

THESIS FOR THE DEGREE OF LICENTIATE OF ENGINEERING

**On the Analysis of DC Network Dynamics of VSC-based
HVDC Systems**

GUSTAVO PINARES



Department of Energy and Environment
Division of Electric Power Engineering
CHALMERS UNIVERSITY OF TECHNOLOGY
Göteborg, Sweden 2014

On the Analysis of DC Network Dynamics of VSC-based HVDC Systems
GUSTAVO PINARES

©GUSTAVO PINARES, 2014

Licentiate Thesis at Chalmers University of Technology

Department of Energy and Environment
Division of Electric Power Engineering
SE-412 96 Göteborg
Sweden
Telephone +46(0)31-772 1000

Chalmers Bibliotek, Reproservice
Göteborg, Sweden 2014

To Karina ♡

On the Analysis of DC Network Dynamics of VSC-based HVDC systems
GUSTAVO PINARES
Department of Energy and Environment
Chalmers University of Technology

Abstract

In this thesis, the dc network dynamics of VSC-HVDC systems is investigated through eigenvalue and frequency domain analysis. The eigenvalue analysis has been used to identify the factors that have an impact on the system stability. It has been determined that instability in the form of sustained oscillations can take place, and that the operating point, the dc side electrical characteristics, the strength of the ac system and the controller structure, are the major factors that impact the stability of the system.

A frequency domain approach is proposed in this thesis in order to explain the instability that occurs in the system. A two-terminal VSC-HVDC system is modelled as a Single-Input-Single-Output feedback system, and the VSC-system and the dc grid transfer functions are defined and derived. The VSC-system transfer function has been interpreted as an admittance, whose conductance is positive or negative, depending on the direction of the power. The main characteristic of the dc grid transfer function is the resonance peak, which appear as a result of the RLC characteristic of the dc transmission line. When the resonance phenomenon takes place at a frequency in which the VSC conductance is negative, there is a risk that the resonance becomes amplified. Whether or not the system becomes unstable depends on the magnitude of the dc grid resonance peak and the magnitude of the VSC conductance. Then, the proposed procedure can provide criteria for the design of controllers which guarantee that dc side resonances do not become amplified.

Finally, simulations in a four-terminal HVDC system show that instability takes places according to the conditions stated in the previous analysis. The dynamic performance of the voltage-droop and the voltage-margin control strategies have been compared as well and it has been found that the former performs better than the latter. The impact of other control loops is also studied through simulations, and it is shown that reactive power injection and the control of the alternating-voltage increases the stability limit. Furthermore, it has been shown that abrupt changes on the control modes trigger other types of phenomena which need to be studied from the large signal point of view.

Index Terms: HVDC, VSC, Eigenvalue Analysis, Frequency Domain Analysis, DC Side Dynamics, DC Grid Resonance, VSC Admittance, DC Grid Impedance.

Acknowledgements

The financial support provided by the Chalmers Energy Initiative research program is gratefully acknowledged.

I would like to express my sincere gratitude to Professor Lina Bertling-Tjernberg, for convincing me to come back to Chalmers, for her support, advices and encouragement during the time she acted as the examiner and supervisor of my project. I would also like to thank my former co-supervisors, Dr. Tuan Ahn Le, Prof. Claes Breitholtz and Dr. Abdel-Aty Edris for the ideas and passionate discussions we had regarding the progress of my work. Many thanks as well to my reference group, Lennart Harnefors and Bertil Berggren from ABB, Emil Hillberg from STRI, Ander Manikoff formerly from SP, Sebastien Gros and Per Norberg from Chalmers, for their ideas during our meetings.

Then, I would like to thank the charismatic Associate Professor Massimo Bongiorno for taking over the supervision of my project in a notable manner. Thanks for the precise use of his sharp knife when reviewing the thesis manuscript. Many thanks also to Professor Torbjörn Thiringer for taking over the role as the examiner of my project and for being surprisingly quick when reviewing the thesis.

Thanks to my colleagues at the Elteknik division for the nice working environment, particularly to the football team, Mebtu Beza, Shemsedin Nursebo, Tarik Abdulahovic, Kalid Yunus, etc, for our legendary Monday football matches at Fysiken and the nice talks about our epic moves and goals on Tuesday's lunches. Also especial thanks to my friend Wang Feng, my former roommate, for his support with great ideas while he was working with us. Many thanks also to my former students, Oscar Lennerhag and Viktor Träff, for their contributions with interesting findings while carrying out their master thesis with me.

To my family: Quiero agradecer también a mi familia, especialmente a mis papás, por el apoyo, el ejemplo y el cariño que me dieron desde siempre. ¡Los quiero mucho!

Finally, to close on a high note, infinite thanks to my beautiful wife, Karina, for her kindness, love and support, especially during these adventurous years abroad. I love you!

Gustavo
Göteborg, Sweden
April 25th, 2014.

List of Abbreviations

| | |
|----------|--|
| CPL | Constant Power Load |
| CTL | Cascaded Two-Level Converter |
| DVC | Direct-Voltage Controller |
| HVDC | High Voltage Direct Current |
| LHP | Left Half of the s -plane |
| MMC | Modular Multilevel Converter |
| MTDC | Multi-Terminal High Voltage Direct Current |
| NPC | Neutral-Point Clamped |
| PCC | Point of common coupling |
| PLL | Phase-Locked Loop |
| PSC | Power Synchronization Control |
| pu | Per Unit |
| PWM | Pulse-Width Modulation |
| RHP | Right Half of the s -plane |
| SCR | Short Circuit Ratio |
| SISO | Single-Input Single-Output |
| SPWM | Sinusoidal Pulse-Width Modulation |
| VCC | Vector Current Controller |
| VSC | Voltage Source Converters |
| VSC-HVDC | Voltage Source Converter based High Voltage Direct Current |

List of Symbols

| | |
|---------------------------------|---|
| $e_{1\text{rated}}$ | Rated pole-to-neutral direct-voltage of the VSC ₁ |
| $P_{1\text{rated}}$ | Rated per-pole power of the VSC ₁ |
| C | Pole-to-neutral VSC capacitance |
| τ | Capacitor time constant |
| $u_{ca,b,c}$ | Converter voltage, phases a , b and c |
| $u_{ga,b,c}$ | Grid voltage, phases a , b and c |
| $u_{sa,b,c}$ | AC source voltage, phases a , b and c |
| $u_{\text{ref}a,b,c}$ | Reference voltage generated by the VCC, phases a , b and c |
| u_c | Three-phase converter voltage |
| u_g | Three-phase grid voltage |
| u_s | Three-phase ac source voltage |
| \underline{u}_c^{dq} | Converter voltage in the dq frame |
| \underline{u}_g^{dq} | Grid voltage in the dq frame |
| \underline{u}_s^{dq} | AC source voltage in the dq frame |
| \underline{u}_g^{xy} | Grid voltage in an arbitrary xy frame |
| $\underline{u}_g^{\alpha\beta}$ | Grid voltage in an arbitrary $\alpha\beta$ frame |
| $u_c^{d\text{ref}}$ | VCC output voltage reference in the d axis |
| $u_c^{q\text{ref}}$ | VCC output voltage reference in the q axis |
| i_f | Three-phase current through the VSC filter reactor |
| i_s | Three-phase current through the ac source impedance |
| $i_f^{d\text{ref}}$ | VCC current reference in the d axis |
| $i_f^{q\text{ref}}$ | VCC current reference in the q axis |
| i_f^{dq} | Current through the VSC filter reactor in the dq frame |
| $i_f^{\alpha\beta}$ | Current through the VSC filter reactor in the $\alpha\beta$ frame |
| i_s^{dq} | Current through the ac source impedance in the dq frame |
| S_g | Apparent power injected/absorbed by the VSC at the PCC |
| P_g | Active power injected/absorbed by the VSC at the PCC |
| Q_g | Reactive power injected/absorbed by the VSC at the PCC |
| P_g^{ref} | Active power controller reference |
| Q_g^{ref} | Reactive power controller reference |
| e_i^{ref} | Direct-voltage controller reference of the i -th VSC |
| u_g^{ref} | Alternating-voltage controller reference |
| e_i | Pole-to-neutral direct-voltage at the i -th dc node |
| i_i | Current injected/absorbed by the i -th VSC to its dc side capacitor |
| P_i | Power injected/absorbed by the i -th VSC to its dc side capacitor |
| θ_g | Angle estimated by the PLL |
| ω_g | Frequency estimated by the PLL |
| R_s | Resistance of the ac source impedance |
| L_s | Inductance of the ac source impedance |
| R_f | Resistance of the VSC filter reactor |
| L_f | Inductance of the VSC filter reactor |
| C_f | AC capacitor connected at the PCC |
| X_f | Reactance of the filter reactor |

| | |
|----------------------------|---|
| $C_{bj,k}$ | Equivalent capacitor of the branch connected between the nodes j and k |
| R_{bi} | Equivalent resistor of the i -th branch |
| L_{bi} | Equivalent inductor of the i -th branch |
| i_{bi} | Current through the i -th branch |
| \mathbf{C} | DC grid capacitance matrix |
| \mathbf{R} | DC grid resistance matrix |
| \mathbf{L} | DC grid inductance matrix |
| \mathbf{T} | DC grid incidence matrix |
| \mathbf{Q} | DC grid current injection matrix |
| α | VCC bandwidth |
| k_p | VCC proportional gain |
| k_i | VCC integral gain |
| ω_n | DVC undamped resonance frequency |
| ξ | DVC damping ratio |
| k_{pe} | DVC proportional gain |
| k_{ie} | DVC integral gain |
| α_{PLL} | PLL bandwidth |
| k_{pl} | PLL propotional gain |
| k_{il} | PLL integral gain |
| k_{pP} | Active power controller proportional gain |
| k_{iP} | Active power controller integral gain |
| k_{pQ} | Reactive power controller proportional gain |
| k_{iQ} | Reactive power controller integral gain |
| k_{pU} | Alternating-voltage controller proportional gain |
| k_{iU} | Alternating-voltage controller integral gain |
| m^d | State that accounts for the integral action of the VCC in the d axis |
| m^q | State that accounts for the integral action of the VCC in the q axis |
| n | State that accounts for the integral action of the DVC |
| n_ω | State that accounts for the integral action of the PLL |
| $\Delta \mathbf{x}_{si}^c$ | State vector of the VSC state space model which controls the power |
| $\Delta \mathbf{r}_{si}^c$ | Input vector of the VSC state space model which controls the power |
| $\Delta \mathbf{A}_{si}^c$ | State matrix of the VSC state space model which controls the power |
| $\Delta \mathbf{B}_{ri}^c$ | Input matrix of the VSC state space model which controls the power |
| $\Delta \mathbf{B}_{ei}^c$ | Voltage input matrix of the VSC state space model which controls the power |
| $\Delta \mathbf{C}_{si}^c$ | Output matrix of the VSC state space model which controls the power |
| $\Delta \mathbf{D}_{ri}^c$ | Feedforward matrix of the VSC state space model which controls the power |
| ΔD_{ei}^c | Voltage feedforward factor of the VSC state space model which controls the power |
| $\Delta \mathbf{x}_{si}^e$ | State vector of the VSC state space model which controls the direct-voltage |
| $\Delta \mathbf{r}_{si}^e$ | Input vector of the VSC state space model which controls the direct-voltage |
| $\Delta \mathbf{A}_{si}^e$ | State matrix of the VSC state space model which controls the direct-voltage |
| $\Delta \mathbf{B}_{ri}^e$ | Input matrix of the VSC state space model which controls the direct-voltage |
| $\Delta \mathbf{B}_{ei}^e$ | Voltage input matrix of the VSC state space model which controls the direct-voltage |
| $\Delta \mathbf{C}_{si}^e$ | Output matrix of the VSC state space model which controls the direct-voltage |

| | |
|-----------------------------|--|
| $\Delta \mathbf{D}_{ri}^e$ | Feedforward matrix of the VSC state space model which controls the direct-voltage |
| ΔD_{ei}^e | Voltage feedforward factor of the VSC state space model which controls the direct-voltage |
| $\Delta \mathbf{x}_g$ | State vector of the dc grid state space model |
| $\Delta \mathbf{i}$ | Current input/output vector of the dc grid/VSC-set state space model |
| $\Delta \mathbf{A}_g$ | Matrix vector of the dc grid state space model |
| $\Delta \mathbf{B}_g$ | Input matrix of the dc grid state space model |
| $\Delta \mathbf{C}_g$ | Output matrix of the dc grid state space model |
| $\Delta \mathbf{e}$ | Voltage output/input vector of the dc grid/VSC-set state space model |
| $\Delta \mathbf{x}_{vsc}$ | State vector of the VSC-set subsystem |
| $\Delta \mathbf{r}_{vsc}$ | Input vector of the VSC-set subsystem |
| $\Delta \mathbf{A}_{vsc}$ | Matrix vector of the VSC-set subsystem |
| $\Delta \mathbf{B}_{vsc}^r$ | Input matrix of the VSC-set subsystem |
| $\Delta \mathbf{B}_{vsc}^e$ | Voltage input matrix of the VSC-set subsystem |
| $\Delta \mathbf{C}_{vsc}$ | Output matrix of the VSC-set subsystem |
| $\Delta \mathbf{D}_{vsc}^r$ | Feedforward matrix of the VSC-set subsystem |
| $\Delta \mathbf{D}_{vsc}^e$ | Voltage feedforward voltage matrix of the VSC-set subsystem |
| $\Delta \mathbf{x}_{sys}$ | State vector of the VSC-HVDC system model |
| $\Delta \mathbf{r}_{sys}$ | Input vector of the VSC-HVDC system model |
| $\Delta \mathbf{A}_{sys}$ | Matrix vector of the VSC-HVDC system model |
| $\Delta \mathbf{B}_{sys}$ | Input matrix of the VSC-HVDC system model |
| $\Delta \mathbf{C}_{sys}$ | Output matrix of the VSC-HVDC system model |
| $\Delta \mathbf{y}_{sys}$ | Output vector of the VSC-HVDC system model |
| λ_i | i -th eigenvalue of the system |
| C_{eq} | Parallel of the VSC capacitor and cable capacitor |
| R_{12} | Resistance of the cable connected between the nodes 1 and 2 |
| L_{12} | Inductance of the cable connected between the nodes 1 and 2 |
| R_{10} | Equivalent resistance which represents the steady state power consumption/supply of VSC ₁ |
| R_{20} | Equivalent resistance which represents the steady state power consumption/supply of VSC ₂ |
| Δi_1 | Current variation injected/absorbed to the dc grid by VSC ₁ |
| Δi_2 | Current variation injected/absorbed to the dc grid by VSC ₂ |
| Δi_1^* | Current variation corresponding to the VSC ₁ dynamics |
| $G(s)$ | DC grid transfer function |
| $G'(s)$ | First approximation of the dc grid transfer function |
| \tilde{G} | Second approximation of the dc grid transfer function |
| \tilde{G}_0 | Third approximation of the dc grid transfer function |
| F | VSC-system transfer function |
| F_{PLL} | PLL transfer function |
| z_1^d | Zero of the VSC-system transfer function |
| k | Drop setting of the voltage-droop controller |

Contents

| | |
|--|------------|
| Abstract | v |
| Aknowledgements | vii |
| List of Abbreviations | ix |
| List of Symbols | xi |
| 1 Introduction | 1 |
| 1.1 Background and motivation | 1 |
| 1.2 Purpose of the thesis and main contributions | 2 |
| 1.3 Structure of the thesis | 2 |
| 1.4 List of publications | 3 |
| 2 VSC-HVDC systems | 5 |
| 2.1 Introduction to VSC-HVDC system | 5 |
| 2.2 Main components of a grid-connected VSC station | 6 |
| 2.2.1 DC side capacitor | 6 |
| 2.2.2 Phase reactor | 7 |
| 2.2.3 AC side filters | 7 |
| 2.2.4 Converter transformer | 8 |
| 2.3 Operating principles | 8 |
| 2.3.1 VSC as a controllable alternating-voltage source | 8 |
| 2.3.2 Pulse-width modulation method | 10 |
| 2.4 VSC control system | 12 |
| 2.4.1 Vector current control method | 14 |
| 2.4.2 Phase-locked loop | 17 |
| 2.4.3 Direct-voltage controller | 19 |
| 2.4.4 Active cower control | 22 |
| 2.4.5 Reactive power and alternating-voltage control | 22 |
| 2.5 New challenges for VSC-HVDC systems | 23 |
| 2.5.1 New multilevel topologies | 23 |
| 2.5.2 VSC-based multi-terminal HVDC systems | 24 |
| 2.6 Conclusions | 27 |
| 3 Overview on dc network dynamics | 29 |
| 3.1 Dynamic issues in dc microgrids | 29 |

| | | |
|----------|---|-----------|
| 3.2 | Dynamic issues in VSC-HVDC systems | 33 |
| 3.2.1 | AC side dynamics of VSC-HVDC | 34 |
| 3.2.2 | DC side dynamics of VSC-HVDC | 35 |
| 3.2.3 | DC dynamics in multi-terminal VSC-HVDC systems | 36 |
| 3.3 | Study of an ideal case | 38 |
| 3.4 | Conclusions | 43 |
| 4 | Small signal modelling and analysis of VSC-HVDC system | 45 |
| 4.1 | Modelling approach | 45 |
| 4.2 | Assumptions | 47 |
| 4.3 | State space model of a VSC connected to an infinite ac source | 48 |
| 4.3.1 | VSC open-loop model | 48 |
| 4.3.2 | VSC closed-loop model with current controller | 49 |
| 4.3.3 | VSC closed loop model with direct voltage controller | 50 |
| 4.4 | State space model of a VSC connected to a non-infinite ac source | 51 |
| 4.4.1 | Constant frequency vectors in the converter dq frame | 51 |
| 4.4.2 | VSC closed-loop model - no ac filter capacitor at the PCC | 52 |
| 4.4.3 | VSC closed-loop model - ac filter capacitor at the PCC | 54 |
| 4.5 | DC grid state space model | 57 |
| 4.6 | HVDC system state space model | 59 |
| 4.7 | Eigenvalue analysis | 61 |
| 4.7.1 | System data | 61 |
| 4.7.2 | VSCs connected to infinite ac sources | 62 |
| 4.7.3 | VSCs connected to non-infinite ac sources | 69 |
| 4.7.4 | VSCs connected to non-infinite ac sources with an shunt capacitor at the PCC | 73 |
| 4.8 | Conclusions | 75 |
| 5 | Frequency domain analysis on HVDC systems | 77 |
| 5.1 | Stability analysis using a frequency domain approach | 77 |
| 5.2 | Preliminary considerations | 78 |
| 5.3 | The dc grid transfer function | 80 |
| 5.4 | The VSC-system transfer function | 84 |
| 5.5 | Stability investigation using a frequency domain approach | 87 |
| 5.5.1 | Analysis of the dc-grid subsystem | 87 |
| 5.5.2 | Analysis of the VSC subsystem - The infinite ac source case | 87 |
| 5.5.3 | The VSC admittance and the dc grid impedance | 89 |
| 5.5.4 | Analysis of the VSC subsystem - The non-infinite ac grid case | 92 |
| 5.5.5 | Analysis of the VSC subsystem - Capacitor connected at the PCC | 93 |
| 5.6 | Conclusions | 96 |
| 6 | Simulations in a multi-terminal configuration | 97 |
| 6.1 | System description | 97 |
| 6.2 | Simulated case | 98 |
| 6.3 | Voltage-margin control strategy | 99 |
| 6.4 | Voltage-droop control strategy | 102 |
| 6.5 | Impact of other control loops | 104 |

| | | |
|----------|---|------------|
| 6.6 | Conclusions | 105 |
| 7 | Conclusions and future work | 107 |
| 7.1 | Conclusions | 107 |
| 7.2 | Future work | 108 |
| | References | 111 |
| A | Three-phase transformations | 117 |
| A.1 | Transformation of three phase quantities to vectors | 117 |
| A.2 | Transformation between stationary and rotating coordinate systems | 118 |
| B | Symbols and Per-unit Convention | 121 |
| B.1 | Coordinate systems | 121 |
| B.2 | Per unit values | 122 |

Contents

Chapter 1

Introduction

1.1 Background and motivation

In recent years, Voltage Source Converter based HVDC (VSC-HVDC) systems have been proposed as an attractive solution for the integration of renewable energy sources located far away from the consumption centres [1, 2] and for the integration of electricity markets located over large geographical areas [3, 4]. Since the first installation put in operation in 1997 [5] to interconnect the North and the South regions of Gotland, the VSC technology has improved tremendously in terms of power ratings, losses, and harmonic performance [16]. An example of that are the multilevel VSC topologies developed by the main manufacturers [10–12], which have decreased the losses to a level comparable to thyristor-based HVDC systems (around 1% [10]). Moreover, compared to the thyristor-based converters, VSCs have very convenient controllability features, such as the independent control of active and reactive power. It is recognized also that VSC-HVDC systems are convenient for the interconnection of weak grids [15, 16]. In addition, in the dc side, VSCs are so versatile that various strategies can be devised for the control of voltage-power in the dc side [31–33, 57]. Those features make VSC convenient for more complex HVDC structures, such as the multi-terminal HVDC (MTDC) systems proposed in [2–4, 6, 7].

From the dynamic performance perspective, VSC-HVDC systems have been traditionally viewed as means to enhance the dynamic performance of the existing ac system. For example, several works has been devoted to the use of VSC-HVDC systems for power oscillation damping, and for ac voltage support [43]. Another concern has been the undesired interactions between VSCs and the ac systems to which they are connected [44, 45]. However, few studies regarding the dynamic interaction between VSCs and the dc network can be found in the literature [47–49]. On the other hand, a large number of works can be found regarding the analysis of the dc network dynamics in low power multi-converter systems (dc microgrids) [36, 39, 41, 42]. For example, the impact of the load characteristics on the stability of the system is studied in [38, 39, 42]. For this kind of investigations, a frequency domain approach is proposed in [40, 41] from which design criteria are provided. In high power applications, the interest in the dc network dynamics has arisen with the interest in MTDC system. In [49], a thorough analysis on the control and protection of MTDC

systems has been carried out. In this work, instability in the dc side of the system was identified also in a point-to-point HVDC system. Other works, such as [50–52], deal with the study of the stability of MTDC systems from a broad perspective. In these works, MTDC systems are modelled and the impact of the controller parameters on the stability of the system is determined through eigenvalue analysis. The risk of dc-side resonances is recognized in [7], where it is mentioned that the mitigation of low frequency dc-side resonances might become a complicated task in complex HVDC structures such as MTDC systems.

The interest in the dc-side dynamics in VSC-HVDC systems has risen when more complex dc network structures have come into the scene. Typically, the investigation of the dynamic characteristics of VSC-HVDCs system has been carried out through eigenvalue analysis and, to some extent, frequency domain analysis. However, they do not strictly focus on the possible stability problems originated from the dc side of the system. The reviewed research work indicates that undesired dynamic problems, which originate in the dc network, can take place in any kind of dc system, especially, when considering more complex HVDC structures, such as MTDC systems. For that reason, a conscientious study on the dynamic characteristics of the dc-side of VSC-HVDC systems is needed.

1.2 Purpose of the thesis and main contributions

The purpose of this thesis is to explain of the different factors that impact the dc-side dynamic performance of VSC-HVDC systems. In order to accomplish this goal, eigenvalue and frequency domain analysis are used in this thesis. To the best author's knowledge, the following are the main contribution of this work:

1. From the dc-side stability point of view, the main factors that limit the power transfer in a point-to-point VSC-HVDC system has been established through eigenvalue analysis. Along with this, a general procedure to obtain the state space model of a general HVDC configuration, VSC-based, has been provided.
2. An approach based on the frequency response of the subsystems (defined in this thesis) that form the VSC-HVDC system, is proposed to explain the origin of the dc-side instability found with eigenvalue analysis.

1.3 Structure of the thesis

Chapter 1 provides the introduction to the topic, where the background, the motivation, the purpose, and contributions of the thesis are presented. In Chapter 2, the VSC-HVDC technology, the VSC control structure, and the challenges for future VSC-HVDC systems are presented in order to provide the reader with a basic background on the topic. Chapter 3 begins with a review on the main dynamic issues investigated in low power dc grids, since their characteristics are similar to high power dc systems. The chapter continues with a review on the dynamic problems found in VSC-HVDC systems. In Chapter 4, the analysis of the dc-side dynamics is performed in a two-terminal VSC-HVDC system.

A general procedure to develop a state space model of an HVDC system is presented, which is valid for more complex HVDC structures. Eigenvalue analysis is used to find the conditions in which instability takes place in the system. In Chapter 5, the instability cases are explained through the analysis of the frequency response of the main elements which compose the two-terminal VSC-HVDC system. The VSC *admittance* and the dc grid *impedance* are defined and derived in this chapter. In Chapter 6, simulations which verify the results obtained in the previous chapters are presented. Finally, the thesis ends with the conclusions and ideas planned for future work, presented in Chapter 7.

1.4 List of publications

The articles originated from this research work are the following

- I. G. Pinares, T. A. Le, L. Bertling-Tjernberg, C. Breitholtz, A. Edris, "On the analysis of the dc dynamics of multi-terminal VSC-HVDC systems using small signal modeling," *IEEE Power Tech conference*, Grenoble, France, 16-20, June, 2013.
- II. G. Pinares, T. A. Le, L. Bertling-Tjernberg, C. Breitholtz, "Analysis of the dc Dynamics of VSC-HVDC Systems Using a Frequency Domain Approach," presented at IEEE Asia Pacific Power Energy Engineering Conference, Hong Kong, China, 8-11, December, 2013.
- III. G. Pinares, "Analysis of the dc Dynamics of VSC-HVDC Systems Connected to Weak AC Grids Using a Frequency Domain Approach," submitted to the Power Systems Computation Conference PSCC, Wroclaw, Poland, 18-22, August, 2014.

The author has also contributed with the following papers not included in this thesis:

1. G. Pinares, M. Bollen, "Understanding the Operation of HVDC Grids," presented at Cigre International Symposium The Electric Power System of the Future, Integrating supergrids and microgrids, Bologna, Italy, 13-15, September, 2011.
2. G. Pinares, N. Ullah, P. Brunnegard, M. Lindgren, "Fault Analysis of a Multilevel-Voltage-Source-Converter-based Multi-terminal HVDC system," presented at Cigre HVDC Colloquium, San Francisco, March 7, 2012.

Chapter 1. Introduction

Chapter 2

VSC-HVDC systems

The intention of this chapter is to provide the reader with a basic background on the VSC-HVDC technology. This chapter starts with a brief introduction to VSC-HVDC systems. Following to that, a brief description of the most important elements which compose a VSC station is presented. Then, an introduction to the operating principle of the VSC-HVDC is presented. Afterwards, the control system is described in detail, since it plays an important role in the dynamic behaviour of the VSC-HVDC system. Finally, new challenges for the VSC-HVDC systems are summarized.

2.1 Introduction to VSC-HVDC system

The typical configuration of a two-terminal VSC-HVDC system is displayed in Figure 2.1, where two VSCs are interconnected through a dc transmission line (cable or overhead transmission line). Usually, the control of the transmitted power flow over the dc-transmission line is achieved by setting one VSC to regulate the direct-voltage of the dc-node to which it is connected, and setting the other VSC to regulate the power. As will be explained later in

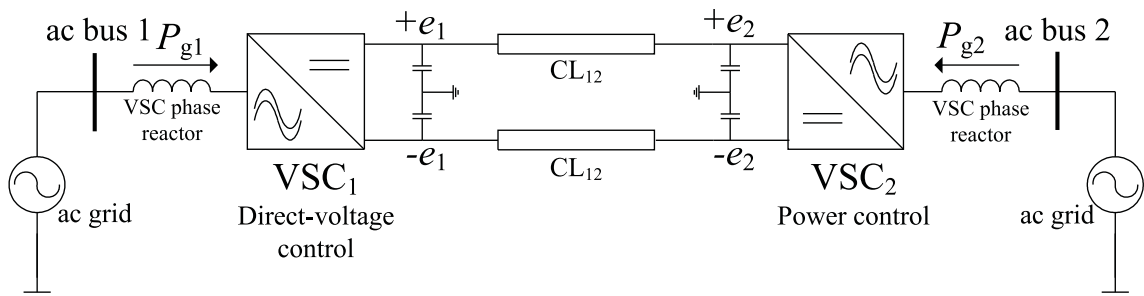


Figure 2.1: Two-terminal VSC-HVDC system.

Section 2.3, the control of the direct-voltage is essential for the operation of the VSC, since VSCs are able to generate a three-phase alternating-voltage with a desired phase, magnitude and frequency as long as there is a sufficiently stiff direct-voltage source in the dc side

of the converter. The VSC’s ability of generating a desired alternating-voltage makes the independent control of the active and reactive power possible, which is one of the greatest advantages of this converter technology over the thyristor-based converters. Moreover, since the valves which compose the VSC allow bidirectional flow of current, the power can be reversed without the need of inverting the polarity of the direct-voltage, as opposite to the classical HVDC system. VSCs are suitable also for multi-terminal configurations, i.e. HVDC systems in which more than two VSCs are interconnected through a dc grid.

Since the VSCs are essential devices of a VSC-HVDC system, the VSC station’s main components, operating principles and control system are described in the next sections.

2.2 Main components of a grid-connected VSC station

Figure 2.2 shows the typical configuration of a grid-connected two-level VSC station. Typically, a VSC station is composed of capacitors in the dc side, and phase reactors, filters and transformers in the ac side. These components are briefly described next.

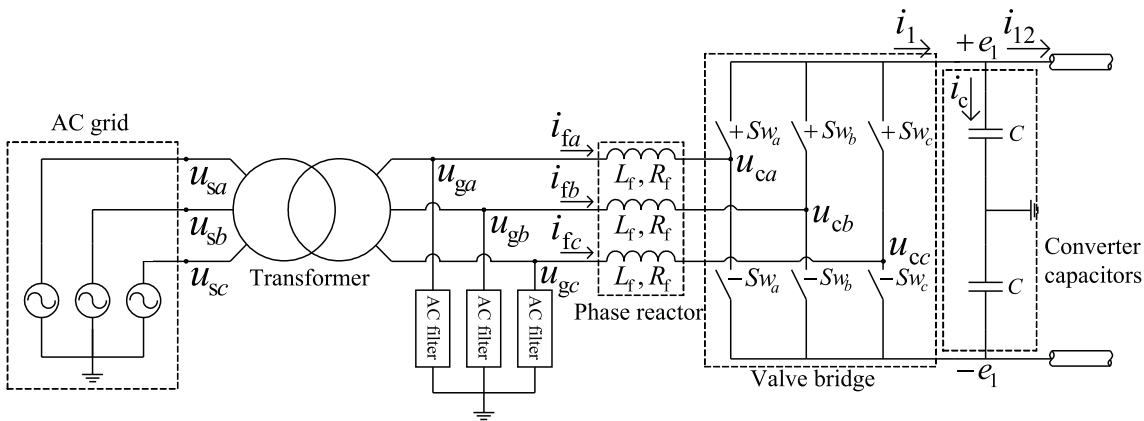


Figure 2.2: Configuration of a VSC station

2.2.1 DC side capacitor

The dc side capacitor is one of the key components of the VSC since it is this element which provides a stable direct-voltage from which the alternating-voltage can be generated. The capacitor also reduces the ripple introduced by the harmonics injected by the VSC into the dc side [15]. The capacitor rating is usually designed considering the amount of energy that the capacitor can store. The *capacitor time constant* is often used as a measure of the amount of capacitor energy. Taking Figure 2.2 as a reference, the capacitor time constant is defined as

$$\tau = \frac{C e_{1\text{rated}}^2}{2P_{1\text{rated}}} \quad (2.1)$$

2.2. Main components of a grid-connected VSC station

where C is the pole-to-neutral capacitance, $e_{1\text{rated}}$ is the pole-to-neutral rated voltage, and $P_{1\text{rated}}$ is the per-pole rated power of the VSC. Physically, the capacitor time constant represents the time that it takes to fully discharge the capacitor when a constant power, $P_{1\text{rated}}$, is drawn from it. A τ of 2ms is recommended in [15], while in [10], it is claimed that the total energy stored per rated power is typically 30-40kJ/MVA, which leads to a capacitor time constant of 30-40ms. In this thesis, 5ms is assumed. For example, from the values that will be indicated in Table 3.1 ($e_{1\text{rated}} = 300$ kV and $P_{1\text{rated}} = 300$ MW per-pole), the size of the capacitor is calculated as

$$C = \frac{2(0.005)300}{300^2} \quad (2.2)$$

which gives a capacitance of 33.33 μ F.

2.2.2 Phase reactor

The phase reactor facilitates the control of the active and reactive power exchange between the converter and the ac system. The voltage drop over the reactor induces a current whose phase and magnitude defines the power injected or absorbed by the converter. The VSC is able to generate an alternating-voltage with a desired phase angle and magnitude and, therefore, is able to control the current through the reactor via the voltage drop over it.

The phase reactor also filters the high frequency harmonics of the current. Another function of the phase reactor is to limit short-circuit currents when faults occur in the dc side of the converter [15]. According to [15], the typical short-circuit impedance of this type of phase reactor is 0.15 pu.

2.2.3 AC side filters

As will be explained in the next section, the voltage generated by a VSC is composed of a fundamental frequency ac component, plus harmonics. These high-order harmonics are filtered through second or third-order high-pass filters, whose typical configurations are shown in Figure 2.3. Depending on the topology of the VSC, the high-order harmonic content can be decreased to a level where ac filters might be unnecessary.

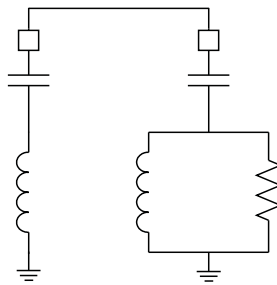


Figure 2.3: Typical AC Filters [15]

2.2.4 Converter transformer

The main function of the converter transformer is to facilitate the interconnection of the VSC with an ac system of different rated voltage [15]. The transformer also isolates the ac grid from the multiples of the third-order harmonics and its multiples generated by the converter. Furthermore, the transformer provides galvanic isolation to the VSC station. The transformer typically has a tap-changer whose main function is to provide voltage regulation support to the system [15].

2.3 Operating principles

Different from *line-commutated converters* (classic HVDC), *self-commutated converters* (VSC) are able to turn off their power electronic valves at any desired current flowing through them. This ability makes it possible that the VSC generates a desired alternating-voltage, provided it is connected to a sufficiently strong dc source on the dc side. As explained in this section, this makes it possible to control the active and reactive power independently, contrarily to the classical HVDC system. Later, the Pulse-Width Modulation (PWM) method is described. PWM is one of the most popular techniques used to generate alternating-voltage while avoiding low-order harmonics. Finally, the generation of alternating-voltages through multilevel topologies is briefly described

2.3.1 VSC as a controllable alternating-voltage source

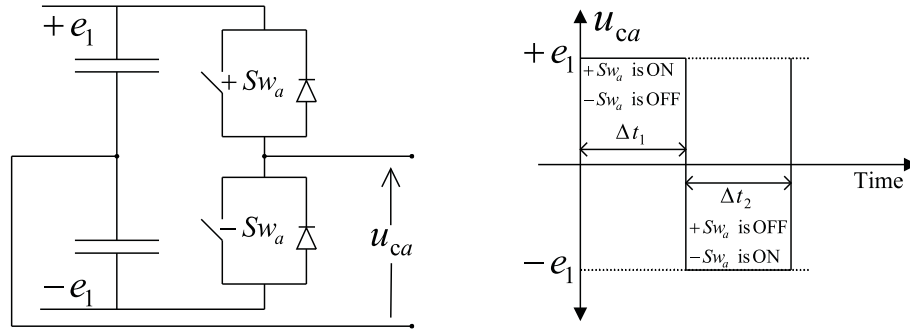
Figure 2.4 shows the phase a of the valve bridge from Figure 2.2. Let us assume that a strong dc source (instead of a capacitor) is connected to the dc side of the VSC. Then, consider the following sequence:

1. During the time Δt_1 , $+Sw_a$ is on, and $-Sw_a$ is off. Then, u_{ca} is $+e_1$.
2. During the time Δt_2 , $+Sw_a$ is off, and $-Sw_a$ is on. Then, u_{ca} is $-e_1$.

The voltage u_{ca} generated by the previous sequence is as shown in Figure 2.4. A square wave with two voltage levels, $+e_1$ and $-e_1$, is obtained, which is the reason why the configuration shown in Figure 2.2 is called two-level converter.

The times Δt_1 and Δt_2 can be selected as desired, in such a way that a square wave of 50 Hz is generated with any phase angle. Moreover, considering that the direct-voltage source can change its magnitude, a square voltage with any phase angle and magnitude can be generated by the VSC. From the Fourier theory, the square wave is composed by a fundamental component plus harmonics, as

$$u_{ca} = (\hat{u}_{ca})_1 \sin(\omega_1 t + \phi_1) + \sum_{h=2}^{\infty} (\hat{u}_{ca})_h \sin(\omega_h t + \phi_h) \quad (2.3)$$


 Figure 2.4: Phase a of the valve arrangement (adapted from [8]).

where $(\hat{u}_{ca})_1$ is the amplitude of the fundamental sinusoidal component, ω_1 is the fundamental frequency, ϕ_1 is the phase shift at the fundamental frequency, $(\hat{u}_{ca})_h$ is the amplitude of the h -th harmonic, ω_h is the angular frequency of the h -th harmonic, and ϕ_h is the phase shift at the h -th harmonic frequency.

Considering only the fundamental component, waiving the need of filters, and the transformer reactance included into the reactor impedance, the interconnection between the VSC and the ac system can be represented by the equivalent diagram shown in Figure 2.5. For such a system, it is well known that the steady-state active and the reactive power injected to the ac system are

$$P_g = \frac{u_g u_c}{X_f} \sin(\delta) \quad (2.4)$$

$$Q_g = -\frac{u_g^2}{X_f} + \frac{u_g u_c}{X_f} \cos(\delta) \quad (2.5)$$

Considering that the angle δ is very small¹, then $\sin(\delta)$ can be approximated to δ and $\cos(\delta)$ to 1. Equations (2.4) and (2.5) can be re-written as

$$P_g = \frac{u_g u_c}{X_f} \delta \quad (2.6)$$

$$Q_g = \left(\frac{u_c - u_g}{X_f} \right) u_g \quad (2.7)$$

From (2.6), it can be seen that the variation of the δ produces a larger variation of P_g , while (2.7) shows that the variation of the voltage difference, $u_c - u_g$ produces a larger variation on the reactive power Q_g . For that reason, it is usually claimed that the active power is controlled by the angle difference of the voltages, and the reactive power is controlled by the magnitude difference of the voltages. Since the VSC can generate a voltage with any frequency, phase, and magnitude, then, the VSC is able to control the active and reactive power independently. Thus, VSCs can be seen as an ideal synchronous machine with no inertia. Different from synchronous generators, the VSC can adjust the phase angle of its generated voltage (and therefore the active power) in a very short time.

¹The angle δ is assumed to be around zero for the sake of illustration. Actually, for a VSC, δ could theoretically take any value between 0° and 90° .

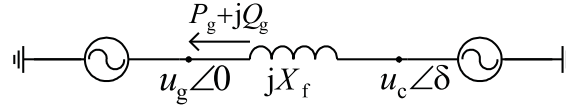


Figure 2.5: AC side of the VSC, with the VSC represented by an ideal alternating-voltage source

Going back to Figure 2.4, the square waveform has a fundamental component with an amplitude equal to [9]

$$(\hat{u}_{ca})_1 = \frac{4}{\pi} e_1 \quad (2.8)$$

and the amplitudes of the harmonics are

$$(\hat{u}_{ca})_h = \frac{(\hat{u}_{ac})_1}{h}, \quad h = 3, 5, 7, \dots \quad (2.9)$$

Equation (2.9) shows that the low-order harmonics are relatively high, which is one of the disadvantages of this modulation method since filters for low order harmonics require bulky components. A solution to this are different modulation methods such as the sinusoidal pulse width modulation, the space vector modulation, or the harmonic elimination [9]. The pulse-width modulation method is summarized next.

2.3.2 Pulse-width modulation method

The Sinusoidal Pulse-Width Modulation (SPWM) method can be explained with the help of Figure 2.6. The SPWM defines the switching pattern for the VSC valves by comparing a carrier signal and a reference signal, as shown in Figure 2.6 (upper plot). In the example shown in the figure, the carrier signal is a 850 Hz triangular wave which varies from -1 to $+1$. The reference signal is a 50 Hz sinusoidal waveform described as

$$u_{\text{ref}a} = m_a \sin(2\pi f_1 t + \phi) \quad (2.10)$$

where m_a is called the *amplitude modulation index*, f_1 is the frequency of the reference voltage and ϕ its phase angle. The signals are compared, and the following rule defines the switching pattern:

1. If the reference is higher than the carrier, then $+Sw_a$ is on and $-Sw_a$ is off.
2. If the reference is lower than the carrier, then $+Sw_a$ is off and $-Sw_a$ is on.

The resulting voltage u_{ca} (phase-to-neutral) is also shown in Figure 2.6 (middle plot), considering a rated direct-voltage of ± 300 kV and a amplitude modulation index of 0.9 (it is also assumed ideal commutation for the valves). The harmonic spectrum in Figure 2.6 (lower plot), shows that the fundamental harmonic has a magnitude of 270 kV (0.9×300 kV). Moreover, the figure shows that there is considerable harmonic content at the multiples of the switching frequency, 850 Hz, and the side bands. It is shown in [9] that the three voltages generated by the converter using the PWM method state above are

$$u_{ca} = (u_{\text{ref}a})e_1, \quad u_{cb} = (u_{\text{ref}b})e_1, \quad u_{cc} = (u_{\text{ref}c})e_1 \quad (2.11)$$

Although the harmonic content is higher than the voltage generated by the square wave modulation, filtering high frequency harmonics requires smaller components which is convenient to reduce costs and footprint. However, high switching frequency increases the

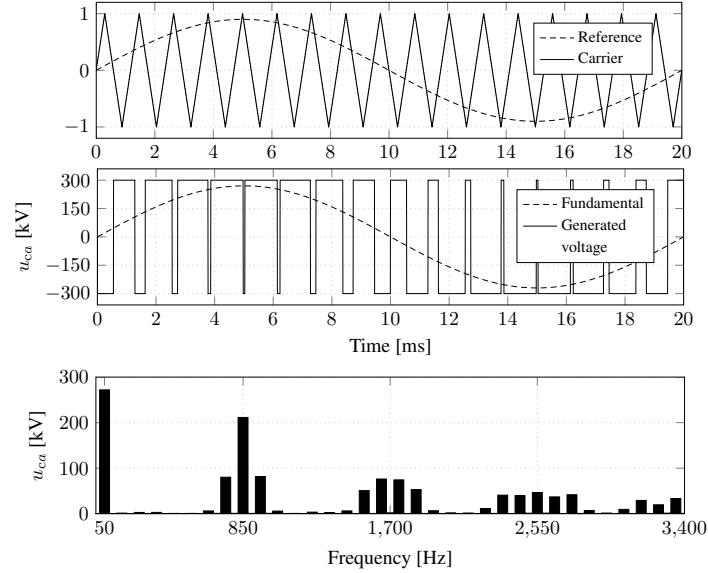


Figure 2.6: Voltage generated by a two-level converter through the SPWM. Upper: Carrier and reference voltages. Middle: Voltage generated and fundamental component. Lower: Harmonic spectrum of the generated phase-to-neutral voltage.

switching losses in the VSC. The nature of the switching losses is described in [9], and it is shown that they depend on the valve technology, the voltage across the valves, the current that the valves conduct, and the switching frequency. From that, the following are means to decrease the switching losses:

1. Decrease the switching frequency. However, that increases the low order harmonics which requires bigger filters. On the other hand, multilevel topologies decrease the individual switching frequency of the valves while improving the generated ac voltage waveform.
2. Decrease the voltage across the valves. That can be achieved through other VSC topologies such as the multilevel technology.
3. Improve the valve technology, in such a way that the switching process becomes faster.

Multilevel topologies have been proposed as a solution to improve the generated voltage waveform and to decrease the losses. With the multilevel technology, not only the voltage across the valves are decreased, but also the individual valve's switching frequency, therefore, the corresponding losses. A three-level Neutral-Point-Clamped (NPC) converter [8] is shown in Figure 2.7 and the generated voltage is shown in Figure 2.8. In contrast to the two-level converter, this type of converter allows three voltage levels, $+e_1$, $-e_1$ and 0. Moreover, in the two-level topology, the voltage across the valve is actually $2e_1$, while in this topology the voltage across the valves is e_1 . Furthermore, the harmonic content, shown in Figure 2.8, is decreased compared to the two-level VSC.

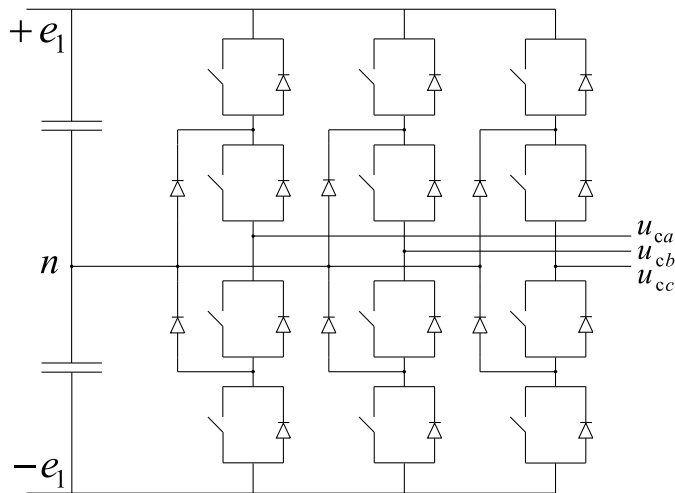


Figure 2.7: Three-level neutral-point-clamped converter

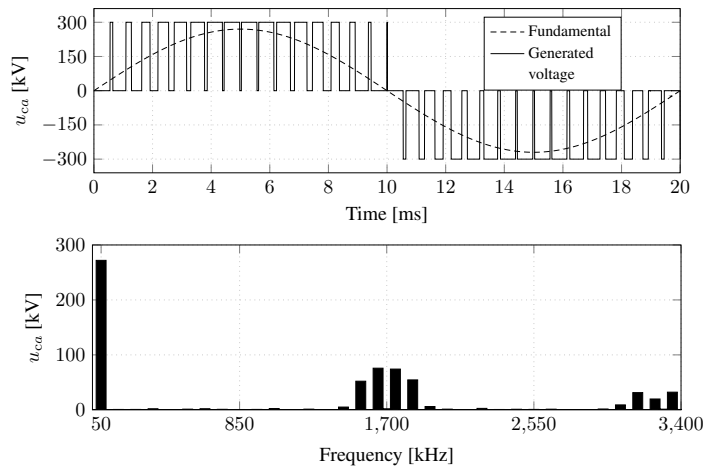


Figure 2.8: Voltage generated by a three-level converter through the SPWM. Upper: Voltage generated and fundamental component. Lower: Harmonic spectrum of the voltage generated

A five-level NPC converter can also be constructed in the same way. Another topology is the flying-capacitor configuration, which can be reviewed in [8]. The more the number of levels, the less switching losses and the less the harmonic content. However, the main disadvantage is the complexity of the circuit, which increases with the number of levels. This is overcome by the recently developed multilevel topologies, which will be briefly described in Section 2.5.

2.4 VSC control system

Several control methods for the control of VSC have been developed and are available in the literature. For example, in the review carried out in [17], the resonant controller, the vector current control, and the power synchronization control methods are mentioned. The vector control method is widely used in grid connected VSCs [12, 15] and it is the one used

in this thesis. The typical structure of a VSC control system is illustrated in Figure 2.9. The core of the control system is the Vector Current Controller (VCC), whose output is a three-phase voltage reference to the PWM block, which issues firing signals to the VSC switches. The VCC has two inputs, i_f^{dref} and i_f^{qref} which are the current references.

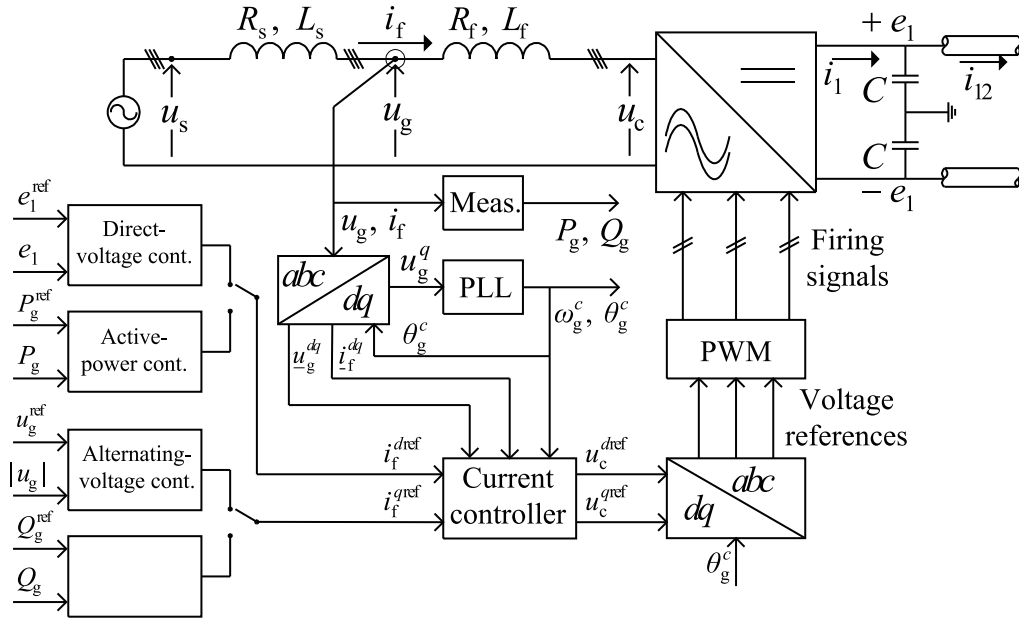


Figure 2.9: VSC control system

Outer controllers are implemented in order to control other quantities, such as the active power, reactive power, direct-voltage and alternating-voltage. The control of the direct-voltage involves active power, since the direct-voltage value is defined by the amount of energy stored in the converter capacitor. Then, the reference i_f^{dref} is used to control either the active power and the direct-voltage, as shown in the figure¹. Another strategy can be to make the active power to be dependent on the direct-voltage, following a voltage-droop characteristic. The control of the alternating-voltage is related to the amount of reactive power support present in the system. Then, the reference i_f^{qref} is used to control either the reactive power or the alternating voltage. As in the dc side, the control of the alternating voltage can be done following a voltage-droop characteristic. A third strategy is to control the alternating-voltage to a fixed frequency waveform (working as a slack bus). This strategy is only useful when VSCs are connected to passive ac grids which do not count on ac sources (or they are weak).

In this section, the different blocks that integrate the control system of the VSC are described. The derivation of the VCC, which is implemented in the dq frame, is presented. Furthermore, the phase-locked loop, which calculates the angle needed to perform the dq transformation, is described. Afterwards, the derivation of the direct-voltage controller is presented. Finally, the active and reactive power controllers are described.

Since the description of the controllers involves voltages and currents in different coordi-

¹It will be explained in the next section that the dq frame is aligned to the rotating voltage vector $u_g^{\alpha\beta}$.

nate systems, the conventions and symbols adopted in this thesis are as specified in Appendix B. Moreover, in most of the cases, the electrical variables are expressed in per-unit values, whose base definitions are also presented in Appendix B.

2.4.1 Vector current control method

The principle of the vector current control method lies in finding the right magnitude and phase of the generated voltage, in such a way that the induced current over the phase reactor has the desired phase and magnitude. In the vector current control method implemented in a rotating frame¹, the three-phase ac quantities are transformed to two dc quantities through the so-called dq transformation which is detailed in Appendix A. As an illustration, in Figure 2.10, the steady-state vector diagram of the voltage drop over the reactor and the corresponding current is plot in two coordinate systems. In Figure 2.10(a), vectors in a generic rotating frame, the xy frame, are shown. The xy frame it is a coordinate system which rotates at the same speed than the vectors, but not aligned to any of them. The vector \underline{u}_g^{xy} , in the xy frame, is expressed as

$$\underline{u}_g^{xy} = u_g^x + ju_g^y. \quad (2.12)$$

From the vector diagram in the xy frame shown in Figure 2.10(a), the complex power S_g is calculated as

$$S_g = P_g + jQ_g = \underline{u}_g^{xy} (\underline{i}_f^{xy})^* \quad (2.13)$$

from where, the active power and reactive power are

$$P_g = u_g^x i_f^x + u_g^y i_f^y \quad (2.14)$$

$$Q_g = -u_g^x i_f^y + u_g^y i_f^x. \quad (2.15)$$

On the other hand, Figure 2.10(b) shows the mentioned steady-state vector diagram in the dq frame where the d axis is aligned to the vector \underline{u}_g^{dq} . In that case, the q component of \underline{u}_g^{dq} is zero. For instance, the vector \underline{u}_g^{dq} , in the dq frame, is

$$\underline{u}_g^{dq} = u_g^d. \quad (2.16)$$

Then, applying (2.13) in the dq frame, the active and reactive power are

$$P_g = u_g^d i_f^d \quad (2.17)$$

$$Q_g = -u_g^d i_f^q \quad (2.18)$$

which means that the active power can be controlled with the d component of the current, i_f^d , and the reactive power with the q of the current, i_f^q .

Considering the ac side of the system shown in Figure 2.11, the following equation, expressed in the $\alpha\beta$ frame (see Appendix B), describes the dynamics of the current through the phase reactor.

$$\frac{d\underline{i}_f^{\alpha\beta}}{dt} = -\frac{R_f}{L_f} \underline{i}_f^{\alpha\beta} + \frac{1}{L_f} \underline{u}_g^{\alpha\beta} - \frac{1}{L_f} \underline{u}_c^{\alpha\beta} \quad (2.19)$$

¹A controller in a stationary frame can also be developed.

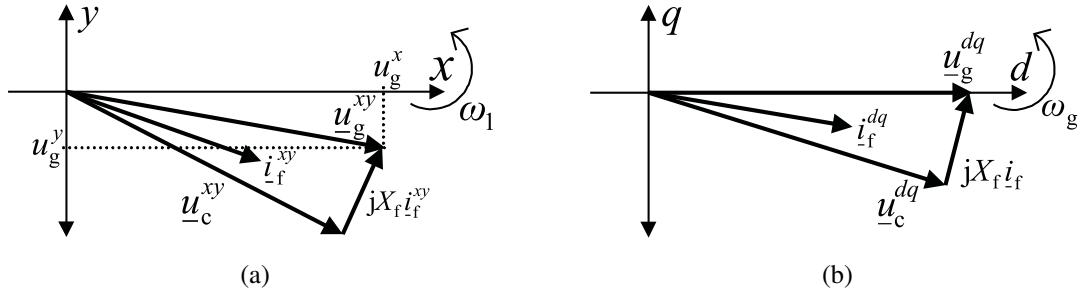


Figure 2.10: Rotating reference frames. (a) generic xy coordinates not aligned to \underline{u}_g^{dq} . (b) dq coordinates aligned to \underline{u}_g .

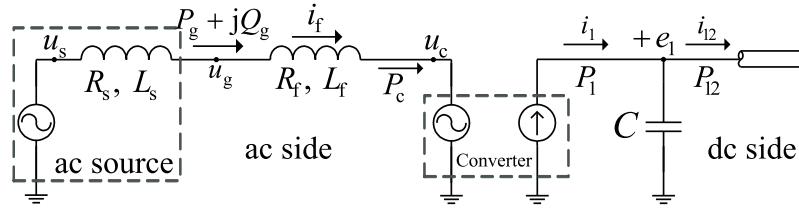


Figure 2.11: Equivalent scheme of a VSC

Note that, in Figure 2.11, the VSC is represented as a voltage source in the ac side, and as a current source in the dc side. In the dq frame, (2.19) becomes

$$\frac{d\underline{i}_f^{dq}}{dt} = -\frac{R_f}{L_f}\underline{i}_f^{dq} - j\omega_g \underline{i}_f^{dq} + \frac{1}{L_f}\underline{u}_g^{dq} - \frac{1}{L_f}\underline{u}_c^{dq} \quad (2.20)$$

or more explicitly

$$\frac{di_f^d}{dt} = -\frac{R_f}{L_f}i_f^d + \omega_g i_f^q + \frac{1}{L_f}u_g^d - \frac{1}{L_f}u_c^d \quad (2.21a)$$

$$\frac{di_f^q}{dt} = -\frac{R_f}{L_f}i_f^q - \omega_g i_f^d + \frac{1}{L_f}u_g^q - \frac{1}{L_f}u_c^q \quad (2.21b)$$

where the synchronization angle θ_g (necessary to perform the dq transformation) and the frequency ω_g are obtained from the three-phase voltage u_g by a Phase-Locked Loop (PLL). From (2.21), it can be seen that there is a cross-coupling between the currents i_f^d and i_f^q . Moreover, it can be seen that the current i_f^{dq} is affected by disturbances on the voltage u_g^{dq} . If the current i_f and the voltage u_g are perfectly measured, the following control law decouples the interaction between i_f^d and i_f^q , and compensates the disturbances introduced by variations on the voltage u_g^{dq}

$$\underline{u}_c^{dq\text{ref}} = \underline{u}_g^{dq} - j\omega_g L_f \underline{i}_f^{dq} + \underline{r}. \quad (2.22)$$

where \underline{r} is the control input. Assuming that the VSC is ideal, then it can generate the output voltage, $\underline{u}_c^{dq\text{ref}}$, exactly as requested by the VCC and with no delay, then

$$\underline{u}_c^{dq} = \underline{u}_c^{dq\text{ref}}. \quad (2.23)$$

Considering (2.23), (2.22) can be entered to (2.20), resulting in

$$\frac{d\dot{i}^{dq}}{dt} = -\frac{R_f}{L_f}\dot{i}^{dq} - \frac{1}{L_f}r \quad (2.24)$$

which is a decoupled, disturbance-free system. In [18], the internal model control method is used to design the VCC for electric drives applications, which has been further used in grid-connected VSC. Equation (2.24) can be expressed in the Laplace domain as

$$\mathbf{i}_f = \mathbf{G}(s)\mathbf{r} \quad (2.25)$$

where

$$\mathbf{i}_f = \begin{bmatrix} \dot{i}_f^d \\ \dot{i}_f^q \end{bmatrix}, \quad \mathbf{G}(s) = \begin{bmatrix} -\frac{1}{L_f s + R_f} & 0 \\ 0 & -\frac{1}{L_f s + R_f} \end{bmatrix}, \quad \mathbf{r} = \begin{bmatrix} r^d \\ r^q \end{bmatrix} \quad (2.26)$$

The input \mathbf{r} can take the following form

$$\mathbf{r} = \mathbf{F}(s)(\mathbf{i}_f^{dqref} - \mathbf{i}_f^{dq}) \quad (2.27)$$

where

$$\mathbf{F}(s) = \begin{bmatrix} F(s) & 0 \\ 0 & F(s) \end{bmatrix}, \quad \mathbf{i}_f^{dqref} = \begin{bmatrix} \dot{i}_f^{dref} \\ \dot{i}_f^{qref} \end{bmatrix} \quad (2.28)$$

Equations (2.25) and (2.27) can be represented by the block diagram shown in Figure 2.12. From the figure, the closed-loop transfer function, $\mathbf{G}_c(s)$ is

$$\mathbf{G}_c(s) = (\mathbf{I} + \mathbf{G}(s)\mathbf{F}(s))^{-1}\mathbf{G}(s)\mathbf{F}(s) \quad (2.29)$$

For the system (2.29) to be a decoupled first-order system, then, the following should be fulfilled

$$\mathbf{G}(s)\mathbf{F}(s) = \begin{bmatrix} \frac{\alpha}{s} & 0 \\ 0 & \frac{\alpha}{s} \end{bmatrix} \quad (2.30)$$

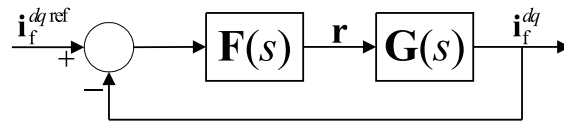


Figure 2.12: Block diagram representation of (2.25) and (2.27)

where α is the bandwidth of closed-loop system. Then, $\mathbf{F}(s)$ should be

$$\mathbf{F}(s) = \mathbf{G}(s)^{-1} \begin{bmatrix} \frac{\alpha}{s} & 0 \\ 0 & \frac{\alpha}{s} \end{bmatrix} = \begin{bmatrix} -(\alpha L_f + \frac{\alpha R_f}{s}) & 0 \\ 0 & -(\alpha L_f + \frac{\alpha R_f}{s}) \end{bmatrix} \quad (2.31)$$

which means that $F(s)$ is a proportional-integral (PI) controller with a proportional gain, k_p , equal to αL_f and an integral gain, k_i , equal to αR_f . Finally, using (2.22), (2.27) and (2.31), the control law is for the VCC in the dq frame is in time domain

$$\underline{u}_c^{dqref} = \underline{u}_g^{dq} - j\omega_g L_f \dot{i}_f^{dq} - k_p(\dot{i}_f^{dqref} - \dot{i}_f^{dq}) - k_i \int_0^t (\dot{i}_f^{dqref} - \dot{i}_f^{dq}) dt \quad (2.32)$$

The output of the controller is the voltage reference \underline{u}_c^{dqref} , which is the input to the PWM block as shown in Figure 2.9. As indicated by (2.11), the three-phase voltage generated by the converter, expressed in the dq frame is

$$\underline{u}_c^{dq} = \underline{u}_c^{dqref} e_1 \quad (2.33)$$

where, it must be stressed that \underline{u}_c^{dqref} and e_1 are in per unit. Equation (2.33) shows that, even for ideal conditions, i.e. no delays and perfect measurement, the voltage generated by the VSC is not exactly the output of the VCC, but it depends on the dc-side direct-voltage. In order to avoid the influence of the direct-voltage, the voltage reference, \underline{u}_c^{dqref} can be pre-multiplied by $\frac{1}{e_1}$, as shown in Figure 2.13. In that case, the voltage generated by the

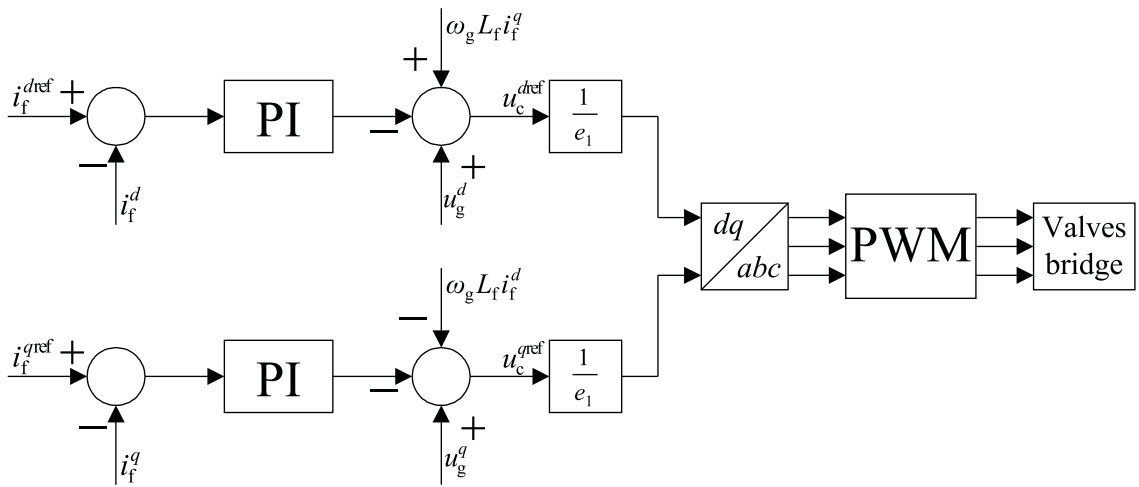


Figure 2.13: VCC representation in the dq frame

VSC will be equal to the voltage reference generated by the VCC, as

$$\underline{u}_c^{dq} = \underline{u}_c^{dqref}. \quad (2.34)$$

The VCC can be further improved with current limiters, anti-windup functions in case of voltage saturation, or active damping for disturbance rejection [20]. Other improvement is the operation under non-symmetrical conditions e.g. non-symmetrical faults, where algorithms to estimate the positive and negative sequence components of the current are proposed in [19,21]. These additional features, however, are not studied in this thesis since the small signal dynamics of the system is investigated in the neighborhood of an operating point. Therefore, it is assumed that the converters are working in their linear range, unsaturated, and in balanced conditions only.

2.4.2 Phase-locked loop

The alignment of the d axis to the rotating voltage $\underline{u}_g^{\alpha\beta}$ is achieved by the knowledge of the phase angle of $\underline{u}_g^{\alpha\beta}$, which is, likewise, estimated by the PLL. The PLL block diagram is

shown in Figure 2.14 and can be mathematically described as

$$\frac{dn_\omega}{dt} = k_{il}\varepsilon \quad (2.35)$$

$$\frac{d\theta_g}{dt} = n_\omega + k_{pl}\varepsilon \quad (2.36)$$

where n_ω is a state which accounts for the integral part of the PLL, θ_g is the phase angle of $\underline{u}_g^{\alpha\beta}$, k_{pl} and k_{il} are gain parameters, and ε is the phase error. Equation (2.35) means that the estimated frequency is updated with a term which is proportional to the error ε . Furthermore, (2.36) says that the angle is updated by the integral of the estimated speed $\hat{\omega}_g$ plus a correction factor which is proportional to the error ε [23]. The error, according to [22], can have the form of

$$\varepsilon = K_{PLL} \sin(\theta_g^i - \theta_g) \quad (2.37)$$

In Figure 2.15, a representation of the *converter dq* frame¹ and the *ideally aligned dq* frame² are shown. The converter *dq* frame is not necessarily aligned to the vector $\underline{u}_g^{\alpha\beta}$, since the

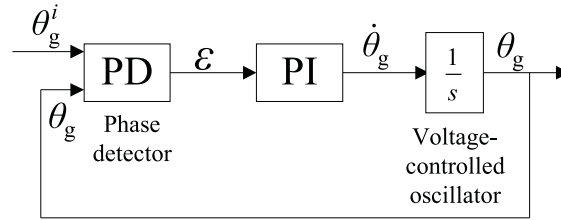


Figure 2.14: Typical PLL block diagram.

PLL cannot estimate the *correct* angle instantaneously. On the other hand, the ideal *dq* frame is always aligned to the rotating voltage $\underline{u}_g^{\alpha\beta}$. The converter *dq* frame should be the same as the ideal *dq* frame in steady-state conditions, but not necessarily during a transient. In Figure 2.15, the *d* axis of the converter *dq* frame is intentionally not aligned, reflecting a transient where the PLL is in the process of calculating the angle which aligns *d* axis of the converter *dq* frame to the rotating voltage $\underline{u}_g^{\alpha\beta}$. From the figure, it can be seen easily that

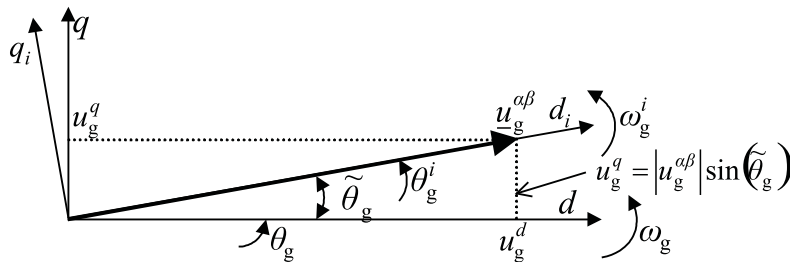


Figure 2.15: Comparison between the converter *dq* frame and ideally aligned *dq* frame.

the *q* component of the voltage in the converter *dq* frame is given by

$$u_g^q = |u_g^{\alpha\beta}| \sin(\tilde{\theta}_g) \quad (2.38)$$

¹In the converter *dq* frame, the angle θ_g estimated by the PLL is used to perform the *dq* transformation.

²In the ideally aligned *dq* frame, the *d* axis is always perfectly aligned to the rotating vector $\underline{u}_g^{\alpha\beta}$.

where $\tilde{\theta}_g = \theta_g^i - \theta_g$. Equation (2.38) shows that u_g^q can be used as the PLL error shown in (2.37). If K_{PLL} in (2.37) is set to one, the normalized voltage u_g^q can be treated as the error ε , that is

$$\varepsilon = \frac{u_g^q}{|u_g^{\alpha\beta}|} \quad (2.39)$$

which is the expression used in [22] and [23]. In works such as [44–46], nevertheless, the per unit value of u_g^q used as the input error of the PLL since they are used in grid-connected VSCs. The error assumed in this thesis is then

$$\varepsilon = u_g^q \quad (2.40)$$

and then, the block diagram shown in Figure 2.16 represents the PLL used in this thesis. Furthermore, the parameters k_{pl} and k_{il} are selected as suggested in [18], that is

$$k_{\text{pl}} = 2\alpha_{\text{PLL}}, \quad k_{\text{il}} = \alpha_{\text{PLL}}^2 \quad (2.41)$$

where α_{PLL} is the bandwidth of the PLL. The value of α_{PLL} is a trade-off between a desired speed of the PLL, and low-frequency harmonics and noise rejection [18, 24, 25]. In [24] a bandwidth of 5 Hz is selected, and in [23] it is mentioned a typical bandwidth of a PLL is between 3 and 5 Hz. In this thesis, a PLL bandwidth of 5 Hz is selected.

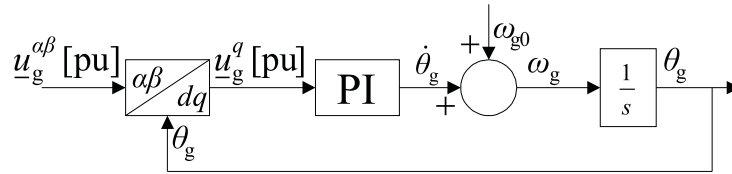


Figure 2.16: PLL block diagram implemented in this thesis.

2.4.3 Direct-voltage controller

The control of the direct-voltage provides the stiffness of a dc source from where the VSCs are able to generate the ac voltages. It also maintains the direct-voltage within acceptable limits. In works such as [45, 46], the *energy stored* in the VSC capacitor is controlled, instead of the voltage e_1 directly (See Figure 2.11). The expression that describes the dynamics of the energy stored in the VSC (in per unit) is

$$\frac{C}{2} \frac{de_1^2}{dt} = P_1 - P_{12} \quad (2.42)$$

where P_1 is the active power per-pole injected by the VSC to the capacitor, and P_{12} is the power that flows through the dc cable, as shown in the dc side of Figure 2.11. If the power P_1 can be controlled perfectly, the following PI controller can be used to control the energy of the VSC capacitor

$$P_1 = k_{\text{pe}} \left(\frac{(e_1^{\text{ref}})^2 - e_1^2}{2} \right) + k_{\text{ie}} \int_0^t \left(\frac{(e_1^{\text{ref}})^2 - e_1^2}{2} \right) dt + P_{12} \quad (2.43)$$

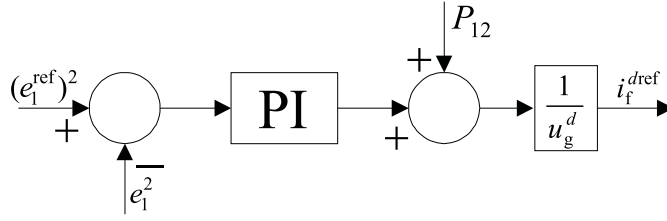


Figure 2.17: DVC block diagram

where the power P_{12}' is the measurement of the power P_{12} which is feed-forwarded to remove disturbances, k_{pe} and k_{ie} are the proportional and the integral gains of the Direct-Voltage Controller (DVC), and e_1^{ref} is the direct-voltage reference. Neglecting the losses over the reactor and the VSC, the active power P_1 injected (or absorbed) by the VSC to the capacitor can be approximated to the active power absorbed (or injected) from ac system at the node G (see Figure 2.11). Furthermore, If the VCC is assumed much faster than the DVC, the current i_f^d can be further approximated to the current reference i_f^{dref} . In that case

$$P_1 \approx u_g^d i_f^{dref}. \quad (2.44)$$

Hence, using (2.43) and (2.44), the control law of the DVC can be defined as

$$i_f^{dref} = \frac{k_{pe}}{u_g^d} \left(\frac{(e_1^{ref})^2 - e_1^2}{2} \right) + \frac{k_{ie}}{u_g^d} \int_0^t \left(\frac{(e_1^{ref})^2 - e_1^2}{2} \right) dt + \frac{P_{12}'}{u_g^d}. \quad (2.45)$$

If the power P_{12} is measured perfectly, and assuming that P_1 is equal to (2.44), (2.45) can be entered to (2.42) and the following can be obtained in the Laplace domain

$$e_1^2 = \frac{C^{-1}(k_{pe}s + k_{ie})}{s^2 + C^{-1}k_{pe}s + C^{-1}k_{ie}} (e_1^{ref})^2 \quad (2.46)$$

whose characteristic polynomial is of second order and has the following form

$$s^2 + 2\omega_n \xi s + \omega_n^2 \quad (2.47)$$

where ω_n is the undamped resonance frequency, and ξ is the damping ratio. From (2.47) the controller gains can be selected as

$$k_{pe} = 2C\omega_n \xi, \quad k_{ie} = C\omega_n^2 \quad (2.48)$$

which are typical expressions that can be find in works such as [46, 54]. The design variables are ω_n and ξ which has to be selected considering the assumption that the VCC is much faster than the DVC.

Others authors, such as [21, 26], derive the DVC considering that the voltage e_1 is controlled, instead of the energy stored at the VSC capacitor. The following describes the dynamics of the voltage on the VSC capacitor

$$C \frac{de_1}{dt} = i_1 - i_{12} \quad (2.49)$$

where i_{12} is the current that flows through the dc cable as indicated in Figure 2.11. Considering the approximation made in (2.44), the current i_1 can be approximated as

$$i_1 \approx \frac{u_g^{d_j d_{ref}}}{e_1} \quad (2.50)$$

then, the DVC is typically defined as the PI controller

$$i_f^{d_{ref}} = \frac{e_1}{u_g^d} \left[k_{pe} (e_1^{ref} - e_1) + k_{ie} \int_0^t (e_1^{ref} - e_1) dt + i'_{12} \right]. \quad (2.51)$$

Using (2.49), (2.50) and (2.51), and considering that i'_{12} is equal to i_{12} , a similar expression as (2.46) is obtained

$$e_1 = \frac{C^{-1}(k_{pe}s + k_{ie})}{s^2 + C^{-1}k_{pe}s + C^{-1}k_{ie}} e_1^{ref}. \quad (2.52)$$

It must be highlighted that, under the considerations made, (2.46) and (2.52) are linear systems which do not depend on the initial operating conditions¹. The assumptions made are helpful to develop rules to select the controller parameters; however, when the assumptions are no longer considered, the system is actually nonlinear. The DVC which controls the energy of the VSC capacitor can be analyzed to show that. For instance, consider that the measurement P'_{12} can be modelled as a low-pass filter of P_{12} and also that P_{12} is equal $e_1 i_{12}$. In addition, if a Π model is considered for the dc cable, the dynamics of i_{12} have to be considered. Then, the state-space model of the VSC which control the direct-voltage is

$$\frac{de_1^2}{dt} = k_{pe} C^{-1} ((e_1^{ref})^2 - e_1^2) + k_{ie} C^{-1} n + 2C^{-1} P'_{12} - 2C^{-1} e_1 i_{12} \quad (2.53a)$$

$$\frac{dn}{dt} = (e_1^{ref})^2 - e_1^2. \quad (2.53b)$$

$$\frac{dP'_{12}}{dt} = -\gamma P'_{12} + \gamma e_1 i_{12} \quad (2.53c)$$

$$\frac{di_{12}}{dt} = -\frac{R_{12}}{L_{12}} i_{12} + \frac{1}{L_{12}} e_1 - \frac{1}{L_{12}} e_2 \quad (2.53d)$$

where γ is the bandwidth of device that measures the power P_{12} , n accounts for the integral term of (2.45). In this model, the states are e_1^2 , n , P'_{12} and i_{12} , and the inputs are e_1^{ref} and e_2 . Clearly, (2.53a) and (2.53c) are nonlinear since the term $e_1 i_{12}$ is the square root of the state e_1^2 multiplied by the state i_{12} . The same can be deduced when (2.52) is analyzed.

Another controller can be implemented if the proportional and the integral terms, without feedforward term, of the DVC is directly fed to the current reference $i_f^{d_{ref}}$ without the *feedback linearization* performed in (2.45) and (2.51). That is

$$i_f^{d_{ref}} = k_{pe} (e_1^{ref} - e_1) + k_{ie} \int_0^t (e_1^{ref} - e_1) dt \quad (2.54)$$

which is going to be used in the analysis performed in Chapter 4 and 5 for the sake of simplicity.

¹Note that the transfer functions (2.46) and (2.52) do not have terms which are related to operating points.

2.4.4 Active power control

The objective of the active power controller is to control the active power transfer over the VSC-HVDC system to the desired value. As mentioned in [21,26], the power controller can be implemented as a combination of an open-loop and feedback controller. The expression that defines the control law of the active power controller is

$$i_f^{dref} = \frac{P_g^{ref}}{u_g^d} + k_{pP} (P_g^{ref} - P_g) + k_{iP} \int_0^t (P_g^{ref} - P_g) dt. \quad (2.55)$$

A block diagram representing (2.55) is shown in Figure 2.18. In this thesis, however, the active power is controlled directly with the current reference i_f^{dref} without using the controller shown in Figure 2.18.

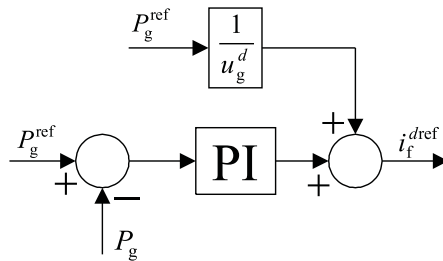


Figure 2.18: Active power controller.

2.4.5 Reactive power and alternating-voltage control

Similarly to the active power controller, the reactive power controller can be implemented as a combination of an open-loop and a feedback controller, as follows

$$i_f^{qref} = -\frac{Q_g^{ref}}{u_g^q} - k_{pQ} (Q_g^{ref} - Q_g) - k_{iQ} \int_0^t (Q_g^{ref} - Q_g) dt \quad (2.56)$$

which, likewise, is represented in Figure 2.19. The alternating-voltage controller can be

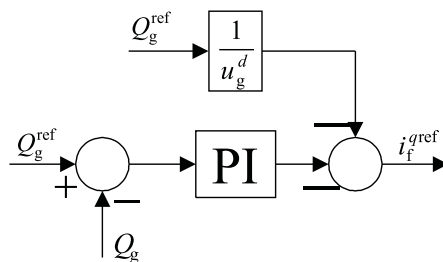


Figure 2.19: Reactive power controller.

implemented as a PI controller [26]

$$i_f^{qref} = k_{pU} (u_g^{ref} - |u_g^{dq}|) + k_{iU} \int_0^t (u_g^{ref} - |u_g^{dq}|) dt. \quad (2.57)$$

As assumed for the control of active power, the reactive power is controlled directly with the current reference i_f^{qref} without using the controller shown in Figure 2.19

2.5 New challenges for VSC-HVDC systems

In recent years, VSC-HVDC systems have been in the spotlight, particularly, due to the development of new converter topologies, and the proposal of using VSCs in MTDC configurations. The developers of the new multilevel topologies claim to have reduced the losses of VSCs to a level similar to the thyristor-based HVDC systems. Moreover, VSCs are considered suitable for MTDC configuration due to their versatile controllability features. In this section, both topics are briefly reviewed.

2.5.1 New multilevel topologies

The Modular Multilevel Converter (MMC), the Cascaded Two-Level converter (CTL) and the hybrid-HVDC-circuit topology described in [10–12], overcomes the lack of modularity of the NPC topology previously introduced. The MMC and CTL, illustrated in Figure 2.20, are similar topologies which builds up the voltage u_{ca} by inserting the submodules following a modulation method. The waveform generated by a twenty-module converter (ten modules in each arm) is shown in Figure 2.21. An eleven-level voltage is generated, and the harmonic spectrum shows that the harmonic level has decreased considerably compared to Figures 2.6 and 2.8. Apart from decreasing the harmonic content, the MMC reduces also the switching losses, since each submodule operates at lowers frequencies compared to the two and-three level converters. If the number of submodules is increased¹, the generated voltage waveform can be almost sinusoidal, so filters might become significantly small or even unnecessary.

The hybrid-HVDC-circuit configuration is described in [12]. It consist of a series connection of a two-level configuration and a H-bridge modules as illustrated in Figure 2.22. Basically, the idea is to use the two-level part of the converter to generate a low frequency voltage waveform and to use the H-bridges as active filter to shape the ac voltage waveform [13]. The main advantage of this topology compared to the MMC and CTL topologies is its performance in dc side faults. In case of dc side faults, the valves of the H-bridges will turn off in such a way that the converter stops feeding the fault. In the case of the MMC and CTL, a dc side fault will be fed through the diodes connected in anti-parallel with the valves.

¹According to [14], the Trans-Bay cable HVDC system has more than 200 modules per arm.

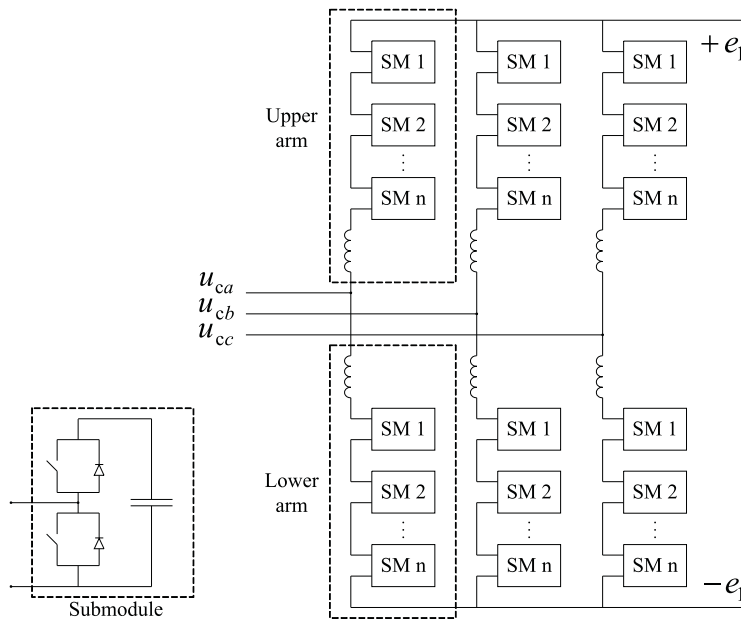


Figure 2.20: Modular Multilevel Converter [11].

2.5.2 VSC-based multi-terminal HVDC systems

An MTDC system can be defined as an HVDC system where more than two VSCs are interconnected through a common dc grid. Similarly to ac systems, in an MTDC system there might be a number of converters injecting power into the dc grid (analogously to generators in ac systems) and a number of converters absorbing power from the dc grid (analogously to loads in ac systems). Furthermore, some converters can be operated in voltage regulating mode, similar to the frequency-regulating generators that are operated in ac systems, i.e. compensating the unexpected “generation-load” mismatches. In that regard, it has been recognized in [30] that the control of the direct-voltage plays an important role on the power balancing task of the dc side. The following are the main conclusions from [30]:

1. Power unbalances in the dc system produces fluctuations in the direct-voltage of the system. If there is excess (deficit) of power going into the dc system, the direct-voltage will increase (decrease). Then, the direct-voltage can be used as an indicator of power unbalances in the dc side, as the frequency is used in the ac side.
2. The VSC which controls the direct-voltage acts as the slack generator in ac systems. It compensates the deficit or surplus of the power in the MTDC system.
3. The dynamics of the dc side is fast since capacitors are designed to store only a small amount of energy. Then, measures to compensate power unbalances should be taken automatically.

Using those principles, control strategies have been proposed in works such as [31–33]. The control strategies in the dc side aim at providing a back up to the direct-voltage control in case of contingencies such as faults in the ac side, or converter outages. The most basic control strategy in an MTDC is that one single VSC controls the direct-voltage while the

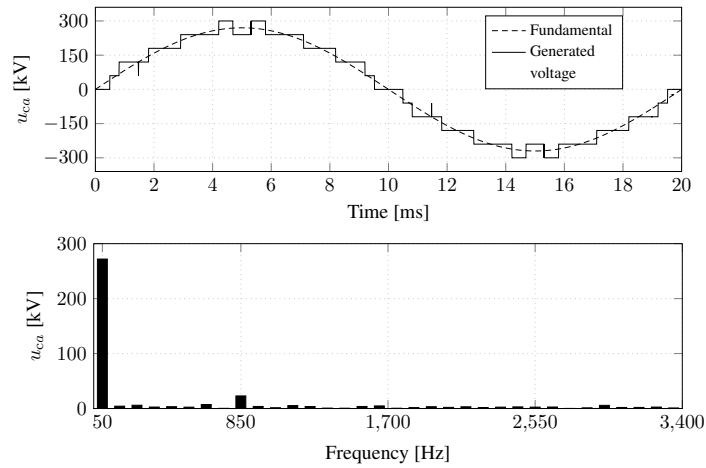


Figure 2.21: Voltage generated by a 20 module MMC through the SPWM. Upper: Generated voltage and fundamental component. Lower: Harmonic spectrum of the generated voltage.

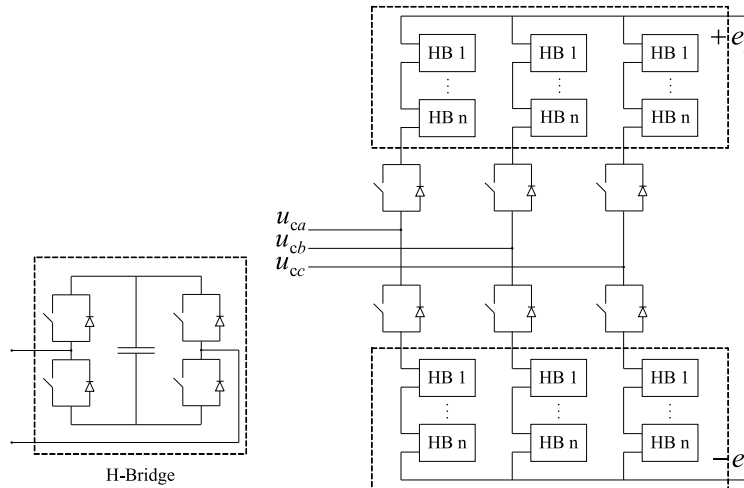


Figure 2.22: Hybrid-HVDC-circuit topology [12].

others control their power set-points to a fixed value. However, the disadvantage of such control strategy is that, if there is an outage of the only VSC which controls the direct-voltage, the voltages will either rise or drop in the dc system in a sustained way.

In Figure 2.23, a three-terminal HVDC system is shown. The system is composed of the VSC_1 , VSC_2 and VSC_3 , whose voltages at their dc side nodes are e_1 , e_2 and e_3 , respectively. Moreover, the VSC_1 , VSC_2 and VSC_3 transfer the powers P_1 , P_2 and P_3 to the dc grid, where a positive value means that the converter “supplies” power to the dc grid, while a negative value means the converter “consumes” power from the dc grid. This setup is used to explain the voltage-margin control and the voltage-droop control strategies.

The voltage-margin control strategy has been presented in [31, 32]. As an example, in Figure 2.24, the voltage-power characteristic of each VSC (in the system from Figure 2.23) would follow under the voltage-margin control strategy. According to Figure 2.24, VSC_1 is consuming 300 MW, VSC_2 is supplying 100 MW, and VSC_3 is supplying 200 MW

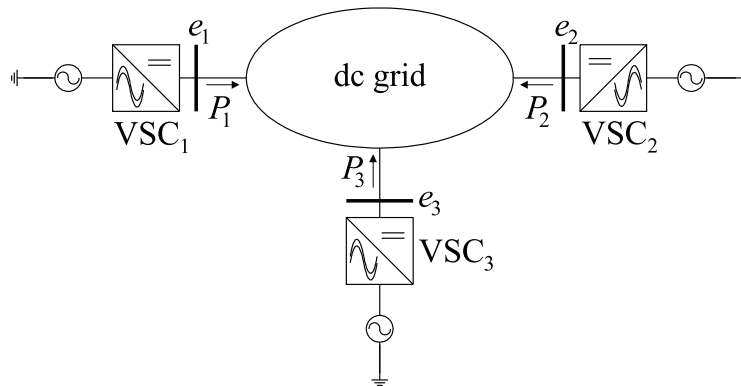


Figure 2.23: Three-terminal HVDC system.

(assuming a lossless dc grid). According to the voltage-margin control, if the converter VSC₁ is lost, VSC₂ and VSC₃ will continue supplying 300 MW together. As stated earlier in this section, this surplus of power will make the voltage of the dc grid to increase. From the figure, it can be seen that VSC₃ will change from a constant power control mode to a direct-voltage control mode when the voltage at its dc-node increases to e_{03} . Finally, after the outage of VSC₁, VSC₂ will be supplying 100 MW, and VSC₃ will be consuming 100 MW and will be controlling the direct-voltage of the system.

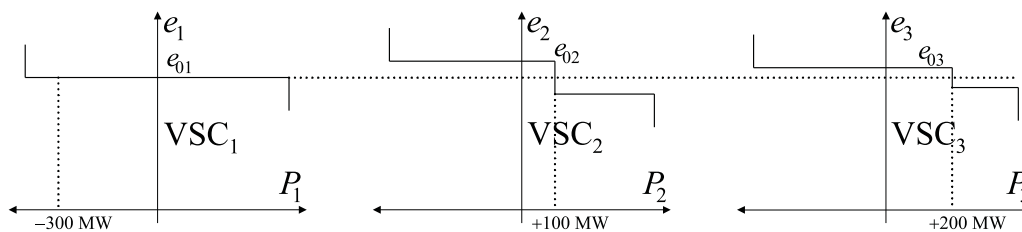


Figure 2.24: Voltage-margin control strategy with $e_{01} < e_{03} < e_{02}$.

The disadvantage of this method is that, only one converter is exposed to large variations of power in case of contingencies. In our example, VSC₃ has to change from +100 MW to -200 MW which means that a fast variation of a 300 MW will be experienced in the VSC₃'s ac side.

In order to overcome the disadvantage of the voltage-margin control, the voltage droop-control is proposed in [33, 34]. A voltage-droop control strategy for the studied three-terminal HVDC system is shown in Figure 2.25. In this scheme, if VSC₁ is suddenly out of service, the voltage will rise in the dc system, and the power output of VSC₂ and VSC₃ will change according to the voltage-power characteristics shown in Figure 2.25 the voltage will rise until the power in the dc-system is balanced. The advantage of this method is that, the balance of the power is performed by the two remaining converters instead of only one. However, the disadvantage is that the final power set-points are uncontrolled. One method to control the power after the contingency is proposed in [57]. In Figure 2.26 the principle of the method is illustrated. Basically, the power can be controlled by changing the *no-load voltage* of the voltage-droop characteristic. For instance, if the power output of

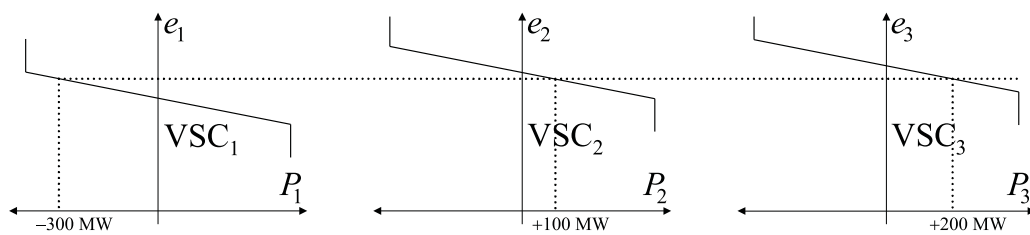


Figure 2.25: Voltage-droop control strategy.

a converter is -300 MW after the contingency, it can be changed to -100 MW (if desired) by increasing the no-load voltage value of voltage-droop characteristic.

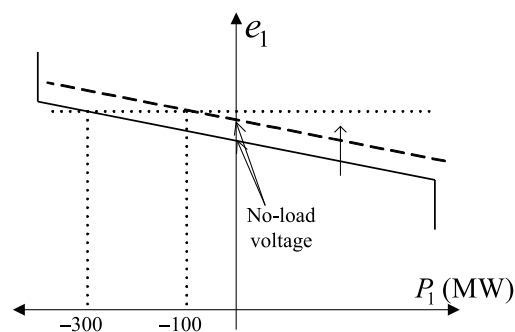


Figure 2.26: Autonomous power control.

Through solving the problem of the power balance in the dc side of an MTDC system, some control strategies have been proposed. However, an MTDC is a system which is composed of complex elements such as the VSC and the dc grid. The dynamics of a VSC, for example, depends on the control structure which, likewise, has to do with the selection of the control strategies proposed in this section. The dc grid on the other hand, is composed by cables and overhead transmission lines, which shows a resonance behaviour in certain conditions. Then, along with considering the power balance issue, the dynamic interactions between elements that conform the MTDC have to be studied when developing a control strategy for MTDC systems.

2.6 Conclusions

In this Chapter, a basic theory on VSC-HVDC systems has been presented. The functions of the main components of a VSC, together with their typical ratings has been summarized. The operating principles of the VSC have been presented and the SPWM modulation method has been introduced. Then, a typical control system of the VSC has been described with a special stress on the derivation of the vector current controller and the direct-voltage controller, and the selection of their parameters. Finally, the new challenges for VSC-HVDC system, regarding new converter topologies and the control of multi-terminal HVDC systems, have been presented.

Chapter 3

Overview on dc network dynamics

Considerable research effort on the subject of control and stability of dc networks can be found in the literature [31–38,49,50,52]. On a low power level, it has been recognized that constant power loads (CPLs) in dc microgrids introduce an incremental negative resistance, which can be detrimental for the dynamic performance of the system. Various analysis methods and control strategies have been proposed to overcome the instability introduced by CPLs. On the high power level, several works have been carried out concerning the stability of HVDC systems, however, with emphasis on the ac side dynamics rather than the dc side of the system. The interest on the dc side dynamics has risen when MTDC systems have come into the scene, since the conditions in MTDC are more variable than in point-to-point HVDC systems. The small signal analysis has been used, mostly to assess the effect of the operating conditions and the controller parameters on the stability of the studied MTDC systems.

In order to get an idea of the challenges that brings HVDC systems from the dynamics perspective, a review of publications on the dynamic analysis of dc microgrids and HVDC systems has been carried out. The main findings from the review are presented in this chapter.

3.1 Dynamic issues in dc microgrids

Multi-converter power electronic systems, in the form of dc microgrids, have been a subject of research for some years. In [36], for instance, definitions and applications of multi-converter power electronics systems are presented. Proposed dc microgrids configurations for automotive power systems, electric and hybrid vehicles, aircraft power systems, and space power systems are presented as examples. As shown in Figure 3.1, a dc microgrid is typically composed of a number of converters connected to a common bus. Those converters interface either power sources or loads or can be used to interconnect systems of different voltage levels. From the dynamic point of view, the challenges in multi-converter systems, as stated in [36], ranges from system modelling, dynamic assessment and control.

CPLs have been recognized as the main source of instability in dc microgrids [35–40]. As pointed out in [38], a CPL can be a DC/DC converter which tightly regulates its output voltage with a passive load connected to its output. In this case, since the load voltage is maintained constant, the current is constant as well, therefore, seen from the dc bus, the DC/DC converter acts as a constant power load. Another example of a CPL is a DC/AC inverter regulating the speed of a motor. If the speed is maintained constant and considering a constant torque, the power seen from the input is also constant. Figure 3.2 shows a sketch of the two examples mentioned.

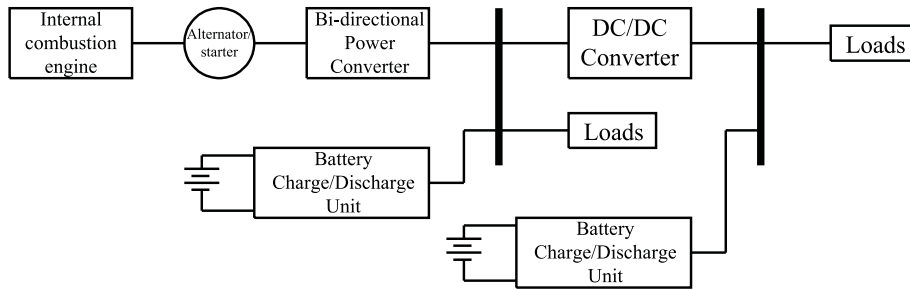


Figure 3.1: Architecture of a power electronic system for automotive applications [36].

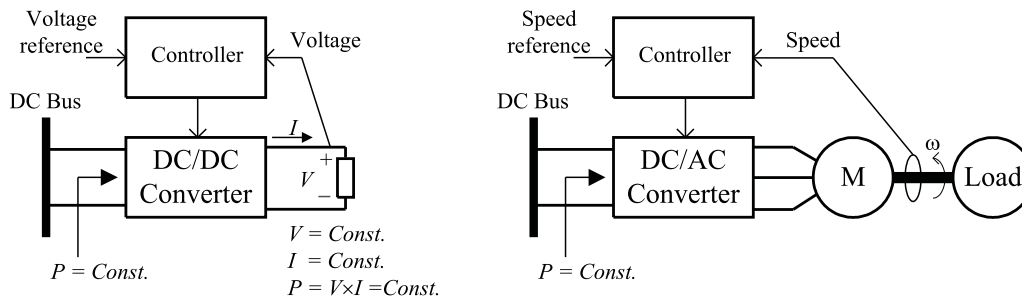


Figure 3.2: Typical CPLs. Left: a DC/DC converter regulating the voltage at its output. Right: a DC/AC inverter regulating the speed of a motor [38].

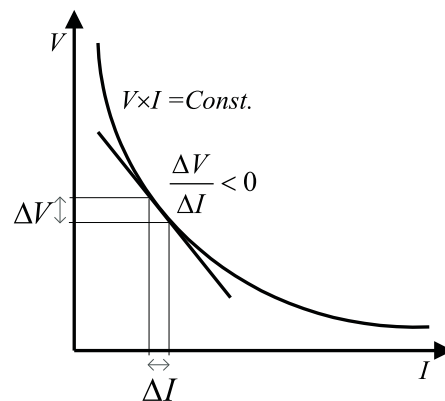


Figure 3.3: Incremental negative impedance of CPLs [38].

Although the instantaneous impedance of a CPL is positive, the incremental impedance is negative as illustrated in Figure 3.3. That is, if there is a decrease voltage at the DC bus, there will be an increase of current drawn from the converter in order to maintain a constant power. As an example of the influence of a CPL on the stability of a dc system, a buck converter supplying power to a resistive load and a CPL (both connected in parallel) is studied in [35]. From Figure 3.4, and using the averaging technique, the following are the equations that describe the dynamics of the studied circuit.

$$\frac{di_L}{dt} = -\frac{R}{L}i_L + \frac{1}{L}d \cdot E - \frac{1}{L}e_c \quad (3.1)$$

$$\frac{de_c}{dt} = \frac{i_L}{C} - \frac{e_c}{CR_L} - \frac{P_L}{Ce_c} \quad (3.2)$$

where d is the duty cycle of the buck converter, i_L is the current through the filter inductor,

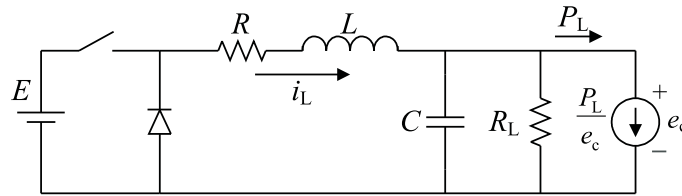


Figure 3.4: Buck converter supplying power to a resistive load and a CPL [35].

C is the filter capacitor, R is the inductor resistance, L is the inductance inductor, E is the main source voltage, e_c is the load voltage, R_L is the resistance of the resistive load, and the P_L is the constant power load. Equations (3.1) and (3.2) can be linearized around an operating point. From the linearized equations the state space model of the system is

$$\frac{d}{dt} \begin{bmatrix} \Delta i_L \\ \Delta e_c \end{bmatrix} = \begin{bmatrix} -\frac{R}{L} & -\frac{1}{L} \\ \frac{1}{C} & \frac{P_T}{Ce_{c0}^2} \end{bmatrix} \begin{bmatrix} \Delta i_L \\ \Delta e_c \end{bmatrix} + \begin{bmatrix} \frac{d_0}{L} & \frac{E_0}{L} \\ 0 & 0 \end{bmatrix} \begin{bmatrix} \Delta E \\ \Delta d \end{bmatrix} \quad (3.3)$$

where d_0 is the initial duty cycle, E_0 is the initial source voltage, e_{c0} is the initial output voltage, and $P_T = P_L - e_{c0}^2/R_L$. The poles of the system are then

$$\lambda_{1,2} = -\frac{1}{2} \left(\frac{R}{L} - \frac{P_T}{Ce_{c0}^2} \right) \pm \frac{1}{2} \sqrt{\left(\frac{R}{L} + \frac{P_T}{Ce_{c0}^2} \right)^2 - \frac{4}{LC}}. \quad (3.4)$$

If the term inside the square root is negative, then, the system is stable if

$$P_L < \frac{e_{c0}^2}{R_L} + Ce_{c0}^2 \frac{R}{L}. \quad (3.5)$$

If the inductor is considered lossless, then, from (3.5) the condition for stability is that the amount of CPLs should be lower than the amount of resistive loads. This principle is illustrated in [37] and [38]. In [35], the principle is extended to a multi-converter system in which the principle is generalized. A multi-converter system is claimed to be stable as long as

$$\sum P_{\text{Constant power loads}} < \sum P_{\text{Resistive loads}} \quad (3.6)$$

Going back to (3.5), if there is no resistive load, the maximum power that a CPL can be supplied is given in terms of C , R , L and e_{c0} . From (3.5), if C is increased, the stability limit is also increased as proposed in [39]. Other measures to avoid instability such as load shedding or the addition of a bulk energy storage device are also proposed in [39]. Advanced methods, such as sliding-mode control, and feedback linearization are proposed in [38] as solutions to stabilize the system.

A frequency domain approach is proposed in [40] and [41]. The so-called *immittance* analysis is preferred over the eigenvalue calculations since it provides design specifications to be fulfilled by the load. The basic idea can be explained with the help of Figure 3.5. The method consist, first, of calculating the source impedance Z_S and the load admittance Y_L in terms of the frequency for all operating points. Then, based on the Nyquist criterion, some stability criteria are defined. Basically, the curve defined by $Z_S(j\omega)Y_L(j\omega)$ for all frequencies should not intersect a certain *forbidden* region in the s -plane. Figure 3.6 shows three criteria which are described in [40]. Figure 3.6(a) shows the Middlebrook criterion where the forbidden area is the area outside dashed circle meaning that the contour defined by $Z_S Y_L$ should remain inside the dashed circle. If the source impedance Z_S is given, then, according to the criterion, Y_L should be shaped to meet the Middlebrook criterion. It is claimed in [40] that the Middlebrook criterion is a conservative method, since, according to the Nyquist criterion, the only condition for the system to be stable is that the contour defined by $Z_S Y_L$ should not encircle clock-wise the real axis to a point lower than -1 . The Gain Margin and Phase Margin (GM/PM) criterion shown in Figure 3.6(b) is a less conservative method, since it allows the contour $Z_S Y_L$ to be located in a larger area of the s -plane. An even less conservative method is the ESAC criterion shown in Figure 3.6(c) where the forbidden area is even smaller.

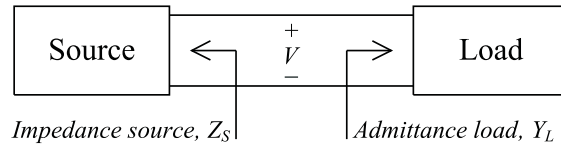


Figure 3.5: Equivalent source and load of a dc microgrid [40].

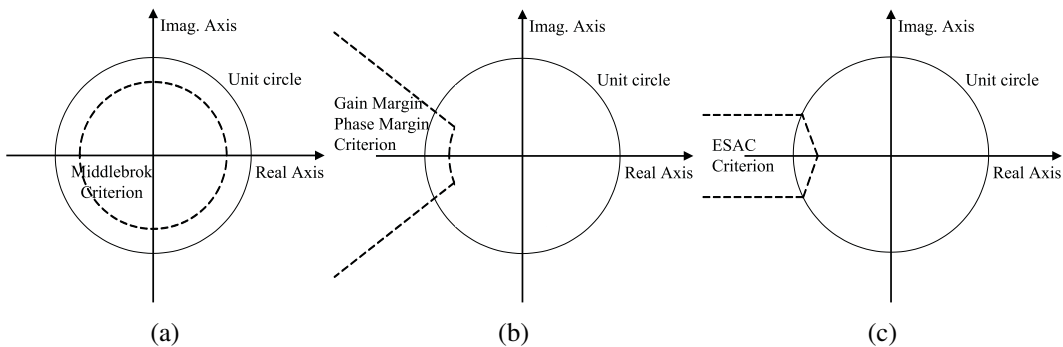


Figure 3.6: Stability criteria [40]. (a) Middlebrook criterion. (b) Gain margin phase margin criterion. (c) ESAC criterion.

Another interesting work is [42] where the load characteristic is investigated. The load dynamics is studied taking into consideration the controller and the load dynamics together instead of the sole simplification of a CPL. It is found that the load can have other destabilizing forms depending on the load characteristic and the controller design. The load impedance can have unstable poles or zeros in the right-half plane (RHP) which impose limitations in the control system. If the load has unstable poles, the system needs a feedback controller to stabilize the system. On the other hand a non-minimum phase load can cause instability if the controller gain is high.

Although there are significant differences with HVDC systems, such as power and voltage ratings, there are similarities on the electrical configuration and control structure. The following aspects, where dc microgrids and HVDC systems are comparable, are summarized next:

1. The studied dc microgrids are converters connected to a common dc bus, while the converters in HVDC systems are interconnected through dc transmission lines. However, the filter configuration (composed of inductors and capacitors) of the dc microgrid's converter resembles the dc transmission lines of HVDC systems.
2. In dc microgrids, CPLs are considered as the main source on instability. Furthermore, the converter control structure and the load characteristic can have destabilizing forms such as unstable poles or zeros in the RHP. In HVDC systems, if the control system dynamics and the converter dynamics are considered, the load (inverter) or the source (rectifier) connected to the dc grid (transmission line) can also have destabilizing forms in the dc side.
3. Methods developed for the analysis of the dc microgrids, based of the averaging techniques, eigenvalue analysis, and frequency domain analysis can be adapted for HVDC systems.

3.2 Dynamic issues in VSC-HVDC systems

In this section, a literature review on HVDC system dynamics is presented. The section starts with an investigation of the dynamics concerns of HVDC systems from the ac side perspective. Then, two studies on the interaction between VSCs and the dc side of the system are presented. Finally, works on the analysis of the dc side dynamics of VSC-MTDC are reviewed.

The control structure illustrated in Figure 3.7 has been used in most of the reviewed publications. The controllers are implemented in the dq frame and with PI controllers, similarly to the ones presented in Section 2.4. For the sake of uniformity, the variable names used in the publications discussed in this section are adapted to the ones shown in Figure 3.7.

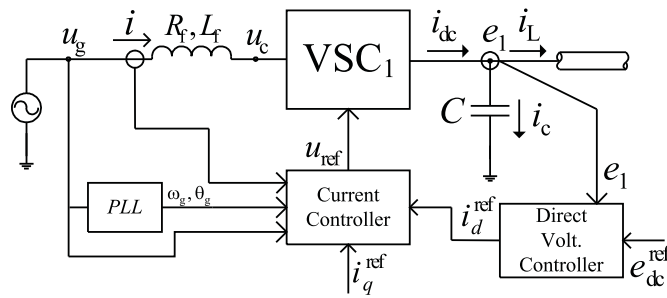


Figure 3.7: Sketch of the control structure of a VSC.

3.2.1 AC side dynamics of VSC-HVDC

Surprisingly, the dynamic analysis of the dc side of VSC-HVDC systems has not been a subject widely investigated. HVDC systems have been rather viewed as means to overcome the weaknesses of the existing ac system. An example of that is [43], where supplementary functions are designed for a VSC-HVDC system. The aim of the supplementary functions is the mitigation of dynamic problems of ac system, such as power oscillation and transient stability. Typically, in such works, electromechanical dynamics from the generators and motors connected to the ac system are of interest rather than the fast dynamics that takes place at converter controllers and the dc side of the system. In most of the cases, fast dynamics are neglected by representing the HVDC system as active and reactive power injections to the ac system with the dc network dynamics neglected.

The stability of VSC-HVDC systems is investigated in [44] and [45] focusing on the interaction between the converter and the ac grid to which they are connected. The input impedance of the converter seen from the ac bus, as illustrated in Figure 3.8, is calculated in [44]. There, it is shown that the input admittance shows a negative conductance characteristic at low frequencies. This negative conductance can amplify low frequency resonances originated in the ac system, as shown in [44], where a series compensated line is studied (see Figure 3.8). The impact of the dc side of the system on the converter input admittance is studied as well. However, only a capacitor is considered to be connected on the dc side and not a dc transmission line. Moreover, experiments are performed where only the converter is connected to an ac system. In some tests, there is a strong dc source in the dc side of the VSC, while in other tests, there is a capacitor in parallel with a resistor.

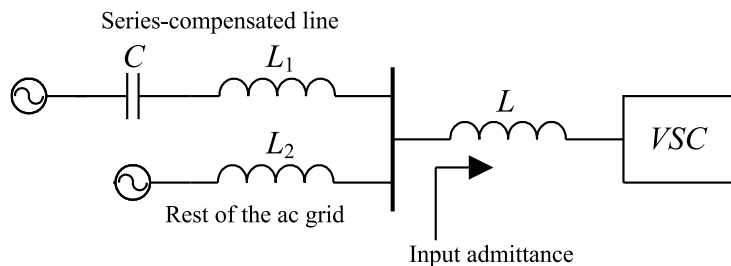


Figure 3.8: Series compensated line and the input admittance of the VSC [44].

In [46], the operation of VSC-HVDC systems connected to weak ac systems is investigated. The power-synchronization control (PSC) approach is proposed as an alternative to the VCC. In the PSC, the control of active power is performed by adjusting the phase angle of the alternating-voltage generated by the converter, θ_c , while the magnitude of the voltage u_g is controlled with the magnitude of the alternating-voltage generated by the converter, u_c , (Figure 3.7 can be used as a help). In the VCC, the active power is controlled with the d component of the current and the magnitude of the voltage u_g is controlled with the q component of the current. In the analysis, the so-called *Jacobian*¹ transfer matrices are derived for both, the VCC and the PSC, and it is found that, for low short-circuit ratios and high power transfers, cross-coupling interactions are more considerable in the VCC compared to the PSC. That is, in the mentioned conditions, a change of the d component of the current affects more the voltage u_g compared to a change in the phase angle of θ_c .

The dc side of the system is analyzed to some extent in [46]. The *Jacobian* transfer matrix of the dc grid (the cable) is derived and it is found that it is unstable. The unstable pole means that the bandwidth of the direct-voltage controller should be higher than the unstable pole. Concerning the direct-voltage control, it is design as a PI controller and the gains are designed in terms of the desired closed-loop bandwidth and the capacitor size. Furthermore, the capacitor size is specified considering the maximum allowed overvoltage and the capacitor charging time.

3.2.2 DC side dynamics of VSC-HVDC

Attempts to investigate the dynamics of the dc side of the HVDC system are [47] and [48]. In [47], the effects of the injection of harmonics into a dc cable is investigated. The admittance of the dc cable is calculated and the resonance peaks and the corresponding frequency are identified for different lengths. The harmonic content of the current injected by the converter into the dc cable is calculated as well. In a particular example presented in [47], the resonance frequency of a 30 km cable is 3 kHz and one 3 kHz harmonic component is found for a switching frequency of 1.5 kHz. It is claimed that simulations in those conditions are unstable, although, the simulation results are not shown. In [48], the VSC model is simplified into a single-input-single-output system (SISO). The model is developed in the dq frame, and, after some simplifications, the influence of the current i_q and the voltage v_{cq} is decoupled from the direct-voltage e_1 resulting in the model illustrated in Figure 3.9. It is found that the transfer function $e_1(s)/i_d(s)$ has a zero in the RHP which impose a limitation on the performance of the closed-loop control system. Basically, a RHP zero limits the achievable bandwidth of the closed-loop system. Experimental results show that the frequency response of a converter matches closely the theoretical results of its corresponding simplified model.

It is clear that the research on the dynamics of VSC-HVDC systems has been driven more by the interest on the interaction between the VSCs and the ac systems to which they are connected. In contrast to the dc microgrid case, the dc side dynamics has been overlooked to some extent in point-to-point VSC-HVDC systems, most likely, due to the foreseeable

¹It should be highlighted that the *Jacobian* transfer matrix it is not the matrix composed by the all the partial derivatives of a vector-valued function.

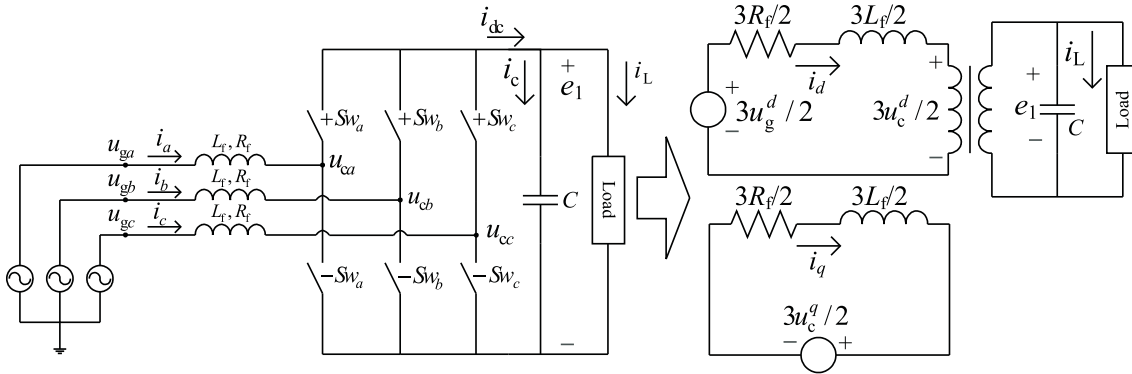


Figure 3.9: One simplified model of a VSC [48].

operating modes of such configurations. However, in MTDC systems, operating conditions are expected to be changeable, particularly, if renewable energy sources are connected to the system. Moreover, the topology of the dc grid is not going to be fixed, as in point-to-point VSC-HVDC systems. Cables can be disconnected due to maintenance or faults changing the dynamic properties of the dc grid. Thus, the question of whether undesirable interactions between VSCs and the dc grid takes place in MTDC systems is relevant and has become a subject of interest, as shown next.

3.2.3 DC dynamics in multi-terminal VSC-HVDC systems

The small-signal modelling approach has been mainly used when investigating the dynamic performance of MTDC systems. A decade ago, in [49], the stability of VSC-MTDC has already been studied using eigenvalues analysis. Instability in the form of sustained oscillations in the dc side is found. In order to investigate the origin of the oscillations, a small-signal model of a point-to-point VSC-HVDC system, sketched in Figure 3.10(a), is developed in [49]. The poles of the system are then calculated and it has been found that unstable poles appear when the VSC₂ (which controls power) transfers power from the dc side to the ac side. Moreover, the unstable poles are found to be related to the dc side dynamics, i.e. the resonance phenomenon which occur in the dc cable. According to the author, the instability is caused by the CPL-like behaviour of the VSC₂. As explained in Section 3.1, a CPL introduces a negative incremental resistance which may amplify the resonance originated from the dc cable. A solution proposed in [49] is to add an RLC circuit, tuned to the resonance frequency, at the dc side of the VSC₂, as shown in Figure 3.10(b).

Other examples of the use of the small signal modelling approach are [50–52]. In [50, 51], the stability of VSC-MTDC systems is investigated through the calculation of the eigenvalues of the systems's linearized model. The effect of different controller parameters on the poles location of the system is investigated. In [50], the effects of the droop setting of the direct-voltage controller k_{droop} (see Figure 3.11), is investigated. In this work, apparently, the ac systems are considered strong, since the PLL dynamics is not mentioned in the model of the VSC. The results indicate that high values of k_{droop} turn the studied point-to-point system unstable. The investigation carried out in [51] deals with the study

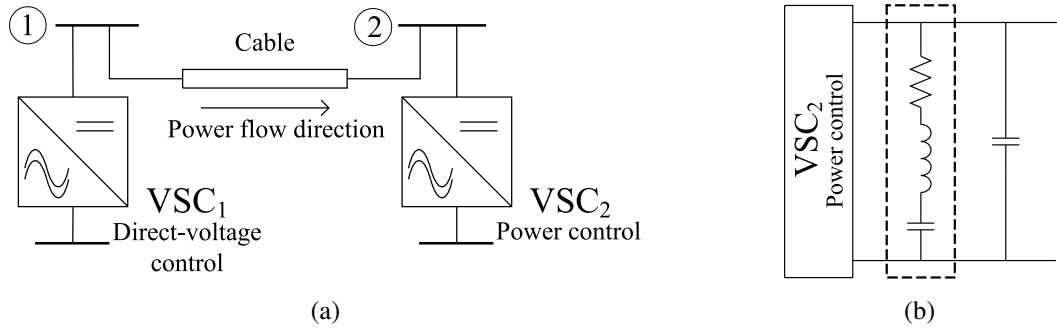


Figure 3.10: (a) Point-to-point VSC-HVDC system. (b) Damping filter proposed in [49].

of a four-terminal VSC-MTDC system, with two-level converters connected to the main ac system, and the other two connected to wind farms. The influence of different controllers loops (alternating-current controller, direct-voltage controller, alternating-voltage controller) in the stability of the system is studied. The controllers are implemented as PI controllers and the ranges in which the gains can be varied without losing stability are calculated. Similarly to [50], for the direct-voltage controller, there is a lower and upper limit in which the proportional gain (corresponding to the droop setting in [50]) can be varied. Again, in [52], VSC-MTDC systems are linearized and the different control structures are investigated through eigenvalue analysis. One thing to highlight is that, in [50–52], the influence of the operating point on the stability of the VSC-MTDC system is not investigated.

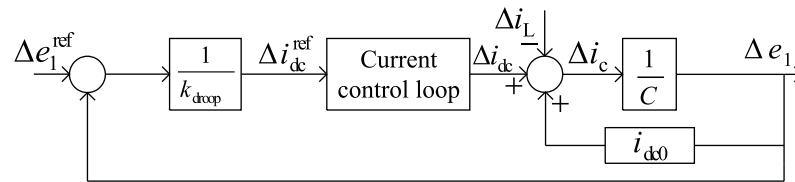


Figure 3.11: Simplified block diagram of the direct-voltage controller [50].

From this review, it has been shown that the interest in dynamics of VSC-HVDC has been driven more by the analysis of the ac side rather than the dc side of the system, where only a few references can be found. With VSC-MTDC, the dc side dynamics has become a relevant subject, and the main findings from the review are summarized next:

1. There is a risk of instability originated from the dc side of the system. From the reviewed literature, sustained oscillations appear when the power flows from the converter which controls the direct-voltage to the converter which controls the power. Moreover, it has been found that the instability is related to the resonance phenomenon of the dc cable.
2. Through eigenvalue analysis, it has been shown that the size of the controller gains, also influences on the stability of the system. Too low or too high gains can turn the system unstable. Moreover, [48] has found a RHP zero in the converter transfer function which may be the reason why the system becomes unstable for high gains.

Then, as pointed out in [42], there might be destabilizing forms that the VSC can have under certain conditions.

3. Eigenvalue analysis shows that unstable scenarios, which are originated from the dc side of the system, may occur. However, to the best of the author's knowledge, no rigorous analysis has been carried out on explaining the origin of the dc side instability. In [49], the dc side instability is attributed to the CPL-like behaviour of the VSC which controls the power, however, no clear evidence has been provided.

In the following section, as an introduction to the problem, a point-to-point VSC-HVDC system is investigated through simulations.

3.3 Study of an ideal case

The purpose of this section is to explore the effect of the operating points, the controller parameters, and the dc side electrical topology on the stability of a point-to-point VSC-HVDC system. The system under study is sketched in Figure 3.12 and the control system is implemented as presented in 2.4. In this case, VSC₁ is set to control the direct-voltage, while VSC₂ is set to control the active power. Table 3.1 and Table 3.2 summarize the main data used in the simulations. The system is modeled in PSCADTM.

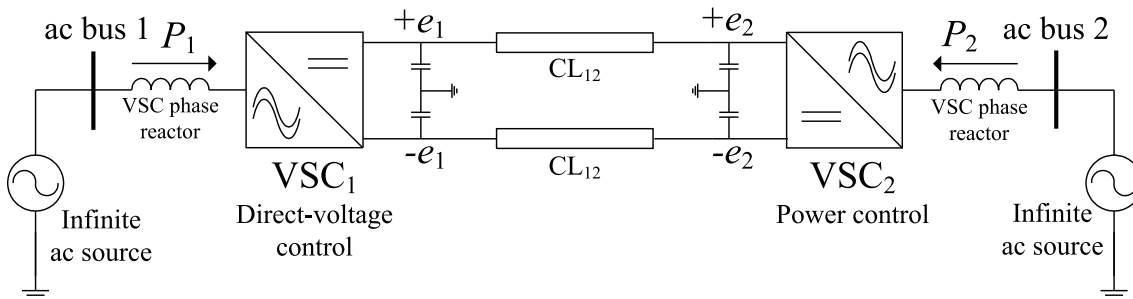


Figure 3.12: Point-to-point VSC-HVDC system under study.

The ac sources to which the converters are connected are assumed to be infinite, so, the unstable cases found are only related due to the interaction between the converters and the dc side dynamics. In other words, with this assumption, the ac side of the system cannot be blamed when unstable cases take place.

The effect of the operating point is evaluated through varying the power transfer between both VSCs. The effect of controller parameter is evaluated for two values of the proportional gain of the DVC, k_{pe} , and the effect of the dc side electrical topology is evaluated with different lengths of the dc cable. The studied cases are listed as follow:

Case 1.1: Ramp up of power from zero to 600 MW with the direction of the power from VSC₁ to VSC₂. The cable length is 50 km.

Table 3.1: Converter Ratings

| Rating | Value |
|--------------------------|----------------|
| Rated Power | 600 MVA |
| AC rated voltage | 300 kV |
| DC rated voltage | ± 300 kV |
| Phase reactor inductance | 0.12 mH |
| Phase reactor resistance | 0.375 Ω |
| Capacitor per pole | 33.33 μ F |

Table 3.2: CL₁₂ Cable Data

| Parameter | Value |
|-------------------|--------------------|
| Cable capacitance | 0.207 μ F/km |
| Cable inductance | 0.189 mH/km |
| Cable resistance | 0.038 Ω /km |

Case 1.2: Ramp up of power from zero to 600 MW with the direction of the power from VSC₂ to VSC₁. The cable length is 50 km.

Case 2.1: Repetition of **Case 1.1** with a higher proportional gain k_{pe} of the DVC.

Case 2.2: Repetition of **Case 1.2** with a higher proportional gain k_{pe} of the DVC.

Case 3.1: Repetition of **Case 2.1** with a cable length of 100 km.

Case 3.2: Repetition of **Case 2.2** with a cable length of 100 km.

It should be highlighted that, in a two-terminal VSC-HVDC system, the typical control strategy is to set the sending VSC to control the direct-voltage, while the receiving VSC to control the active power, as illustrated in Figure 3.13. However, in this thesis, it is always assumed that the same VSC controls the direct-voltage regardless of the direction of the power. This is to investigate the effect of the whole range of power variation on the control system of the VSC. That means that, in all the above mentioned cases, VSC₁ controls the direct-voltage, and the power transfer is ramped-up or ramped-down by controlling the power at VSC₂.

The results are shown in Figures 3.14, 3.15, 3.16, and 3.17 where the direct-voltage, e_1 , and the active power, P_1 , are plotted for each case. Figure 3.15 shows the Cases 1.1 and 1.2 where the last instants before reaching 600 MW (in both directions) is shown. It can be seen that the system is able to reach the “steady state” without any inconvenience. Figure 3.16 shows the Cases 2.1 and 2.2, where the proportional gain of direct-voltage controller has been increased. Figure 3.16(a) show that, in Case 2.1, the system turns unstable when the power almost reaches 600 MW, with the direction of the power from VSC₁ to VSC₂. However, Figure 3.16(b) shows that when the power flows in the opposite direction, the system manages to reach 600 MW without problems. Finally, the results from the Cases 3.1 and 3.2 are shown in Figure 3.17. It can be seen that the unstable case, produced in Case 2.1 due to the high gain k_{pe} , does not occur in Case 3.1, when the dc cable is longer.

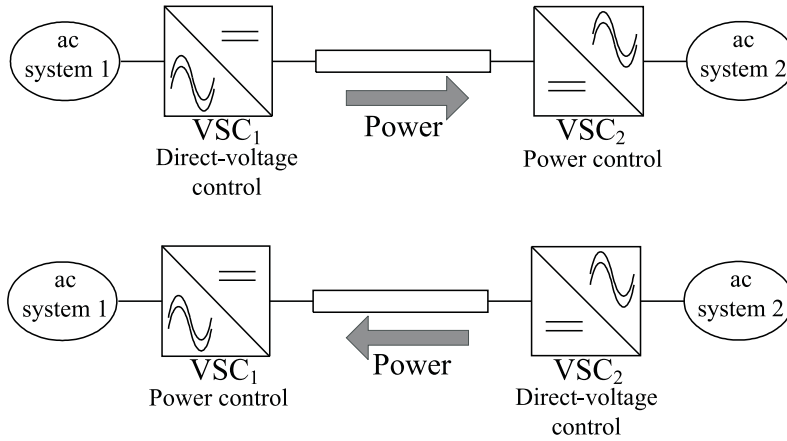


Figure 3.13: Typical control strategy in a point-to-point VSC-HVDC system. Upper: Control strategy for a power flow direction from the ac system 1 to the ac system 2. Lower: Control strategy for a power flow direction from the ac system 2 to the ac system 1

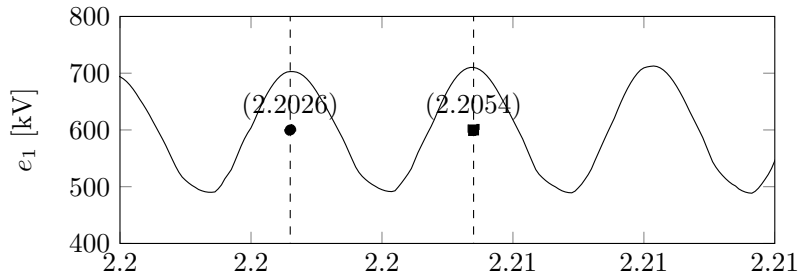


Figure 3.14: Detail of the direct-voltage e_1 from case 2.1.

Figure 3.14 shows a zoomed picture of the direct-voltage e_1 between 2.20 s and 2.21 s. It can be seen that there is an oscillation with a period of approximately 2.8 ms, which corresponds to a frequency of around 357 Hz. Considering a lossless Π model of the dc cable, the resonance frequency is given by

$$f_{\text{res}} = \frac{1}{2\pi\sqrt{LC/2}} \quad (3.7)$$

where L is the inductance of the cable, and C is the cable capacitance together with the converter capacitor per pole. For a cable length of 50 km, L is 9.43 mH, and C is 43.67 μF . With these values, the resonance frequency, f_{res} , is around 350.7 Hz, which is very close to the frequency found from Figure 3.14. Then, it can be inferred that the instability takes place when the dc side resonance phenomenon becomes amplified by a mechanism that should be investigated.

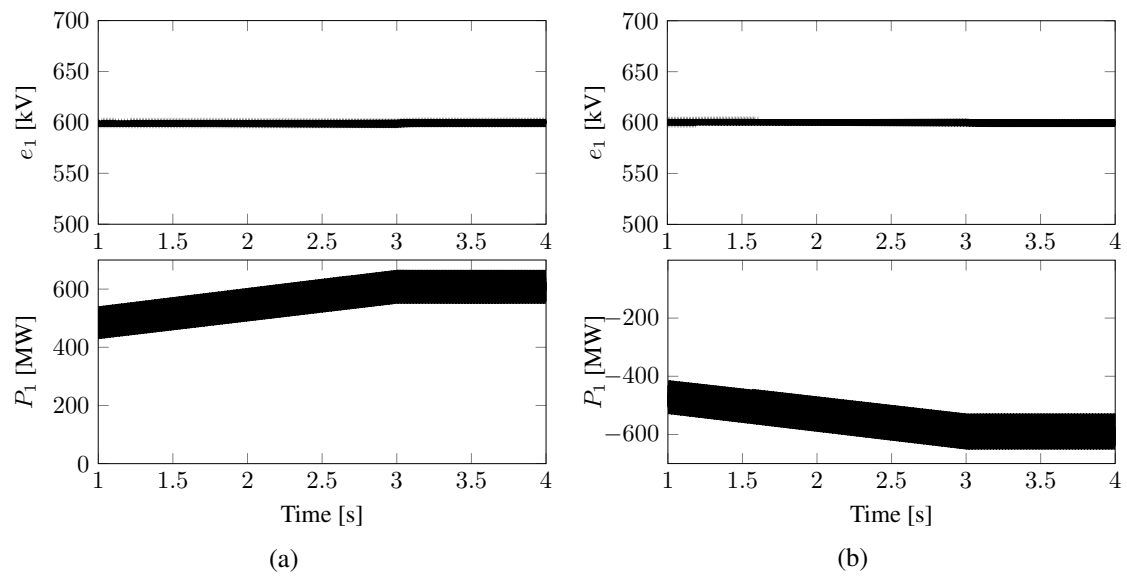


Figure 3.15: Simulation results of Case 1. (a) VSC₁ direct-voltage and power of Case 1.1. (b) VSC₁ direct-voltage and power of Case 1.2

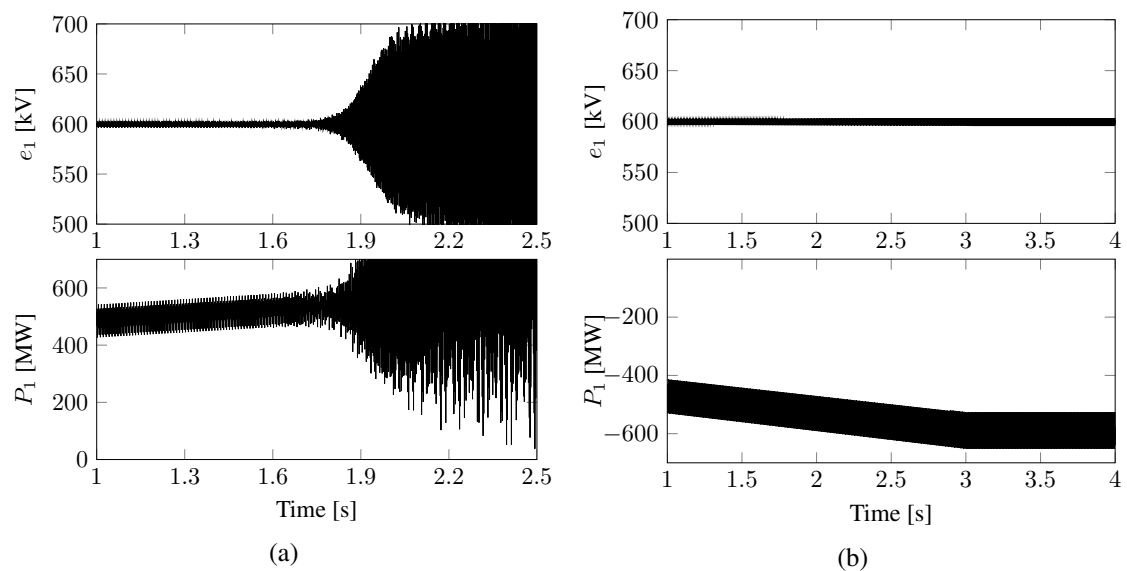


Figure 3.16: Simulation results of Case 2. (a) VSC₁ direct-voltage and power of Case 2.1. (b) VSC₁ direct-voltage and power of Case 2.2

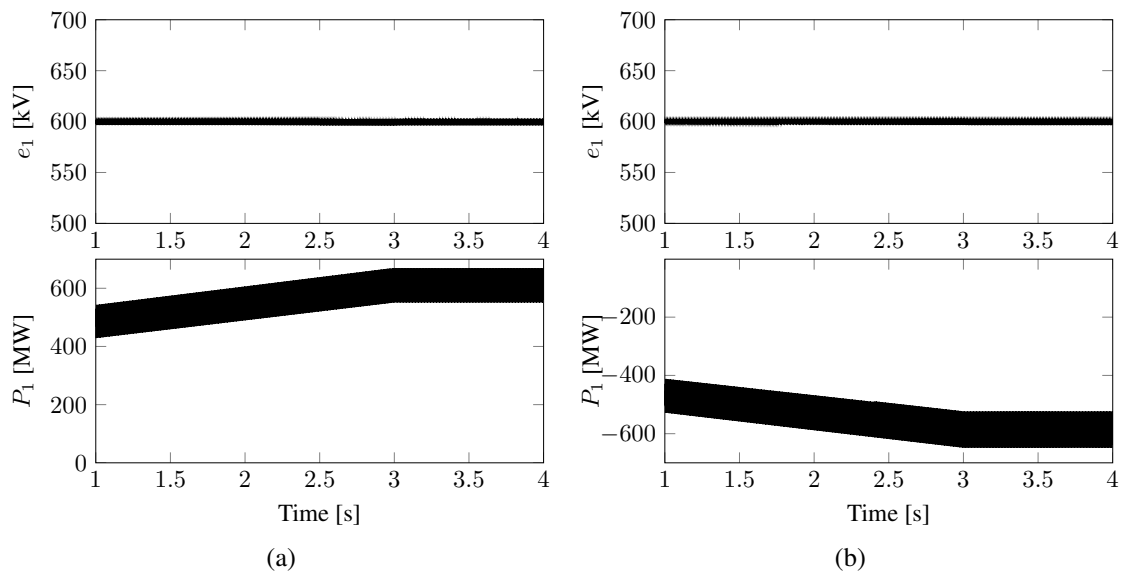


Figure 3.17: Simulation results of Case 3. (a) VSC₁ direct-voltage and power of Case 3.1. (b) VSC₁ direct-voltage and power of Case 3.2

3.4 Conclusions

In this chapter, an overview on the dynamic of dc microgrids and HVDC systems has been presented. In dc microgrids, CPLs has been recognized as the main source of instability. Other sources of instability are the destabilizing form of power electronic loads, such as unstable poles or zeros in the RHP. In HVDC systems, the interest is mainly focused on the interaction between the converter and the ac side to which it is connected. Since MTDC systems has been lately proposed, the interest of the stability of the dc side of the system has captured more attention. Several works have found, through eigenvalues analysis, that the operating point, the converter dynamics characteristics, and the topology of the dc side play a major role in the stability of MTDC systems. Moreover, in Section 3.3, an ideal case has been studied confirming the findings of other authors, where it has been shown also that the instability is related to the resonance phenomenon produced in the dc cable.

Although interesting conclusions have been obtained through eigenvalue analysis, the source of the instability in VSC-HVDC systems has not been properly identified yet. Thus, the work presented in this thesis attempts to fill this gap. The dynamic performance of the dc side of VSC-HVDC systems is explored in Chapter 4 through eigenvalue analysis, and a frequency domain approach is proposed in Chapter 5 in order to explain the source of the dc side instability.

Chapter 4

Small signal modelling and analysis of VSC-HVDC system

In the previous chapter, the investigations carried out from different authors on the dynamics of dc network have been reviewed. For instance, instability related to the resonance phenomenon of the dc-side and the operating point of the system has been found in a point-to-point HVDC system in [49]. The same phenomenon has been found through simulations in a two-terminal VSC-HVDC system, whose results have been presented in Section 3.3. In this chapter, the causes of the instability are further investigated through eigenvalue analysis of the system. The investigated system is linearized around an operating point and the obtained state space model is derived following a modular approach, explained in Section 4.1. The modelling approach is not constrained to a two-terminal VSC-HVDC system but can also be used to model more complex HVDC structures, such as VSC-MTDC systems. For the sake of simplicity, the stability analysis is carried out in a two-terminal VSC-HVDC system using eigenvalue analysis. The influence of different factors on the dynamics of the system is studied. Among the studied factors are operating points, controller parameters, electrical characteristic of the dc side of the system, and characteristics of the ac system to which the VSCs are connected.

4.1 Modelling approach

The modelling approach consists of defining subsystems which are interconnected into the final system of interest. The advantage of this approach is that details can be easily added in individual models. Moreover, in a computational program, it is simpler to implement routines to model small subsystems to later be merged into the system of interest, rather than to implement a large system at once. It also allows flexibility, since the subsystems can be modelled individually and then reused in different configurations. Furthermore, the dynamics of the system of interest can be investigated through the analysis of the individual subsystems, as will be shown in Chapter 5. For example, in Figure 4.1, a three-terminal VSC-HVDC is represented as a multivariable feedback system, which can be divided into two subsystems, the VSC-set subsystem (which, assuming a three-terminal HVDC system

is constituted by VSC₁, VSC₂, VSC₃) and the dc grid subsystem. Each subsystem has inputs and outputs which are used as interconnection variables. In this case, the VSC-set subsystem has the references to the control system of the VSCs as the inputs, and the currents that the VSCs inject to the dc side, i_1 , i_2 , and i_3 , as the outputs. Likewise, the dc

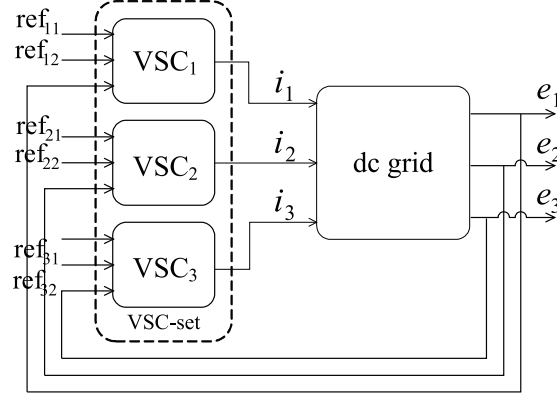


Figure 4.1: Sketch of the modelling approach proposed in this thesis

grid has the currents injected by each VSC, i_1 , i_2 and i_3 , as the inputs, and the voltages of the dc nodes to where the VSCs are connected, e_1 , e_2 and e_3 , as the outputs. The state-space model of the VSC-set subsystem can be represented as

$$\dot{\mathbf{x}}_c = \mathbf{f}_c(\mathbf{x}_c, \mathbf{e}, \mathbf{r}) \quad (4.1a)$$

$$\mathbf{i} = \mathbf{h}_c(\mathbf{x}_c, \mathbf{e}, \mathbf{r}) \quad (4.1b)$$

where

\mathbf{x}_c is the VSC-set state vector,

\mathbf{r} is the VSC-set reference input vector, defined as $[\text{ref}_{11} \text{ref}_{12} \text{ref}_{21} \text{ref}_{22} \text{ref}_{31} \text{ref}_{32}]^T$,

\mathbf{e} is the VSC-set voltage vector, defined as $[e_1 \ e_2 \ e_3]^T$,

\mathbf{i} is the VSC-set current vector, defined as $[i_1 \ i_2 \ i_3]^T$.

The state-space model of the dc grid subsystem is

$$\dot{\mathbf{x}}_g = \mathbf{f}_g(\mathbf{x}_g, \mathbf{i}) \quad (4.2a)$$

$$\mathbf{e} = \mathbf{h}_g(\mathbf{x}_g) \quad (4.2b)$$

where \mathbf{x}_g is the dc grid state vector. The state space model of the VSC-MTDC system can be derived by combining (4.1) and (4.2). That is

$$\dot{\mathbf{x}}_c = \mathbf{f}_c(\mathbf{x}_c, \mathbf{h}_g(\mathbf{x}_g), \mathbf{r}) \quad (4.3a)$$

$$\dot{\mathbf{x}}_g = \mathbf{f}_g(\mathbf{x}_g, \mathbf{h}_c(\mathbf{x}_c, \mathbf{h}_g(\mathbf{x}_g), \mathbf{r})). \quad (4.3b)$$

From (4.3), it can be seen that the HVDC system state space model can be derived using the expressions that define the subsystem models, which is the approach adopted in this chapter.

The small signal analysis is used in this work due to the nonlinear characteristic of the system. Therefore, in order to use the linear analysis tools, the system must be linearized

around a given operating point. It is well known that a nonlinear system

$$\dot{\mathbf{x}} = \mathbf{f}(\mathbf{x}, \mathbf{r}) \quad (4.4)$$

can be linearized as

$$\Delta \dot{\mathbf{x}} = \left[\frac{\partial \mathbf{f}}{\partial \mathbf{x}} \right]_0 \Delta \mathbf{x} + \left[\frac{\partial \mathbf{f}}{\partial \mathbf{r}} \right]_0 \Delta \mathbf{r} \quad (4.5)$$

where

| | |
|---|---|
| $\Delta \mathbf{x}$ | is the deviation of \mathbf{x} from the operating point \mathbf{x}_0 , |
| $\Delta \mathbf{r}$ | is the deviation of \mathbf{r} from the initial reference \mathbf{r}_0 , |
| $\left[\frac{\partial \mathbf{f}}{\partial \mathbf{x}} \right]_0$ and $\left[\frac{\partial \mathbf{f}}{\partial \mathbf{r}} \right]_0$ | are the jacobians of \mathbf{f} with respect to \mathbf{x} and \mathbf{r} , respectively, |
| $\mathbf{x}_0, \mathbf{r}_0$ | evaluated at the initial point $(\mathbf{x}_0, \mathbf{r}_0)$, |
| | are the initial states and the initial references, respectively. |

Equation (4.5) describes the small signal dynamics around the operating point $(\mathbf{x}_0, \mathbf{r}_0)$. This method is used throughout this chapter for the linearization of the nonlinear expressions of the system model.

4.2 Assumptions

The objective of this chapter is to investigate the instability described in Section 3.3. In order to facilitate the analysis, the models should be as simple as possible but still containing a sufficient level of detail to represent the dynamic issues under investigation. The following assumptions are adopted in this thesis in order to simplify the system model.

1. The electrical properties of the capacitors, inductors and resistors are linear. They are also temperature and frequency independent.
2. The measuring devices are ideal. The signals coming from these devices are noise-free, instantaneous with no distortion.
3. The converter is treated as a linear amplifier. That means that the high frequency harmonics originated by the switching actions of the power electronic valves are neglected. Besides, the converter is assumed lossless meaning that the power in the ac side is equal to the power in the dc side of the converter.

In addition to the above assumptions, initially, the VSC models are developed considering that they are connected to infinite ac sources. This allows to neglect PLL block, since the angle it measures becomes constant. Assuming infinite ac sources also reduces the scope of the problem to only the dc side of the system, so if stability problems are found, they are only due to the interaction between the converters and the dc grid. Later, the ac sources are considered non-infinite, and their effects on the stability of the system are studied.

4.3 State space model of a VSC connected to an infinite ac source

The VSC system to be modelled is depicted in Figure 4.2. In the ac side, the converter is modelled as a ideal controllable three-phase voltage source connected to the ac source through the phase reactor. In this section, the ac sources connected to the Point of Common Coupling (PCC), are assumed infinitely strong (See Figure 4.2). This means that the source impedance is zero (i.e. $R_{si} = 0$ and $L_{si} = 0$). In the dc side, the converter is modelled as a current source, where the magnitude of the current is such that the powers in the ac side and the dc side of the converter are equal. The control system is the same as the one described in Section 2.4. The converter capacitor is considered as part of the dc grid, then, it is not modelled as part of the VSC system. Next, the state space model of a VSC system connected to a infinite ac source is derived.

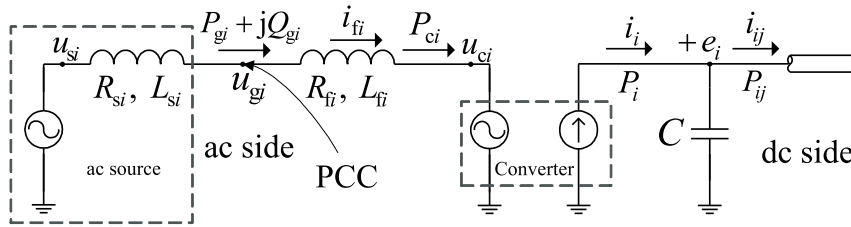


Figure 4.2: Model of the i -th VSC system

4.3.1 VSC open-loop model

From Figure 4.2, the model that describes the current injection of the i -th VSC to the i -th dc node can be expressed in the converter dq frame as

$$\frac{di_{fi}^d}{dt} = -\frac{R_{fi}}{L_{fi}}i_{fi}^d + \omega_{gi}i_{fi}^q + \frac{1}{L_{fi}}u_{gi}^d - \frac{1}{L_{fi}}u_{ci}^d \quad (4.6a)$$

$$\frac{di_{fi}^q}{dt} = -\frac{R_{fi}}{L_{fi}}i_{fi}^q - \omega_{gi}i_{fi}^d + \frac{1}{L_{fi}}u_{gi}^q - \frac{1}{L_{fi}}u_{ci}^q \quad (4.6b)$$

$$i_i = \frac{u_{ci}^d i_{fi}^d + u_{ci}^q i_{fi}^q}{e_i} \quad (4.6c)$$

where the subscript “ i ” denotes that the variable corresponds to the i -th VSC system. The currents i_{fi}^d and i_{fi}^q are the d and q components of the current through the phase reactor, respectively; u_{gi}^d and u_{gi}^q are the d and q components of the ac grid voltage, respectively; u_{ci}^d and u_{ci}^q are the d and q components of the converter voltage, respectively; ω_{gi} is the angular frequency of the ac side of the VSC; i_i is the current injected to the dc side of the VSC; e_i is the voltage of the dc node to which the VSC is connected. Furthermore, R_{fi} and L_{fi} are the resistance and the inductance of the phase reactor.

4.3. State space model of a VSC connected to an infinite ac source

It should be noted that the system (4.6) is nonlinear, since (4.6c) is a nonlinear expression. Equation (4.6) can be linearized as follows

$$\frac{d\Delta i_{fi}^d}{dt} = -\frac{R_{fi}}{L_{fi}}\Delta i_{fi}^d + \omega_{gi0}\Delta i_{fi}^q + i_{fi0}^q\Delta\omega_{gi} + \frac{1}{L_{fi}}\Delta u_{gi}^d - \frac{1}{L_{fi}}\Delta u_{ci}^d \quad (4.7a)$$

$$\frac{d\Delta i_{fi}^q}{dt} = -\omega_{gi0}\Delta i_{fi}^d - \frac{R_{fi}}{L_{fi}}\Delta i_{fi}^q - i_{fi0}^d\Delta\omega_{gi} + \frac{1}{L_{fi}}\Delta u_{gi}^q - \frac{1}{L_{fi}}\Delta u_{ci}^q \quad (4.7b)$$

$$\Delta i_i = \frac{u_{ci0}^d}{e_{i0}}\Delta i_{fi}^d + \frac{u_{ci0}^q}{e_{i0}}\Delta i_{fi}^q + \frac{i_{fi0}^d}{e_{i0}}\Delta u_{ci}^d + \frac{i_{fi0}^q}{e_{i0}}\Delta u_{ci}^q - \frac{P_{i0}}{e_{i0}^2}\Delta e_i \quad (4.7c)$$

where the subscript “0” denotes the initial conditions as

$$P_{i0} = P_{c0} = u_{ci0}^d i_{fi0}^d + u_{ci0}^q i_{fi0}^q. \quad (4.8)$$

When the ac source is assumed infinite, u_{gi}^d , u_{gi}^q and ω_{gi} are constant. In addition, u_{gi}^q is zero since the d axis of the dq frame is aligned to the rotating vector $\underline{u}_{gi}^{\alpha\beta}$. Considering the mentioned items, the following applies

$$u_{gi}^q = 0, \quad \Delta u_{gi}^d = 0, \quad \Delta u_{gi}^q = 0, \quad \Delta\omega_{gi} = 0. \quad (4.9)$$

It should be stressed that (4.9) does not hold when the ac source is not infinitely strong. Next, the closed-loop system models are derived when the VSC is implemented with the VCC and the DVC described in Section 2.4.

4.3.2 VSC closed-loop model with current controller

Considering the controller algorithm described by (2.32), the VCC of the i -th VSC can be expressed as

$$\frac{dm_i^d}{dt} = k_{ii}(i_{fi}^{dref} - i_{fi}^d) \quad (4.10a)$$

$$\frac{dm_i^q}{dt} = k_{ii}(i_{fi}^{qref} - i_{fi}^q) \quad (4.10b)$$

$$u_{ci}^{dref} = u_{gi}^d + \omega_{gi}L_{fi}i_{fi}^q - k_{pi}(i_{fi}^{dref} - i_{fi}^d) - m_i^d \quad (4.10c)$$

$$u_{ci}^{qref} = u_{gi}^q - \omega_{gi}L_{fi}i_{fi}^d - k_{pi}(i_{fi}^{qref} - i_{fi}^q) - m_i^q \quad (4.10d)$$

where m_i^d and m_i^q are states that accounts for the integral action of the controller (2.32). Under the assumptions made, the voltage $\underline{u}_{ci}^{dqref}$ can be considered equal to \underline{u}_{ci}^{dq} . Then, the closed-loop system of the VSC is

$$\frac{d}{dt} \begin{bmatrix} i_{fi}^d \\ i_{fi}^q \end{bmatrix} = \begin{bmatrix} -\alpha_i & 0 \\ 0 & -\alpha_i \end{bmatrix} \begin{bmatrix} i_{fi}^d \\ i_{fi}^q \end{bmatrix} + \begin{bmatrix} \alpha_i & 0 \\ 0 & \alpha_i \end{bmatrix} \begin{bmatrix} i_{fi}^{dref} \\ i_{fi}^{qref} \end{bmatrix} \quad (4.11a)$$

$$i_i = \frac{u_{ci}^d i_{fi}^d + u_{ci}^q i_{fi}^q}{e_i} \quad (4.11b)$$

where k_{pi} and k_{ii} have been selected as $\alpha_i L_{fi}$ and $\alpha_i R_{fi}$. Equation (4.11a) is linear and can be easily expressed in terms of small signals. The linearized expression of (4.11b) becomes (4.7c). Moreover, when the VCC outputs, (4.10c) and (4.10d), are linearized they result in

$$\Delta u_{ci}^d = \Delta u_{gi}^d + k_{pi}\Delta i_{fi}^d + \omega_{gi0}L_{fi}\Delta i_{fi}^q + i_{fi0}^qL_{fi}\Delta\omega_{gi} - \Delta m_i^d - k_{pi}\Delta i_{fi}^{dref} \quad (4.12a)$$

$$\Delta u_{ci}^q = \Delta u_{gi}^q - \omega_{gi0}L_{fi}\Delta i_{fi}^d + k_{pi}\Delta i_{fi}^q - i_{fi0}^dL_{fi}\Delta\omega_{gi} - \Delta m_i^q - k_{pi}\Delta i_{fi}^{qref}. \quad (4.12b)$$

Furthermore, it can be also shown that, for the selected values of k_{pi} and k_{ii} , m_i^d is $R_{fi}i_{fi}^d$ and m_i^q is $R_{fi}i_{fi}^q$. Finally, considering (4.9), and combining (4.12) with (4.7c), the closed-loop system model (VSC and current controller) in terms of small signals is

$$\frac{d\Delta\mathbf{x}_{si}^c}{dt} = \mathbf{A}_{si}^c\Delta\mathbf{x}_{si}^c + \mathbf{B}_{sri}^c\Delta\mathbf{r}_{si}^c + \mathbf{B}_{sei}^c\Delta e_i \quad (4.13a)$$

$$\Delta i_i = \mathbf{C}_{si}^c\Delta\mathbf{x}_{si}^c + \mathbf{D}_{sri}^c\Delta\mathbf{r}_{si}^c + D_{sei}^c\Delta e_i \quad (4.13b)$$

where

$$\Delta\mathbf{x}_{si}^c = \begin{bmatrix} \Delta i_{fi}^d \\ \Delta i_{fi}^q \end{bmatrix}, \quad \Delta\mathbf{r}_{si}^c = \begin{bmatrix} \Delta i_{fi}^{dref} \\ \Delta i_{fi}^{qref} \end{bmatrix}, \quad \mathbf{A}_{si}^c = \begin{bmatrix} -\alpha_i & 0 \\ 0 & -\alpha_i \end{bmatrix}, \quad \mathbf{B}_{sri}^c = \begin{bmatrix} \alpha_i & 0 \\ 0 & \alpha_i \end{bmatrix}, \quad \mathbf{B}_{sei}^c = \begin{bmatrix} 0 \\ 0 \end{bmatrix},$$

$$\mathbf{C}_{si}^c = \begin{bmatrix} \frac{u_{g0}^d - 2R_{fi}i_{fi0}^d + i_{fi0}^d\alpha_i L_{fi}}{e_{i0}} & \frac{-2R_{fi}i_{fi0}^q + i_{fi0}^q\alpha_i L_{fi}}{e_{i0}} \end{bmatrix},$$

$$\mathbf{D}_{sri}^c = \frac{\alpha_i L_{fi}}{e_{i0}} \begin{bmatrix} -i_{fi0}^d & -i_{fi0}^q \end{bmatrix}, \quad D_{sei}^c = -\frac{P_{i0}}{e_{i0}^2}.$$

Interestingly, the system (4.13) can be further reduced to a first order system as

$$\frac{d\Delta z_i}{dt} = -\alpha_i\Delta z_i + \alpha_i \begin{bmatrix} a & b \end{bmatrix} \begin{bmatrix} \Delta i_{fi}^{dref} \\ \Delta i_{fi}^{qref} \end{bmatrix} \quad (4.14a)$$

$$\Delta i_i = \Delta z_i + \frac{\alpha_i L_{fi}}{e_{i0}} \begin{bmatrix} -i_{fi0}^d & -i_{fi0}^q \end{bmatrix} \begin{bmatrix} \Delta i_{fi}^{dref} \\ \Delta i_{fi}^{qref} \end{bmatrix} - \frac{P_{i0}}{e_{i0}^2}\Delta e_i \quad (4.14b)$$

where

$$\Delta z_i = a\Delta i_{fi}^d + b\Delta i_{fi}^q, \quad a = \frac{u_{g0}^d - 2R_{fi} + i_{fi0}^d\alpha_i L_{fi}}{e_{i0}} \quad \text{and} \quad b = \frac{-2R_{fi} + i_{fi0}^q\alpha_i L_{fi}}{e_{i0}}.$$

However, the model (4.14) does not allow the access to variables such us the currents Δi_{fi}^d and Δi_{fi}^q . The model (4.13) is considered in this thesis since it gives access to the ac side variables.

4.3.3 VSC closed loop model with direct voltage controller

The DVC studied in this thesis is the one described by (2.54), and, for the i -th VSC, it can be expressed as

$$\frac{dn_i}{dt} = k_{iei}(e_i^{\text{ref}} - e_i) \quad (4.15a)$$

$$i_{fi}^{dref} = k_{pei}(e_i^{\text{ref}} - e_i) + n_i. \quad (4.15b)$$

where n_i is the state that accounts for the integral actions of the controller. In terms of small signals, (4.15) becomes

$$\frac{d\Delta n_i}{dt} = k_{iei}(\Delta e_i^{\text{ref}} - \Delta e_i) \quad (4.16a)$$

$$\Delta i_{fi}^{dref} = k_{pei}(\Delta e_i^{\text{ref}} - \Delta e_i) + \Delta n_i \quad (4.16b)$$

4.4. State space model of a VSC connected to a non-infinite ac source

whose output is the current reference Δi_{fi}^{dref} which is one of the inputs of the system (4.13). Combining (4.13) and (4.16), the state space model of closed-loop system is

$$\frac{d\Delta \mathbf{x}_{si}^e}{dt} = \mathbf{A}_{si}^e \Delta \mathbf{x}_{si}^e + \mathbf{B}_{sri}^e \Delta \mathbf{r}_{si}^e + \mathbf{B}_{sei}^e \Delta e_i \quad (4.17a)$$

$$\Delta i_i = \mathbf{C}_{si}^e \Delta \mathbf{x}_{si}^e + \mathbf{D}_{sri}^e \Delta \mathbf{r}_{si}^e + \mathbf{D}_{sei}^e \Delta e_i \quad (4.17b)$$

where

$$\Delta \mathbf{x}_{si}^e = \begin{bmatrix} \Delta i_{fi}^d \\ \Delta i_{fi}^q \\ \Delta n_i \end{bmatrix}, \quad \Delta \mathbf{r}_{si}^e = \begin{bmatrix} \Delta e_i^{ref} \\ \Delta i_{fi}^{qref} \end{bmatrix}, \quad \mathbf{A}_{si}^e = \begin{bmatrix} -\alpha_i & 0 & \alpha_i \\ 0 & -\alpha_i & 0 \\ 0 & 0 & 0 \end{bmatrix}, \quad \mathbf{B}_{sri}^e = \begin{bmatrix} \alpha_i k_{pei} & 0 \\ 0 & \alpha_i \\ k_{iei} & 0 \end{bmatrix},$$

$$\mathbf{B}_{sei}^e = \begin{bmatrix} -\alpha_i k_{pe} \\ 0 \\ -k_{iei} \end{bmatrix}, \quad \mathbf{C}_{si}^e = \begin{bmatrix} \frac{u_{g0}^d - 2R_{fi}i_{fi0}^d + i_{fi0}^d \alpha_i L_{fi}}{e_{i0}} & \frac{-2R_{fi}i_{fi0}^q + i_{fi0}^q \alpha_i L_{fi}}{e_{i0}} & -\frac{\alpha_i L_{fi} i_{fi0}^d}{e_{i0}} \end{bmatrix},$$

$$\mathbf{D}_{sri}^e = \frac{\alpha_i L_{fi}}{e_{i0}} \begin{bmatrix} -k_{pei} i_{fi0}^d & -i_{fi0}^q \end{bmatrix}, \quad \mathbf{D}_{sei}^e = \begin{pmatrix} \frac{\alpha_i L_{fi} k_{pei} i_{fi0}^d}{e_{i0}} & -\frac{P_{i0}}{e_{i0}^2} \end{pmatrix}.$$

As mentioned in Section 2.4.4, the active power is controlled directly through the current reference Δi_{fi}^{dref} . Then, if a VSC connected to a strong ac grid is set to control the active power, its state space model is given by (4.13), while if it is set to control the direct-voltage, its state space model is given by (4.17).

4.4 State space model of a VSC connected to a non-infinite ac source

Models for VSCs connected to non-infinite ac sources are derived in this section since it is desired to investigate the impact of weak ac sources on the dc network dynamics of the VSC-HDVC system. Two ac side configurations are considered in this section. In the first configuration, the VSC is connected to a non-infinite ac source with no voltage support. In the second configuration, apart from considering a non-infinite ac source, a shunt ac capacitor is connected at the PCC. Next, the representation of vectors with constant rotating speed in the converter dq is presented.

4.4.1 Constant frequency vectors in the converter dq frame

It must be borne in mind that the converter dq frame uses the angle estimated by the PLL to perform the transformation from the stationary $\alpha\beta$ frame to the rotating dq frame. That means that, in transient conditions, a vector with a constant rotating speed and magnitude will not be necessarily constant in the converter dq frame when considering a non-infinite ac source. Similarly to [44], a *grid dq frame* can be defined. In order to perform the transformation, the grid dq frame uses the synchronous angle, θ_{gi}^s , which changes at a constant rate ω_{gi0} , and initially coincides with the converter dq frame (see Figure 4.3).

After a disturbance, the grid dq frame and the converter dq frame do not coincide anymore, and they can be represented as shown in Figure 4.3 where the voltage u_{gi} is plotted¹.

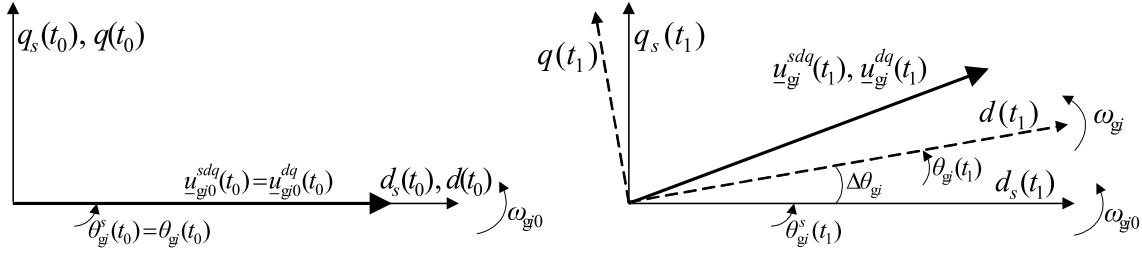


Figure 4.3: Left: u_{gi} represented in the grid and the converter dq at initial conditions ($t = t_0$). Right: u_{gi} represented in the grid and the converter dq frame after a disturbance ($t = t_1$).

From Figure 4.3, both rotating frames, when transformed to the $\alpha\beta$ frame, should give the same vector, that is

$$\underline{u}_{gi}^{sdq} e^{j\theta_{gi}^s} = \underline{u}_{gi}^{dq} e^{j\theta_{gi}} = \underline{u}_{gi}^{\alpha\beta} \quad (4.18)$$

or in general, any vector z in the converter dq frame is related to the grid dq frame as

$$\underline{z}^{dq} = \underline{z}^{sdq} e^{-j\Delta\theta_{gi}} \quad (4.19)$$

where $\Delta\theta_{gi} = \theta_{gi} - \theta_{gi}^s$. In terms of small signal deviations, (4.19) becomes

$$\Delta \underline{z}^{dq} = \Delta \underline{z}^{sdq} - j \underline{z}_0^{sdq} \Delta\theta_{gi} \quad (4.20)$$

In particular, vectors which have a constant frequency, phase and magnitude, have constant components in the grid dq frame. For example, the ac source voltage, \underline{u}_{si}^{sdq} , indicated in Figure 4.2, is constant since u_{si} is a three-phase voltage with constant frequency, phase and magnitude. This also implies that $\Delta \underline{u}_{si}^{sdq}$ is zero. Then, $\Delta \underline{u}_{si}^{sdq}$ expressed in the converter dq frame is

$$\Delta \underline{u}_{si}^{dq} = -j \underline{u}_{si0}^{sdq} \Delta\theta_{gi} \quad (4.21)$$

or, more explicitly

$$\Delta u_{si}^d = u_{si0}^{sq} \Delta\theta_{gi} \quad (4.22a)$$

$$\Delta u_{si}^q = -u_{si0}^{sd} \Delta\theta_{gi} \quad (4.22b)$$

where u_{si0}^{sd} and u_{si0}^{sq} are the initial operating voltages.

4.4.2 VSC closed-loop model - no ac filter capacitor at the PCC

The VSC model with the current controller is described by (4.11). However, different from the case when the ac grid is assumed infinite, the voltage deviation $\Delta \underline{u}_{gi}^{dq}$ is not zero in the

¹Note that variables in the grid dq frame have the superscript “s”

4.4. State space model of a VSC connected to a non-infinite ac source

linearized expression (4.12). Then, in terms of small signals, the current injected by the VSC to the dc side, Δi_i , is:

$$\begin{aligned} \Delta i_i = & \left[\begin{array}{cc} \frac{u_{gi0}^d - 2R_{fi}i_{fi0}^d + \alpha_i L_{fi}i_{fi0}^d}{e_{i0}} & \frac{-2R_{fi}i_{fi0}^q + \alpha_i L_{fi}i_{fi0}^q}{e_{i0}} \end{array} \right] \left[\begin{array}{c} \Delta i_{fi}^d \\ \Delta i_{fi}^q \end{array} \right] \\ & + \left[\begin{array}{cc} -\frac{\alpha_i L_{fi}i_{fi0}^d}{e_{i0}} & -\frac{\alpha_i L_{fi}i_{fi0}^q}{e_{i0}} \end{array} \right] \left[\begin{array}{c} \Delta i_{fi}^{dref} \\ \Delta i_{fi}^{qref} \end{array} \right] - \frac{P_{i0}}{e_{i0}^2} \Delta e_i \\ & + \left[\begin{array}{cc} i_{fi0}^d & i_{fi0}^q \\ e_{i0} & e_{i0} \end{array} \right] \left[\begin{array}{c} \Delta u_{gi}^d \\ \Delta u_{gi}^q \end{array} \right] \end{aligned} \quad (4.23)$$

where it can be seen that the only difference between (4.13b) and (4.23) are the additional terms related to the voltage $\Delta \underline{u}_{gi}^{dq}$. However, Δu_{gi}^d and Δu_{gi}^q are not actually inputs nor states of the closed-loop VSC system. Then, they have to be expressed in terms of the states and inputs of the system. The voltage $\Delta \underline{u}_{gi}^{dq}$ can be expressed as

$$\Delta \underline{u}_{gi}^{dq} = \left(\frac{L_{fi}}{L_{si} + L_{fi}} \right) \Delta \underline{u}_{si}^{dq} + \left(\frac{L_{si}}{L_{si} + L_{fi}} \right) \Delta \underline{u}_{ci}^{dq} + \left(\frac{R_{fi}L_{si} - R_{si}L_{fi}}{L_{si} + L_{fi}} \right) \Delta i_{fi}^{dq}. \quad (4.24)$$

Using (4.12) and (4.24), it can be shown that, in terms of small signals, the voltage $\Delta \underline{u}_{gi}^{dq}$ becomes

$$\begin{aligned} \Delta u_{gi}^d = & \Delta u_{si}^d - R_{si} \Delta i_{fi}^d + i_{fi0}^q L_{si} \Delta \omega_{gi} + \omega_{gi0} L_{si} \Delta i_{fi}^q + \alpha_i L_{si} \Delta i_{fi}^d \\ & - \alpha_i L_{si} \Delta i_{fi}^{dref} \end{aligned} \quad (4.25a)$$

$$\begin{aligned} \Delta u_{gi}^q = & \Delta u_{si}^q - R_{si} \Delta i_{fi}^q - i_{fi0}^d L_{si} \Delta \omega_{gi} - \omega_{gi0} L_{si} \Delta i_{fi}^d + \alpha_i L_{si} \Delta i_{fi}^q \\ & - \alpha_i L_{si} \Delta i_{fi}^{qref} \end{aligned} \quad (4.25b)$$

where the term $\Delta \omega_{gi}$ denotes the frequency deviation. Regarding the angular frequency and the angles, from Figure 4.3, it can be claimed that

$$\Delta \theta_{gi} = \theta_{gi} - \theta_{gi}^s, \quad \Delta \omega_{gi} = \omega_{gi} - \omega_{gi0}, \quad \frac{d\omega_{gi0}}{dt} = 0, \quad \frac{d\theta_{gi}^s}{dt} = \omega_{gi0}. \quad (4.26)$$

Using (4.26), the PLL described in Section 2.4.2 can be written in terms of small signals as

$$\frac{d\Delta n_{\omega i}}{dt} = k_{ili} \Delta u_{gi}^q \quad (4.27a)$$

$$\frac{d\Delta \theta_{gi}}{dt} = \Delta n_{\omega i} + k_{pli} \Delta u_{gi}^q. \quad (4.27b)$$

Equation (4.22) can be entered into (4.25) and using (4.11), (4.23) and (4.27) the state space model of the closed-loop VSC system, analogously to (4.13), is in this case

$$\frac{d\Delta \mathbf{x}_{si}^c}{dt} = \mathbf{A}_{si}^c \Delta \mathbf{x}_{si}^c + \mathbf{B}_{sri}^c \Delta \mathbf{r}_{si}^c + \mathbf{B}_{sei}^c \Delta e_i \quad (4.28a)$$

$$\Delta i_i = \mathbf{C}_{si}^c \Delta \mathbf{x}_{si}^c + \mathbf{D}_{sri}^c \Delta \mathbf{r}_{si}^c + \mathbf{D}_{sei}^c \Delta e_i \quad (4.28b)$$

where

$$\begin{aligned} \Delta \mathbf{x}_{si}^c &= [\Delta i_{fi}^d \quad \Delta i_{fi}^q \quad \Delta n_{\omega i} \quad \Delta \theta_{gi}]^T, \quad \Delta \mathbf{r}_{si}^c = [\Delta i_{fi}^{dref} \quad \Delta i_{fi}^{qref}]^T, \\ \mathbf{A}_{si}^c &= \begin{bmatrix} -\alpha_i & 0 & 0 & 0 \\ 0 & -\alpha_i & 0 & 0 \\ -k_{ili}L_{si}\omega_{gi0}d & k_{ili}(\alpha_i L_{si} - R_{si})d & -k_{ili}L_{si}i_{fi0}^d d & -k_{ili}u_{si0}^d d \\ -k_{pli}L_{si}\omega_{gi0}d & k_{pli}(\alpha_i L_{si} - R_{si})d & d & -k_{pli}u_{si0}^d d \end{bmatrix} \\ \mathbf{B}_{sri}^c &= \begin{bmatrix} \alpha_i & 0 & 0 & 0 \\ 0 & \alpha_i & -\alpha_i L_{si}k_{ili}d & -\alpha_i L_{si}k_{pli}d \end{bmatrix}^T, \quad \mathbf{B}_{sri}^c = \mathbf{0}_{4 \times 1} \\ \mathbf{C}_{si}^c &= \begin{bmatrix} \frac{u_{si0}^d - 2R_{ti}i_{fi0}^d + \alpha_i L_{ti}i_{fi0}^d}{e_{i0}} & \frac{u_{si0}^q - 2R_{ti}i_{fi0}^q + \alpha_i L_{ti}i_{fi0}^q}{e_{i0}} & 0 & \frac{i_{fi0}^d u_{si0}^q - i_{fi0}^q u_{si0}^d}{e_{i0}} \end{bmatrix}, \\ \mathbf{D}_{sri}^c &= \begin{bmatrix} -\frac{\alpha_i L_{ti}i_{fi0}^d}{e_{i0}} & -\frac{\alpha_i L_{ti}i_{fi0}^q}{e_{i0}} \end{bmatrix}, \quad D_{sei}^c = -\frac{P_{i0}}{e_{i0}^2}, \quad d = \frac{1}{1 + i_{fi0}L_{si}k_{pli}} \end{aligned}$$

where $L_{ti} = L_{fi} + L_{si}$ and $R_{ti} = R_{fi} + R_{si}$. Considering (4.16) into (4.28), the closed-loop system of the VSC and the DVC is given by

$$\frac{d\Delta \mathbf{x}_{si}^e}{dt} = \mathbf{A}_{si}^e \Delta \mathbf{x}_{si}^e + \mathbf{B}_{sri}^e \Delta \mathbf{r}_{si}^e + \mathbf{B}_{sei}^e \Delta e_i \quad (4.29a)$$

$$\Delta i_i = \mathbf{C}_{si}^e \Delta \mathbf{x}_{si}^e + \mathbf{D}_{sri}^e \Delta \mathbf{r}_{si}^e + D_{sei}^e \Delta e_i \quad (4.29b)$$

where

$$\begin{aligned} \Delta \mathbf{x}_{si}^e &= [\Delta i_{fi}^d \quad \Delta i_{fi}^q \quad \Delta n_{\omega i} \quad \Delta \theta_{gi} \quad \Delta n_i]^T, \quad \Delta \mathbf{r}_{si}^e = [\Delta e_i^{ref} \quad \Delta i_{fi}^{qref}]^T \\ \mathbf{A}_{si}^e &= \begin{bmatrix} -\alpha_i & 0 & 0 & 0 & \alpha_i \\ 0 & -\alpha_i & 0 & 0 & 0 \\ -k_{ili}L_{si}\omega_{gi0}d & k_{ili}d(\alpha_i L_{si} - R_{si}) & -k_{ili}L_{si}i_{fi0}^d d & -k_{ili}u_{si0}^d d & 0 \\ -k_{pli}L_{si}\omega_{gi0}d & k_{pli}d(\alpha_i L_{si} - R_{si}) & d & -k_{pli}u_{si0}^d d & 0 \\ 0 & 0 & 0 & 0 & 0 \end{bmatrix} \\ \mathbf{B}_{sri}^e &= \begin{bmatrix} \alpha_i k_{pei} & 0 & 0 & 0 & k_{iei} \\ 0 & \alpha_i & -\alpha_i L_{si}k_{ili}d & -\alpha_i L_{si}k_{pli}d & 0 \end{bmatrix}^T, \\ \mathbf{B}_{sei}^e &= [-\alpha_i k_{pei} \quad 0 \quad 0 \quad 0 \quad -k_{iei}]^T \\ \mathbf{C}_{si}^e &= \begin{bmatrix} \frac{u_{si0}^d - 2R_{ti}i_{fi0}^d + \alpha_i L_{ti}i_{fi0}^d}{e_{i0}} & \frac{u_{si0}^q - 2R_{ti}i_{fi0}^q + \alpha_i L_{ti}i_{fi0}^q}{e_{i0}} & 0 & \frac{i_{fi0}^d u_{si0}^q - i_{fi0}^q u_{si0}^d}{e_{i0}} & -\frac{\alpha_i L_{ti}i_{fi0}^d}{e_{i0}} \end{bmatrix} \\ \mathbf{D}_{sri}^e &= \begin{bmatrix} -\frac{\alpha_i L_{ti}k_{pei}i_{fi0}^d}{e_{i0}} & -\frac{\alpha_i L_{ti}i_{fi0}^q}{e_{i0}} \end{bmatrix}, \quad D_{sei}^e = \left(\frac{\alpha_i L_{ti}k_{pei}i_{fi0}^d}{e_{i0}} - \frac{P_{i0}}{e_{i0}^2} \right). \end{aligned}$$

4.4.3 VSC closed-loop model - ac filter capacitor at the PCC

An ac filter capacitor is connected at the PCC, as shown in Figure 4.4. In this case, the dynamics of the voltage at the ac side capacitor, \underline{u}_{gi}^{dq} , and the current through the source impedance, \underline{i}_{si}^{dq} , must be considered together with (4.11).

4.4. State space model of a VSC connected to a non-infinite ac source

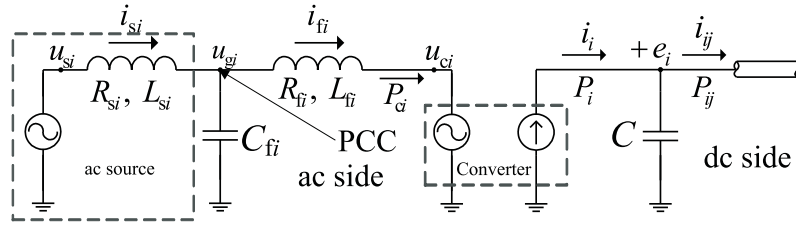


Figure 4.4: VSC system model with an ac capacitor

The dynamics of the current i_{si}^{dq} is

$$\frac{di_{si}^d}{dt} = -\frac{R_{si}}{L_{si}}i_{si}^d + \omega_{gi}i_{si}^q + \frac{1}{L_{si}}u_{si}^d - \frac{1}{L_{si}}u_{gi}^d \quad (4.30a)$$

$$\frac{di_{si}^q}{dt} = -\frac{R_{si}}{L_{si}}i_{si}^q - \omega_{gi}i_{si}^d + \frac{1}{L_{si}}u_{si}^q - \frac{1}{L_{si}}u_{gi}^q \quad (4.30b)$$

while the dynamics of the voltage u_{gi}^{dq} is given by

$$\frac{du_{gi}^d}{dt} = -\frac{1}{C_{fi}}i_{fi}^d + \frac{1}{C_{fi}}i_{si}^d + \omega_{gi}u_{gi}^q \quad (4.31a)$$

$$\frac{du_{gi}^q}{dt} = -\frac{1}{C_{fi}}i_{fi}^q + \frac{1}{C_{fi}}i_{si}^q - \omega_{gi}u_{gi}^d. \quad (4.31b)$$

Considering (4.22), in terms of small signals, (4.31) and (4.30) become

$$\frac{d\Delta i_{si}^d}{dt} = -\frac{R_{si}}{L_{si}}\Delta i_{si}^d + \omega_{gi0}\Delta i_{si}^q + i_{si0}^q\Delta\omega_{gi} + \frac{u_{si0}^q}{L_{si}}\Delta\theta_{gi} - \frac{1}{L_{si}}\Delta u_{gi}^d \quad (4.32a)$$

$$\frac{d\Delta i_{si}^q}{dt} = -\frac{R_{si}}{L_{si}}\Delta i_{si}^q - \omega_{gi0}\Delta i_{si}^d - i_{si0}^d\Delta\omega_{gi} - \frac{u_{si0}^d}{L_{si}}\Delta\theta_{gi} - \frac{1}{L_{si}}\Delta u_{gi}^q \quad (4.32b)$$

$$\frac{d\Delta u_{gi}^d}{dt} = -\frac{1}{C_{fi}}\Delta i_{fi}^d + \frac{1}{C_{fi}}\Delta i_{si}^d + u_{gi0}^q\Delta\omega_{gi} + \omega_{gi0}\Delta u_{gi}^q \quad (4.32c)$$

$$\frac{d\Delta u_{gi}^q}{dt} = -\frac{1}{C_{fi}}\Delta i_{fi}^q + \frac{1}{C_{fi}}\Delta i_{si}^q - u_{gi0}^d\Delta\omega_{gi} - \omega_{gi0}\Delta u_{gi}^d. \quad (4.32d)$$

Therefore, the state space model of the closed-loop VSC system is

$$\frac{d\Delta \mathbf{x}_{si}^c}{dt} = \mathbf{A}_{si}^c \Delta \mathbf{x}_{si}^c + \mathbf{B}_{sri}^c \Delta \mathbf{r}_{si}^c + \mathbf{B}_{sei}^c \Delta e_i \quad (4.33a)$$

$$\Delta i_i = \mathbf{C}_{si}^c \Delta \mathbf{x}_{si}^c + \mathbf{D}_{sri}^c \Delta \mathbf{r}_{si}^c + D_{sei}^c \Delta e_i \quad (4.33b)$$

where

$$\Delta \mathbf{x}_{si}^c = [\Delta i_{fi}^d \quad \Delta i_{fi}^q \quad \Delta i_{si}^d \quad \Delta i_{si}^q \quad \Delta u_{gi}^d \quad \Delta u_{gi}^q \quad \Delta n_{\omega i} \quad \Delta \theta_{gi}]^T, \quad \Delta \mathbf{r}_{si}^c = \begin{bmatrix} \Delta i_{fi}^{dref} \\ \Delta i_{fi}^{qref} \end{bmatrix}$$

$$\mathbf{A}_{si}^c = \begin{bmatrix} -\alpha_i & 0 & 0 & 0 & 0 & 0 & 0 & 0 & 0 \\ 0 & -\alpha_i & 0 & 0 & 0 & 0 & 0 & 0 & 0 \\ 0 & 0 & -\frac{R_{si}}{L_{si}} & \omega_{gi0} & -\frac{1}{L_{si}} & i_{si0}^q k_{pli} & i_{si0}^q & \frac{u_{si0}^q}{L_{si}} & 0 \\ 0 & 0 & -\omega_{gi0} & -\frac{R_{si}}{L_{si}} & 0 & -\frac{1}{L_{si}} - i_{si0}^d k_{pli} & -i_{si0}^d & -\frac{u_{si0}^d}{L_{si}} & 0 \\ -\frac{1}{C_{si}} & 0 & \frac{1}{C_{si}} & 0 & 0 & \omega_{gi0} & u_{gi0}^q & 0 & 0 \\ 0 & -\frac{1}{C_{si}} & 0 & \frac{1}{C_{si}} & -\omega_{gi0} & -u_{gi0}^d k_{pli} & -u_{gi0}^d & 0 & 0 \\ 0 & 0 & 0 & 0 & 0 & k_{ili} & 0 & 0 & 0 \\ 0 & 0 & 0 & 0 & 0 & k_{pli} & 1 & 0 & 0 \end{bmatrix},$$

$$\mathbf{B}_{sri}^c = \begin{bmatrix} \alpha_i & 0 & 0 & 0 & 0 & 0 & 0 & 0 & 0 \\ 0 & \alpha_i & 0 & 0 & 0 & 0 & 0 & 0 & 0 \end{bmatrix}^T, \quad \mathbf{B}_{sei}^c = \mathbf{0}_{8 \times 1},$$

$$\mathbf{C}_{si}^c = \begin{bmatrix} \frac{u_{gi0}^d - 2R_{fi}i_{fi0}^d + \alpha_i L_{fi}i_{fi0}^d}{e_{i0}} & \frac{u_{gi0}^q - 2R_{fi}i_{fi0}^q + \alpha_i L_{fi}i_{fi0}^q}{e_{i0}} & 0 & 0 & \frac{i_{fi0}^d}{e_{i0}} & \frac{i_{fi0}^q}{e_{i0}} & 0 & 0 \end{bmatrix}$$

$$\mathbf{D}_{sri}^c = \begin{bmatrix} -\frac{\alpha_i L_{fi}i_{fi0}^d}{e_{i0}} & -\frac{\alpha_i L_{fi}i_{fi0}^q}{e_{i0}} \end{bmatrix}, \quad D_{sei}^c = -\frac{P_{i0}}{e_{i0}^2}.$$

Similarly to Section 4.4.2, the closed-loop system of the VSC and the DVC (4.16) is as follows

$$\frac{d\Delta \mathbf{x}_{si}^e}{dt} = \mathbf{A}_{si}^e \Delta \mathbf{x}_{si}^e + \mathbf{B}_{sri}^e \Delta \mathbf{r}_{si}^e + \mathbf{B}_{sei}^e \Delta e_i \quad (4.34a)$$

$$\Delta i_i = \mathbf{C}_{si}^e \Delta \mathbf{x}_{si}^e + \mathbf{D}_{sri}^e \Delta \mathbf{r}_{si}^e + D_{sei}^e \Delta e_i \quad (4.34b)$$

where

$$\Delta \mathbf{x}_{si}^e = [\Delta i_{fi}^d \quad \Delta i_{fi}^q \quad \Delta i_{si}^d \quad \Delta i_{si}^q \quad \Delta u_{gi}^d \quad \Delta u_{gi}^q \quad \Delta n_{\omega i} \quad \Delta \theta_{gi} \quad \Delta n_i]^T, \quad \Delta \mathbf{r}_{si}^e = \begin{bmatrix} \Delta e_i^{\text{ref}} \\ \Delta i_{fi}^{\text{qref}} \end{bmatrix}$$

$$\mathbf{A}_{si}^e = \begin{bmatrix} -\alpha_i & 0 & 0 & 0 & 0 & 0 & 0 & 0 & \alpha_i \\ 0 & -\alpha_i & 0 & 0 & 0 & 0 & 0 & 0 & 0 \\ 0 & 0 & -\frac{R_{si}}{L_{si}} & \omega_{gi0} & -\frac{1}{L_{si}} & i_{si0}^q k_{pli} & i_{si0}^q & \frac{u_{si0}^q}{L_{si}} & 0 \\ 0 & 0 & -\omega_{gi0} & -\frac{R_{si}}{L_{si}} & 0 & -\frac{1}{L_{si}} - i_{si0}^d k_{pli} & -i_{si0}^d & -\frac{u_{si0}^d}{L_{si}} & 0 \\ -\frac{1}{C_{si}} & 0 & \frac{1}{C_{si}} & 0 & 0 & \omega_{gi0} & u_{gi0}^q & 0 & 0 \\ 0 & -\frac{1}{C_{si}} & 0 & \frac{1}{C_{si}} & -\omega_{gi0} & -u_{gi0}^d k_{pli} & -u_{gi0}^d & 0 & 0 \\ 0 & 0 & 0 & 0 & 0 & k_{ili} & 0 & 0 & 0 \\ 0 & 0 & 0 & 0 & 0 & k_{pli} & 1 & 0 & 0 \\ 0 & 0 & 0 & 0 & 0 & 0 & 0 & 0 & 0 \end{bmatrix}$$

$$\mathbf{B}_{sri}^e = \begin{bmatrix} \alpha_i k_{pei} & 0 & 0 & 0 & 0 & 0 & 0 & 0 & k_{iei} \\ 0 & \alpha_i & 0 & 0 & 0 & 0 & 0 & 0 & 0 \end{bmatrix}^T$$

$$\mathbf{B}_{sei}^e = \begin{bmatrix} -\alpha_i k_{pei} & 0 & 0 & 0 & 0 & 0 & 0 & 0 & -k_{iei} \end{bmatrix}^T$$

$$\mathbf{C}_{si}^e = \begin{bmatrix} \frac{u_{gi0}^d - 2R_{fi}i_{fi0}^d + \alpha_i L_{fi}i_{fi0}^d}{e_{i0}} & \frac{u_{gi0}^q - 2R_{fi}i_{fi0}^q + \alpha_i L_{fi}i_{fi0}^q}{e_{i0}} & 0 & 0 & \frac{i_{fi0}^d}{e_{i0}} & \frac{i_{fi0}^q}{e_{i0}} & 0 & 0 & -\frac{\alpha_i L_{fi}i_{fi0}^d}{e_{i0}} \end{bmatrix}$$

$$\mathbf{D}_{sri}^e = \begin{bmatrix} -\frac{\alpha_i L_{fi}k_{pei}i_{fi0}^d}{e_{i0}} & -\frac{\alpha_i L_{fi}i_{fi0}^q}{e_{i0}} \end{bmatrix}, \quad D_{sei}^e = \left(\frac{\alpha_i L_{fi}k_{pei}i_{fi0}^d}{e_{i0}} - \frac{P_{i0}}{e_{i0}^2} \right).$$

Finally, the selection of the VSC model depends on the configuration of the ac side. To summarize:

VSC connected to an infinite ac source: The model (4.13) is used if the VSC is set to control the active power injection to the dc side. The model (4.17) is used if the VSC is set to control the direct-voltage.

VSC connected to a non-infinite ac source, without ac side capacitor: The model (4.28) is used if the VSC is set to control the active power injection to the dc side. The model (4.29) is used if the VSC is set to control the direct-voltage.

VSC connected to a non-infinite ac source, with ac side capacitor: The model (4.33) is used if the VSC is set to control the active power injection to the dc side. The model (4.34) is used if the VSC is set to control the direct-voltage.

4.5 DC grid state space model

The state space model of a generic dc grid with n nodes, m branches and where p VSCs are connected, will be derived in this section. In this thesis, cables or overhead transmission lines are both modelled as Π -sections. As an example, Figure 4.5 shows a dc cable represented as a Π -section connected between the dc nodes j and k . The nodes are electrical points where branches and shunt elements (such as the equivalent capacitors C_{bj} and C_{bk} connected to the nodes j and k , respectively) are connected. A node is characterized by its voltage. For example, in the figure, e_j and e_k are the voltages of the nodes j and k , respectively. The series elements which interconnect the nodes are called branches. For instance, in the figure it is shown the branch bi (which is composed by a series connection of the resistance R_{bi} and the inductance L_{bi}) which interconnects the nodes j and k . The branches are characterized by the current which flows *from* one node *to* the other corresponding node. In the figure, the currents i_j and i_k represent current injections from external sources, such as converters.

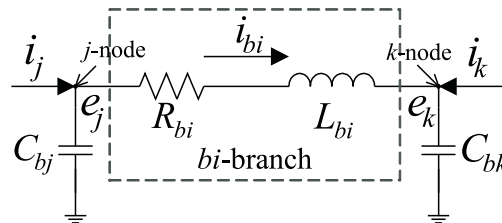


Figure 4.5: A cable connected between the nodes j and k modelled as a π section

From Figure 4.5, the dynamics of the voltages e_j and e_k , and the current i_{bi} , are given by

the following equation

$$C_{bj} \frac{de_j}{dt} = -i_{bi} + i_j \quad (4.35a)$$

$$C_{bk} \frac{de_k}{dt} = i_{bi} + i_k \quad (4.35b)$$

$$L_{bi} \frac{di_{bi}}{dt} = -R_{bi}i_{bi} + e_j - e_k \quad (4.35c)$$

which can be generalized as

$$\mathbf{C} \frac{d\mathbf{e}}{dt} = -\mathbf{T}^T \mathbf{i}_b + \mathbf{Q} \mathbf{i} \quad (4.36a)$$

$$\mathbf{L} \frac{d\mathbf{i}_b}{dt} = -\mathbf{R} \mathbf{i}_b + \mathbf{T} \mathbf{e} \quad (4.36b)$$

where \mathbf{e} is the vector of voltages of the n dc node defined as

$$\Delta \mathbf{e} = [e_1 \quad e_2 \quad \dots \quad e_n]^T \quad (4.37)$$

\mathbf{i}_b is vector of currents through the m branches, defined as

$$\Delta \mathbf{i}_b = [i_{b1}, i_{b2} \quad \dots \quad i_{bm}] \quad (4.38)$$

\mathbf{i} is the vector of currents injected by the p VSCs connected to the dc grid, defined as

$$\Delta \mathbf{i} = [i_1, i_2 \quad \dots \quad i_p]. \quad (4.39)$$

\mathbf{C} is the capacitance matrix and the following rules define its jk -th element

$$c_{jk} = \begin{cases} 0 & \text{if } j \neq k \\ C_{eqj} & \text{if } j = k \end{cases} \quad (4.40)$$

In this case, the indices j and k are related to the dc node number, and their maximum values are n . C_{eqj} is the equivalent capacitor connected to the dc node j . The equivalent capacitor is given by

$$C_{eqj} = C_{bj1} + C_{bj2} + \dots + C_{bjh} + C_{jvsc} \quad (4.41)$$

where the subscript h represents the number of cables connected to the dc node j and C_{jvsc} is the VSC capacitor connected to the node j , if any is connected to it. Then, the matrix \mathbf{C} is a diagonal matrix whose size is $n \times n$. \mathbf{L} is the inductance matrix and its jk -th element is defined as follows

$$l_{jk} = \begin{cases} 0 & \text{if } j \neq k \\ L_{bj} & \text{if } j = k \end{cases} \quad (4.42)$$

In this case, the indices j and k are related to the branch number, and their maximum values are m . L_{bj} is the equivalent inductor of the branch bj , which comes from the Π -model of the cable. Then, the matrix \mathbf{L} is a diagonal matrix whose size is $m \times m$. Finally, the jk -th element of the resistance matrix \mathbf{R} is defined as:

$$r_{jk} = \begin{cases} 0 & \text{if } j \neq k \\ R_{bj} & \text{if } j = k \end{cases} \quad (4.43)$$

In this case, the indices j and k are related to the branch number, and their maximum values are m . R_{bj} is the equivalent resistor of the branch bj , which comes from the Π -model of the cable. Then, the matrix \mathbf{R} is a diagonal matrix whose size is $m \times m$.

\mathbf{T} is the so-called incidence matrix [53], which gives information about the interconnection of the different branches and nodes. The information needed to build matrix \mathbf{T} is “from” which node “to” which node the branch current flows. Then, the jk -th element of the matrix \mathbf{T} is defined as follow:

$$t_{jk} = \begin{cases} +1 & \text{if } k \text{ corresponds to the “from” bus of the branch } j \\ -1 & \text{if } k \text{ corresponds to the “to” bus of the branch } j \\ 0 & \text{if } k \text{ does not correspond to any of the buses} \\ & \text{to where the branch } j \text{ is connected} \end{cases} \quad (4.44)$$

In this case, the index j is related to the branch number and its maximum value is m . The index k is related to the dc node number, and its maximum value is n . Then, the size of the matrix \mathbf{T} is $m \times n$.

\mathbf{Q} is called the current injection matrix in this thesis, since it gives information on to which nodes the VSCs inject current. The following defines the jk -th element of \mathbf{Q}

$$q_{jk} = \begin{cases} 0 & \text{if the VSC } k \text{ is not connected to the node } j \\ 1 & \text{if the VSC } k \text{ is connected to the node } j \end{cases} \quad (4.45)$$

where q_{jk} is the jk -element of the matrix \mathbf{Q} . In this case, the index j is related to the dc node number and its maximum value is n , while the index k is related to the VSC “identification” number and its maximum value is p . Then, the matrix \mathbf{Q} is a diagonal matrix whose size is $n \times p$.

As a result, the state space model of the dc grid is given by

$$\frac{d\mathbf{x}_g}{dt} = \mathbf{A}_g \mathbf{x}_g + \mathbf{B}_g \mathbf{i}_g \quad (4.46a)$$

$$\mathbf{e} = \mathbf{C}_g \mathbf{x}_g \quad (4.46b)$$

which is a linear system. Equation (4.46), in terms of small signals, is

$$\frac{d\Delta\mathbf{x}_g}{dt} = \mathbf{A}_g \Delta\mathbf{x}_g + \mathbf{B}_g \Delta\mathbf{i} \quad (4.47a)$$

$$\Delta\mathbf{e} = \mathbf{C}_g \Delta\mathbf{x}_g \quad (4.47b)$$

where

$$\Delta\mathbf{x}_g = \begin{bmatrix} \Delta\mathbf{e} \\ \Delta\mathbf{i}_b \end{bmatrix}, \quad \mathbf{A}_g = \begin{bmatrix} \mathbf{0}_{n \times n} & -\mathbf{C}^{-1} \mathbf{T}^T \\ \mathbf{L}^{-1} \mathbf{T} & \mathbf{L}^{-1} \mathbf{R} \end{bmatrix}, \quad \mathbf{B}_g = \begin{bmatrix} \mathbf{C}^{-1} \mathbf{Q} \\ \mathbf{0}_{m \times p} \end{bmatrix}, \quad \mathbf{C}_g = [\mathbf{I}_{n \times n} \quad \mathbf{0}_{n \times m}]$$

4.6 HVDC system state space model

In order to show the generality of the modelling procedure, the state space model of a three-terminal HVDC system, such as the one shown in Figure 2.23 and Figure 4.1, is

developed in this section as a example. Let us assume that the VSC₁ is set to control the direct-voltage, and the VSC₂ and VSC₃ are set to control the power. The state space models of VSC₁, VSC₂ and VSC₃ are:

VSC₁

$$\frac{d\Delta\mathbf{x}_{s1}^e}{dt} = \mathbf{A}_{s1}^e \Delta\mathbf{x}_{s1}^e + \mathbf{B}_{sr1}^e \Delta\mathbf{r}_{s1}^e + \mathbf{B}_{se1}^e \Delta e_1 \quad (4.48a)$$

$$\Delta i_1 = \mathbf{C}_{s1}^e \Delta\mathbf{x}_{s1}^e + \mathbf{D}_{sr1}^e \Delta\mathbf{r}_{s1}^e + D_{se1}^e \Delta e_1 \quad (4.48b)$$

VSC₂

$$\frac{d\Delta\mathbf{x}_{s2}^c}{dt} = \mathbf{A}_{s2}^c \Delta\mathbf{x}_{s2}^c + \mathbf{B}_{sr2}^c \Delta\mathbf{r}_{s2}^c + \mathbf{B}_{se2}^c \Delta e_2 \quad (4.49a)$$

$$\Delta i_2 = \mathbf{C}_{s2}^c \Delta\mathbf{x}_{s2}^c + \mathbf{D}_{sr2}^c \Delta\mathbf{r}_{s2}^c + D_{se2}^c \Delta e_2 \quad (4.49b)$$

VSC₃

$$\frac{d\Delta\mathbf{x}_{s3}^c}{dt} = \mathbf{A}_{s3}^c \Delta\mathbf{x}_{s3}^c + \mathbf{B}_{sr3}^c \Delta\mathbf{r}_{s3}^c + \mathbf{B}_{se3}^c \Delta e_3 \quad (4.50a)$$

$$\Delta i_3 = \mathbf{C}_{s3}^c \Delta\mathbf{x}_{s3}^c + \mathbf{D}_{sr3}^c \Delta\mathbf{r}_{s3}^c + D_{se3}^c \Delta e_3 \quad (4.50b)$$

Then, the state space model of the VSC-set subsystem (as defined in Figure 4.1), where the inputs are the references $\Delta\mathbf{r}_{s1}^e$, $\Delta\mathbf{r}_{s2}^c$ and $\Delta\mathbf{r}_{s3}^c$ and the outputs are i_1 , i_2 and i_3 , is

$$\frac{d\Delta\mathbf{x}_{vsc}}{dt} = \mathbf{A}_{vsc} \Delta\mathbf{x}_{vsc} + \mathbf{B}_{vsc}^r \Delta\mathbf{r}_{vsc} + \mathbf{B}_{vsc}^e \Delta\mathbf{e} \quad (4.51a)$$

$$\Delta\mathbf{i} = \mathbf{C}_{vsc} \Delta\mathbf{x}_{vsc} + \mathbf{D}_{vsc}^r \Delta\mathbf{r}_{vsc} + \mathbf{D}_{vsc}^e \Delta\mathbf{e} \quad (4.51b)$$

where

$$\Delta\mathbf{x}_{vsc} = \begin{bmatrix} \Delta\mathbf{x}_{s1}^e \\ \Delta\mathbf{x}_{s2}^c \\ \Delta\mathbf{x}_{s3}^c \end{bmatrix}, \quad \mathbf{A}_{vsc} = \begin{bmatrix} \mathbf{A}_{s1}^e & \mathbf{0} & \mathbf{0} \\ \mathbf{0} & \mathbf{A}_{s2}^c & \mathbf{0} \\ \mathbf{0} & \mathbf{0} & \mathbf{A}_{s3}^c \end{bmatrix}, \quad \mathbf{B}_{vsc}^r = \begin{bmatrix} \mathbf{B}_{sr1}^e & \mathbf{0} & \mathbf{0} \\ \mathbf{0} & \mathbf{B}_{sr2}^c & \mathbf{0} \\ \mathbf{0} & \mathbf{0} & \mathbf{B}_{sr3}^c \end{bmatrix},$$

$$\Delta\mathbf{r}_{vsc} = \begin{bmatrix} \Delta\mathbf{r}_{s1}^e \\ \Delta\mathbf{r}_{s2}^c \\ \Delta\mathbf{r}_{s3}^c \end{bmatrix}, \quad \mathbf{B}_{vsc}^e = \begin{bmatrix} \mathbf{B}_{se1}^e & \mathbf{0} & \mathbf{0} \\ \mathbf{0} & \mathbf{B}_{se2}^c & \mathbf{0} \\ \mathbf{0} & \mathbf{0} & \mathbf{B}_{se3}^c \end{bmatrix}, \quad \mathbf{C}_{vsc} = \begin{bmatrix} \mathbf{C}_{s1}^e & \mathbf{0} & \mathbf{0} \\ \mathbf{0} & \mathbf{C}_{s2}^c & \mathbf{0} \\ \mathbf{0} & \mathbf{0} & \mathbf{C}_{s3}^c \end{bmatrix},$$

$$\mathbf{D}_{vsc}^r = \begin{bmatrix} \mathbf{D}_{sr1}^e & \mathbf{0} & \mathbf{0} \\ \mathbf{0} & \mathbf{D}_{sr2}^c & \mathbf{0} \\ \mathbf{0} & \mathbf{0} & \mathbf{D}_{sr3}^c \end{bmatrix}, \quad \mathbf{D}_{vsc}^e = \begin{bmatrix} D_{se1}^e & 0 & 0 \\ 0 & D_{se2}^c & 0 \\ 0 & 0 & D_{se3}^c \end{bmatrix}$$

In order to obtain the state space model of the MTDC system, (4.47) can be combined with (4.51). The following is the state space model of a three-terminal VSC-HVDC system

$$\frac{d\Delta\mathbf{x}_{sys}}{dt} = \mathbf{A}_{sys} \Delta\mathbf{x}_{sys} + \mathbf{B}_{sys} \Delta\mathbf{r}_{sys} \quad (4.52a)$$

$$\Delta\mathbf{y}_{sys} = \mathbf{C}_{sys} \Delta\mathbf{x}_{sys} \quad (4.52b)$$

where

$$\Delta\mathbf{x}_{sys} = \begin{bmatrix} \Delta\mathbf{x}_{vsc} \\ \Delta\mathbf{x}_g \end{bmatrix}, \quad \mathbf{A}_{sys} = \begin{bmatrix} \mathbf{A}_{vsc} & \mathbf{B}_{vsc}^e \mathbf{C}_g \\ \mathbf{B}_g \mathbf{C}_{vsc} & \mathbf{A}_g + \mathbf{B}_g \mathbf{D}_{vsc}^e \mathbf{C}_g \end{bmatrix}$$

$$\Delta\mathbf{r}_{sys} = \Delta\mathbf{r}_{vsc}, \quad \mathbf{B}_{sys} = \begin{bmatrix} \mathbf{B}_{vsc}^r \\ \mathbf{B}_g \mathbf{D}_{vsc}^r \end{bmatrix}$$

the VCC of both VSCs, $\alpha_{1,2}$, are selected as 4 pu (1256.6 rad/s), as suggested in [44]. Finally, the DVC parameters of VSC₁ are varied in the different tests performed, and they are specified at the beginning of every test.

Table 4.1: Converter data

| Electrical parameter | Value |
|---|-----------|
| Phase reactor inductance (L_{f1}, L_{f2}) | 0.25 pu |
| Phase reactor resistance (R_{f1}, R_{f1}) | 0.0025 pu |
| Capacitor per pole (C_1, C_2) | 3.142 pu |
| VCC bandwidth (α_1, α_2) | 4.0 pu |
| VCC proportional gain (k_{p1}, k_{p2}) | 1.0 pu |
| VCC integral gain (k_{i1}, k_{i2}) | 0.01 pu |

Table 4.2: CL₁₂ Cable Data in pu

| Electrical parameter | Value |
|--------------------------------|-----------------------------|
| Cable capacitance (C_{b1}) | 0.0195 pu/km |
| Cable inductance (L_{b1}) | $1.975 \cdot 10^{-4}$ pu/km |
| Cable resistance (R_{b1}) | $1.253 \cdot 10^{-4}$ pu/km |

4.7.2 VSCs connected to infinite ac sources

Similar to Section 3.3, the VSCs of the two-terminal HVDC system are assumed to be connected to infinite ac sources in this section. Two cases are studied, and they are differentiated by the choice of the DVC parameters k_{pe1} and k_{ie1} . The choice k_{pe1} and k_{ie1} is shown in Table 4.3. In both cases, the cable length is assumed as 50 km.

Table 4.3: DVC parameters of VSC₁

| Parameter | Case 1 (pu) | Case 2 (pu) |
|---------------|-------------|-------------|
| ω_{n1} | 0.40 | 0.80 |
| ξ_1 | 3.0 | 3.0 |
| k_{pe1} | 4.62 | 9.23 |
| k_{ie1} | 0.31 | 1.23 |

It should be highlighted that the choice of k_{pe1} and k_{ie1} are higher than the values recommended in [44], which, adapted to (2.48), means that ξ_1 should be equal to 1 and ω_{n1} should be less than $0.1\alpha_1$. However, high values are chosen for the sake of illustration. Besides, it should be borne in mind that the ac source to which VSC₁ is connected is assumed infinite which makes the system quite robust.

The VSC-set subsystem is modelled as indicated in Section 4.3, meaning that VSC₁ is modelled as (4.17) and VSC₂ as (4.13). The dc grid subsystem is modelled following

the procedure indicated in Section 4.5. Finally, the system state space model is obtained according to the procedure indicated in Section 4.6. The power transfer between VSC₁ and VSC₂ is regulated with the current reference i_{f2}^{dref} . In this section, the current references, i_{f1}^{qref} and i_{f2}^{qref} are set to zero. The direct-voltage reference, e_1^{ref} is set to 1.

Table 4.4 shows the eigenvalues for i_{f2}^{dref} equal to +1 pu, 0 and -1 pu. The table shows that, in case 1, the system is stable for the three values of i_{f2}^{dref} since the real parts of all eigenvalues are negative. The eigenvalues $\lambda_{1,2}$ are complex conjugate which means that they are oscillatory modes. Moreover, the real parts of $\lambda_{1,2}$ are very small compared to the imaginary parts meaning that they are not well damped oscillation modes. Another interesting observation is that the real part of $\lambda_{1,2}$ increases as i_{f2}^{dref} decreases. In case 2, $\lambda_{1,2}$ are not-well-damped oscillatory modes again. However, the main difference from case 1 is that, for i_{f2}^{dref} equal to -1, the real parts of $\lambda_{1,2}$ are positive, which means that the system is unstable. The eigenvalues $\lambda_{3,4}$ changes also with the operating point, but their real parts are negative in all the cases. Finally, $\lambda_{5,6,7,8}$ are negative real numbers and they do not change when the initial operating point is changed.

Table 4.4: Eigenvalues for different i_{f2}^{dref} and DVC parameters

| Set-points | Eigenvalues case 1 (pu) | Eigenvalues case 2 (pu) |
|----------------------|-----------------------------------|-----------------------------------|
| $i_{f2}^{dref} = +1$ | $\lambda_{1,2} = -0.59 \pm j7.00$ | $\lambda_{1,2} = -0.87 \pm j6.96$ |
| | $\lambda_3 = -3.99$ | $\lambda_3 = -3.97$ |
| | $\lambda_4 = -0.49$ | $\lambda_4 = -0.98$ |
| | $\lambda_5 = -0.08$ | $\lambda_5 = -0.15$ |
| | $\lambda_6 = -4.00$ | $\lambda_6 = -4.00$ |
| | $\lambda_7 = -4.00$ | $\lambda_7 = -4.00$ |
| | $\lambda_8 = -4.00$ | $\lambda_8 = -4.00$ |
| $i_{f2}^{dref} = 0$ | $\lambda_{1,2} = -0.38 \pm j7.13$ | $\lambda_{1,2} = -0.44 \pm j7.27$ |
| | $\lambda_3 = -3.22$ | $\lambda_{3,4} = -1.80 \pm j0.61$ |
| | $\lambda_4 = -0.58$ | |
| | $\lambda_5 = -0.08$ | $\lambda_5 = -0.15$ |
| | $\lambda_6 = -4.00$ | $\lambda_6 = -4.00$ |
| | $\lambda_7 = -4.00$ | $\lambda_7 = -4.00$ |
| | $\lambda_8 = -4.00$ | $\lambda_8 = -4.00$ |
| $i_{f2}^{dref} = -1$ | $\lambda_{1,2} = -0.13 \pm j7.25$ | $\lambda_{1,2} = 0.12 \pm j7.49$ |
| | $\lambda_3 = -2.41$ | $\lambda_{3,4} = -1.21 \pm j1.37$ |
| | $\lambda_4 = -0.74$ | |
| | $\lambda_5 = -0.08$ | $\lambda_5 = -0.15$ |
| | $\lambda_6 = -4.00$ | $\lambda_6 = -4.00$ |
| | $\lambda_7 = -4.00$ | $\lambda_7 = -4.00$ |
| | $\lambda_8 = -4.00$ | $\lambda_8 = -4.00$ |

Table 4.5 and Table 4.6 show the absolute values of the participation factors for case 1 when $i_{f2}^{dref} = +1$ and when $i_{f2}^{dref} = -1$, respectively. From the participation factors the following can be claimed:

1. The eigenvalues $\lambda_{1,2}$ are related to the states Δe_1 , Δe_2 and Δi_{b1} which indicates that

$\lambda_{1,2}$ are related to the resonance phenomenon of the dc side.

2. The eigenvalue λ_3 is related to Δi_{f1}^d , which reflects the VCC dynamics. However, in Table 4.6 it can be seen that λ_3 is related to Δi_{f1}^d , Δe_1 Δe_2 , which reflects a possible interaction between the VCC and the DVC.
3. The eigenvalue λ_4 is related to Δe_1 and Δe_2 , which means that it is related to the DVC dynamics. However, Table 4.6 shows that λ_4 also influences Δi_{f1}^d reflecting a possible interaction between the VCC and the DVC.
4. The eigenvalue λ_5 is related the integral part of the DVC, Δn_1 .
5. The eigenvalues $\lambda_{6,7,8}$ are related to the states Δi_{f1}^q , Δi_{f2}^d and Δi_{f2}^q meaning that they relate to the VCC of VSC₁ and VSC₂.

Table 4.5: Absolute values of the participation factors for case 1 and $i_{f2}^{dref} = 1$

| | λ_1 | λ_2 | λ_3 | λ_4 | λ_5 | λ_6 | λ_7 | λ_8 |
|-------------------|-------------|-------------|-------------|-------------|-------------|-------------|-------------|-------------|
| Δi_{f1}^d | 0.0006 | 0.0006 | 1.0078 | 0.0085 | 0.0001 | 0 | 0 | 0 |
| Δi_{f1}^q | 0 | 0 | 0 | 0 | 0 | 1 | 0 | 0 |
| Δn_1 | 0.0015 | 0.0015 | 0.0004 | 0.192 | 1.1886 | 0 | 0 | 0 |
| Δi_{f2}^d | 0 | 0 | 0 | 0 | 0 | 0 | 1 | 0 |
| Δi_{f2}^q | 0 | 0 | 0 | 0 | 0 | 0 | 0 | 1 |
| Δe_1 | 0.2542 | 0.2542 | 0.0069 | 0.6134 | 0.0945 | 0 | 0 | 0 |
| Δe_2 | 0.2542 | 0.2542 | 0.003 | 0.6006 | 0.0942 | 0 | 0 | 0 |
| Δi_{b1} | 0.5062 | 0.5062 | 0.0017 | 0.0135 | 0 | 0 | 0 | 0 |

Table 4.6: Absolute values of the participation factors for case 1 and $i_{f2}^{dref} = -1$

| | λ_1 | λ_2 | λ_3 | λ_4 | λ_5 | λ_6 | λ_7 | λ_8 |
|-------------------|-------------|-------------|-------------|-------------|-------------|-------------|-------------|-------------|
| Δi_{f1}^d | 0.0386 | 0.0386 | 1.7282 | 0.7864 | 0.0072 | 0 | 0 | 0 |
| Δi_{f1}^q | 0 | 0 | 0 | 0 | 0 | 1 | 0 | 0 |
| Δn_1 | 0.0004 | 0.0004 | 0.0261 | 0.2003 | 1.1748 | 0 | 0 | 0 |
| Δi_{f2}^d | 0 | 0 | 0 | 0 | 0 | 0 | 1 | 0 |
| Δi_{f2}^q | 0 | 0 | 0 | 0 | 0 | 0 | 0 | 1 |
| Δe_1 | 0.2894 | 0.2894 | 0.5021 | 1.0181 | 0.0905 | 0 | 0 | 0 |
| Δe_2 | 0.2186 | 0.2186 | 0.3535 | 1.009 | 0.0919 | 0 | 0 | 0 |
| Δi_{b1} | 0.4697 | 0.4697 | 0.1013 | 0.0403 | 0.0004 | 0 | 0 | 0 |

Impact of the operating point

Figure 4.7 shows the pole placement when the current reference i_{f2}^{dref} decreases from +1 pu (indicated with the triangle) to -1 pu (indicated with the circle), decreased in steps of -0.1 pu. Figure 4.7(a) shows that, in case 1, the eigenvalues $\lambda_{1,2}$ approach the unstable region¹

¹The unstable region is defined as the part of the s-plane where the real part of the complex numbers are all positive, i.e. from Figure 4.7, the unstable region is to the right side of the dashed gray line.

of the s-plane as i_{f2}^{dref} decreases. Figure 4.7(b) shows that, in case 2, the system becomes unstable when i_{f2}^{dref} is less than -0.8 pu for this case. Actually, calculations show that when i_{f2}^{dref} is equal to -0.81 , $\lambda_{1,2}$ are $0.0014 \pm j7.46$ which are an unstable eigenvalues. The other eigenvalues, however, remain inside the well damped area defined by the dotted gray lines.

The show the effects of removing the dc-side resonance, the dc cable is modelled as only a resistance of 0.01 pu. Although not realistic, for a two-terminal HVDC system, this configuration might well represent a back-to-back VSC-HVDC system. The eigenvalues of the system are calculated again for case 1 and 2. The eigenvalues when i_{f2}^{dref} is changed from $+1$ to -1 , in steps of -0.1 are plotted in Figure 4.8. It can be seen that similar eigenvalues as $\lambda_{1,2}$ are not found in Figure 4.8 since the dc-side resonance is removed. The other eigenvalues are well damp, meaning that the bandwidth of the DVC can be high without jeopardizing the dynamics of the system. This also means that, modelling the dc cable as only a resistance can give optimistic values for the DVC gains [51]. Then, for the dynamic of the dc network, the dc cables must be modelled in detail.

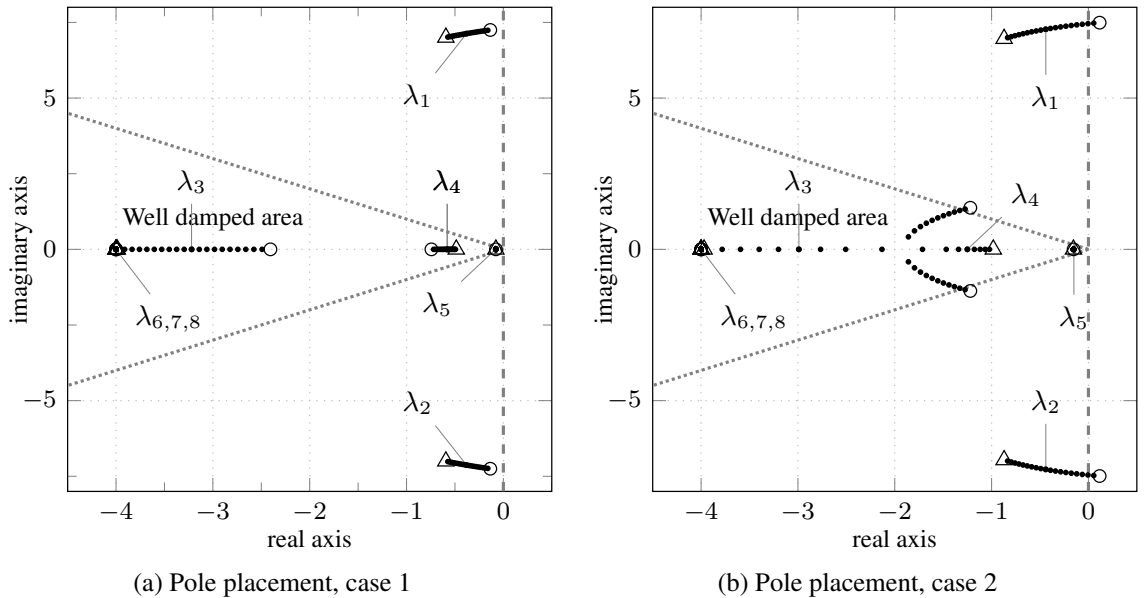


Figure 4.7: Eigenvalues of the system for i_{f2}^{dref} from $+1$ (\triangle) to -1 (\circ), in steps of -0.1 . The cable length is 50 km

According to results shown in Table 4.4, 4.5, 4.6 and Figures 4.7 and 4.8, the following can be concluded:

1. The stability of the system depends on the power transfer, the DVC parameters, and the dynamic characteristic of the dc side of the system. In the analyzed cases, the system becomes unstable when the current reference i_{f2}^{dref} is less than -0.8 pu, and when the DVC gains are high.
2. In the analyzed cases, it has been found that the instability is related to the resonance phenomenon of the dc side of the system. In fact, when the dc side resonance is removed (by modelling the as a resistance), all the eigenvalues are well damped in all the cases.

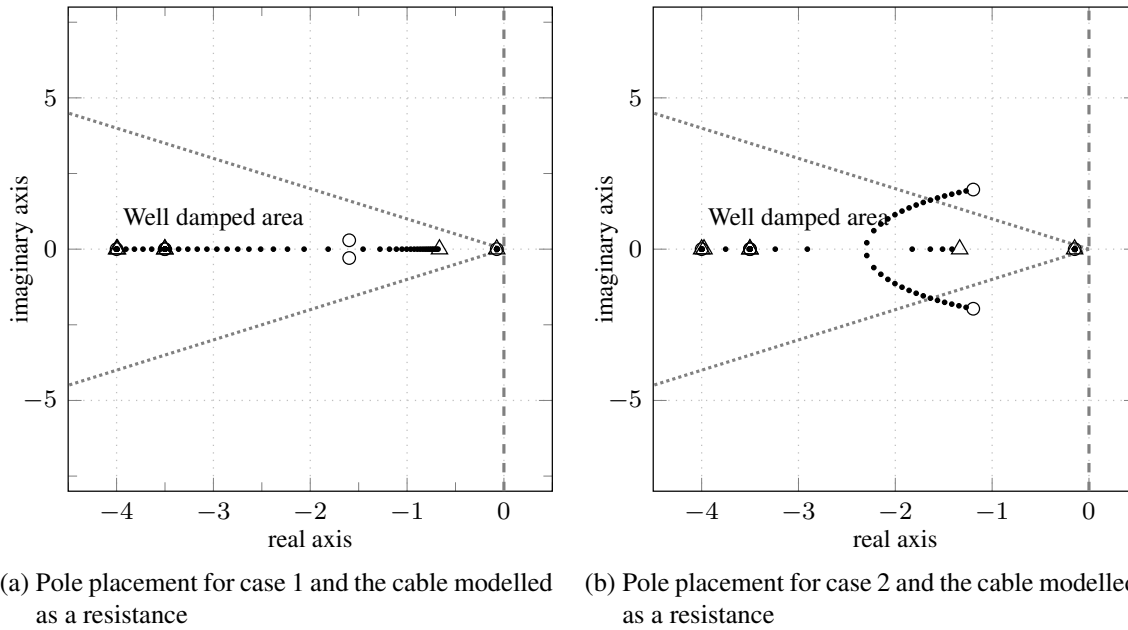


Figure 4.8: Eigenvalues of the system for i_{f2}^{dref} from +1 (\triangle) to -1 (\circ), in steps of -0.1 . The cable is modelled as only a resistance.

Eigenvalue analysis also confirms the results from the simulations shown in Section 3.3. In that case, instability occurred when the power transfer from VSC₁ to VSC₂ is ramped up to 600 MW (corresponding to $i_{f2}^{dref} = -1$ pu). It has been shown in this section that the eigenvalues $\lambda_{1,2}$ approach to the unstable region when the i_{f2}^{dref} gets around -1 pu. In addition, the oscillation frequency in the unstable case is found to be around 350 Hz in Section 3.3. For i_{f2}^{dref} equal to -0.81 pu, the eigenvalues $\lambda_{1,2}$ are $0.0014 \pm j7.46$, which correspond to an oscillation frequency of $7.46 \times 50 = 373$ Hz. This value is in the order of the oscillation frequency found in Section 3.3.

When the power transfer from VSC₂ to VSC₁ is ramped up to 600 MW (corresponding to $i_{f2}^{dref} = 1$ pu), the system is shown to be stable in Section 3.3. From the analysis, it is shown that $\lambda_{1,2}$ move away from the unstable region when i_{f2}^{dref} is increased to $+1$ pu. This means that the real values of $\lambda_{1,2}$ become more negative and the oscillation gets better damped.

Impact of the cable length and the DVC integral gain

In Section 3.3, the impact of the cable length has been also investigated through simulations. It has been shown that the system remains stable in all the analyzed cases when the cable length is 100 km. In this section, the impact of the cable length on the system dynamics is investigated through eigenvalue analysis. Figure 4.9(a) shows the pole placement when the i_{f2}^{dref} is -1 pu, i_{f1}^{qref} and i_{f2}^{qref} are zero, e_1^{ref} is 1 pu, the DVC gains are set according to case 2, and the length is changed from 50 km to 150 km in steps of 5 km. It can be seen from the figure that the real part of $\lambda_{1,2}$ ¹ decreases and become negative as the length in-

¹In this section, from now on, $\lambda_{1,2}$ represents the eigenvalues that are related to the resonance phenomenon of the dc side.

creases which means that the oscillations are more damped. The imaginary part of $\lambda_{1,2}$ also decreases meaning that the oscillation frequency decreases. This means that, the longer the transmission line, the lower the resonance frequency of the dc side of the system.

Figure 4.9(b) shows the pole placement when i_{f2}^{dref} is set to -1 pu, i_{f1}^{qref} and i_{f2}^{qref} are zero, e_1^{ref} is 1 pu, k_{pe1} is 9.23 pu, and the integral term of the DVC, k_{ie1} , is changed from 0 to 12.31 pu. It can be seen that the variation of k_{ie1} has negligible effects on $\lambda_{1,2}$. However, it has a considerable impact on the eigenvalues related to the DVC, which move towards the unstable region (although they still remain inside the stable region). If the eigenvalues of interest are $\lambda_{1,2}$, k_{ie1} can be neglected since it does not have a significant impact on these poles. This implies that the DVC can be implemented as only a proportional controller. That is

$$\Delta i_{f1}^{dref} = k_{pe1}(e_1^{ref} - e_1) \quad (4.53)$$

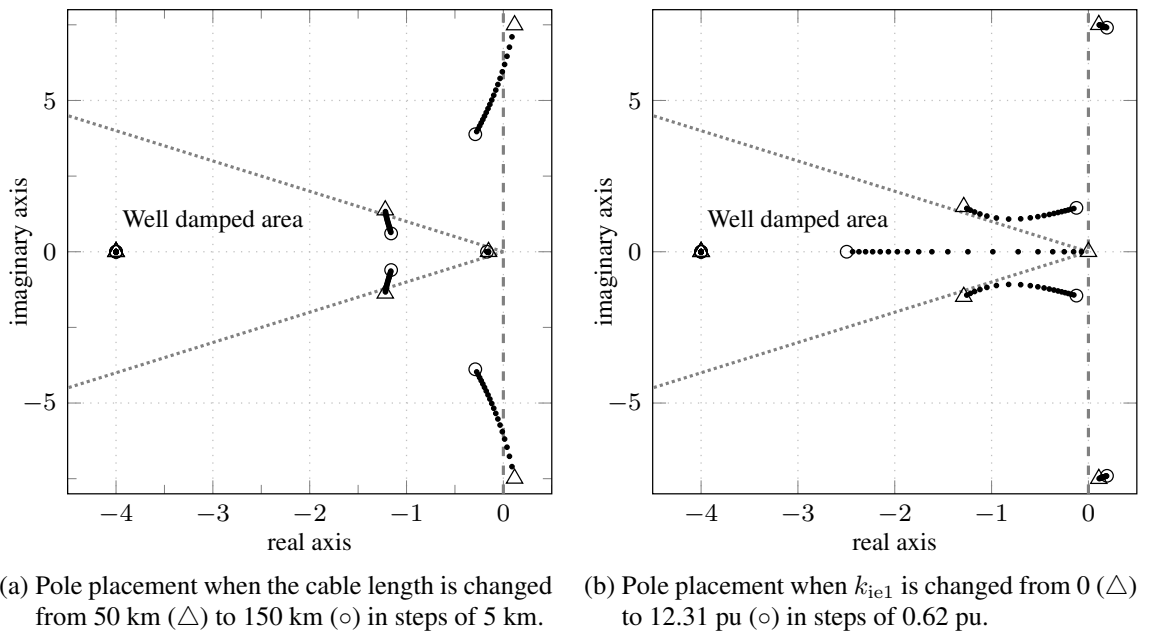


Figure 4.9: Eigenvalues of the system with $i_{f2}^{dref} = -1$

Impact of the current controller bandwidth

Another test performed is the increase of the VCC bandwidth of the VSC which controls the active power, VSC₂. In Table 4.7, the eigenvalues of the system are shown when the VCC bandwidth of VSC₂, α_2 , takes three values, 4, 40 and 400 pu. The other controller parameters are set as defined for case 2, i.e. $\alpha_1 = 4$ pu, $k_{pe1} = 9.23$ pu and $k_{ie1} = 1.23$ pu. The eigenvalues are obtained for two different values of i_{f2}^{dref} , $+1$ and -1 pu.

The results in Table 4.7 show that the speed of response of VSC₂ has no effect on the eigenvalues of the system, except on those that correspond to the dynamics of the VCC of VSC₂, i.e. $\lambda_{7,8}$. If the speed of response of the VCC is assumed to be very high, the currents i_{f2}^d and i_{f2}^q can be assumed constant; and, therefore, having the voltage source u_{s1}

Table 4.7: Eigenvalues for different i_{f2}^{dref} and VSC₂'s VCC bandwidth

| Set-points | $i_{f2}^{dref} = +1$ | $i_{f2}^{dref} = -1$ |
|------------------|-----------------------------------|-----------------------------------|
| $\alpha_2 = 4$ | $\lambda_{1,2} = -0.87 \pm j6.96$ | $\lambda_{1,2} = 0.12 \pm j7.49$ |
| | $\lambda_3 = -3.97$ | $\lambda_{3,4} = -1.22 \pm j1.37$ |
| | $\lambda_4 = -0.98$ | |
| | $\lambda_5 = -0.15$ | $\lambda_5 = -0.15$ |
| | $\lambda_6 = -4.00$ | $\lambda_6 = -4.00$ |
| | $\lambda_7 = -4.00$ | $\lambda_7 = -4.00$ |
| | $\lambda_8 = -4.00$ | $\lambda_8 = -4.00$ |
| $\alpha_2 = 40$ | $\lambda_{1,2} = -0.87 \pm j6.96$ | $\lambda_{1,2} = 0.12 \pm j7.49$ |
| | $\lambda_3 = -3.97$ | $\lambda_{3,4} = -1.22 \pm j1.37$ |
| | $\lambda_4 = -0.98$ | |
| | $\lambda_5 = -0.15$ | $\lambda_5 = -0.15$ |
| | $\lambda_6 = -4.00$ | $\lambda_6 = -4.00$ |
| | $\lambda_7 = -40.00$ | $\lambda_7 = -40.00$ |
| | $\lambda_8 = -40.00$ | $\lambda_8 = -40.00$ |
| $\alpha_2 = 400$ | $\lambda_{1,2} = -0.87 \pm j6.96$ | $\lambda_{1,2} = 0.12 \pm j7.49$ |
| | $\lambda_3 = -3.97$ | $\lambda_{3,4} = -1.22 \pm j1.37$ |
| | $\lambda_4 = -0.98$ | |
| | $\lambda_5 = -0.15$ | $\lambda_5 = -0.15$ |
| | $\lambda_6 = -4.00$ | $\lambda_6 = -4.00$ |
| | $\lambda_7 = -400.00$ | $\lambda_7 = -400.00$ |
| | $\lambda_8 = -400.00$ | $\lambda_8 = -400.00$ |

constant, the active power injection or absorption to the dc side can also be considered constant. That means that the i -th VSC which controls the active power can be modelled as a constant power device without affecting the other eigenvalues of the system. Then, the current injected by the i -th VSC to its dc side can be modelled as

$$\Delta i_i = -\frac{P_{i0}}{e_{i0}^2} \Delta e_i \quad (4.54)$$

which means that a VSC which controls the power can be modelled as a resistance whose sign depends on the direction of the power, and whose value depends on the power and voltage values. If the VSC is injecting power into the dc side, the resistance is negative. If the VSC is absorbing power from the dc side, the resistance is positive.

The impact of the bandwidth of the current controller of VSC₁ is also investigated. One of the main assumptions for arriving to the formula for the parameters of the DVC (2.48) is that the VCC is assumed very fast compared to the DVC. According to the recommendations in [44], for a VCC bandwidth of 4 pu, k_{pe1} and k_{ie1} should be not higher than 1.54 pu and 0.31 pu, respectively, which considers the assumption that the bandwidth of the DVC should be ten times smaller than the VCC. However, the values analyzed and shown in Table 4.3 are relatively high and make the speed of the DVC comparable to the speed of the VCC. Then, if higher values of k_{pe1} and k_{ie1} are desired, the bandwidth of the VCC, α_1 should also be increased. Figure 4.10 shows the eigenvalues when α_1 is varied from 4 to 24 pu in steps of 1 pu. It can be seen that when α_1 is between 4 and 7 pu, the real part of

$\lambda_{1,2}$ increases. When α_1 is greater than 7 and less than 14 pu, the real parts of $\lambda_{1,2}$ starts decreasing but they are still positive. Finally, when α_1 is greater than 14 pu, the real parts of $\lambda_{1,2}$ becomes more negative, therefore, better damped.

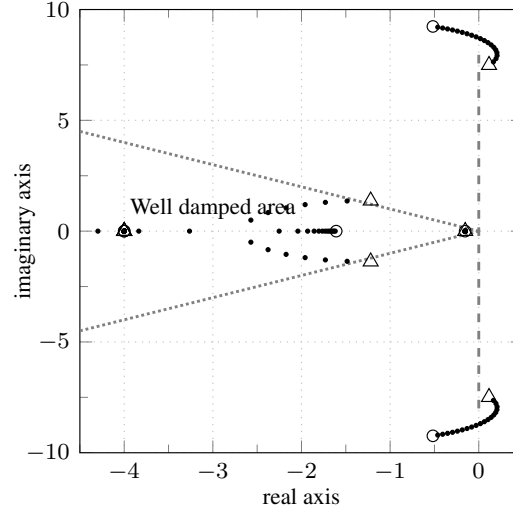


Figure 4.10: Eigenvalues for case 2, $i_{f2}^{dref} = -1$, cable of 50 km, and a change of α_1 from 4 to 24 in steps of 1

4.7.3 VSCs connected to non-infinite ac sources

The same two-terminal VSC HVDC system studied previously is analyzed in this section, but considering that the VSCs are connected to non-infinite ac sources. The VSC controller parameters are as specified in Tables 4.3 and 4.4. The strength of ac system is characterized through the *Short-Circuit Ratio* (SCR). The SCR is defined in [55] as the ratio between the short-circuit power of the ac system to which the converter (either VSC or thyristor-based converter) is connected, and the rated power of the VSC. That is

$$SCR = \frac{S_{sc}}{S_{rated}} \quad (4.55)$$

where S_{sc} is the short-circuit MVA of the ac system, and S_{rated} is the converter MVA rating. Let us start the analysis with a SCR of 5, which means that the ac source reactance x_s is 0.2 in pu. If an additional resistance equal to 10% of the reactance is considered, then, for a SCR of 5, the ac source inductance L_s is 0.2 pu and the resistance R_s is 0.02 pu.

Since the VSCs are connected to non-infinite ac sources, then, VSC₁ is modelled as (4.29) and VSC₂ is modelled (4.28), where the PLL is taken into consideration. The PLL parameters are selected as indicated by (2.41), where α_{PLL} is selected as 5 Hz (0.1 pu). About the VSC's setpoints, i_{f2}^{qref} is set to zero, i_{f1}^{qref} is set to -0.3 pu (to improve the voltage u_g), and e_1^{ref} is set to 1 pu. Table 4.8 shows the eigenvalues of the system for i_{f2}^{dref} equal to +1, 0, and -1 .

It can be shown through the participation factors that the eigenvalues shown in Table 4.8 are related to the dynamics of the system, as follow:

1. $\lambda_{1,2}$ are related to the resonance phenomenon of the dc grid.
2. $\lambda_{3,4,7,8}$ are, in most of the cases, related to the dynamics of the VCC, i.e. the currents $i_{f1}^d, i_{f1}^q, i_{f2}^d$ and i_{f2}^q , respectively.
3. $\lambda_{5,6}$ are related to the dynamics of the DVC.
4. $\lambda_{9,10}$ are related to the PLL dynamics of VSC₁.
5. $\lambda_{11,12}$ are related to the PLL dynamics of VSC₂.

Similarly to Section 4.7.2, the eigenvalues $\lambda_{1,2}$ are identified as the relevant ones in terms of the stability of the system. As in the previous case, the eigenvalues related to the resonance phenomenon of the dc side are not well damped. Moreover, when i_{f2}^{dref} is set to -1 pu the real parts of $\lambda_{1,2}$ are positive in both cases, differently from the infinite ac source case, where only in case 2 the real parts of $\lambda_{1,2}$ are positive. This implies that a *weak* ac source deteriorates the dc side dynamic performance of the system compared to the cases with a *strong* ac source. In order to clarify this, Figure 4.11 plots the pole placement for both, case 1 and case 2, with i_{f2}^{dref} changed from $+1$ to -1 pu in steps of -0.1 pu. It can be seen that, in case 1, the system turns unstable when i_{f2}^{dref} is approximately less than -0.81 pu, while, in case 2, the system turns unstable when i_{f2}^{dref} is approximately less than -0.45 pu. In Table 4.9, the maximum power that can be transferred without losing stability, for SCRs equal to infinite, 5 and 3, and the DVC set as case 1 and 2 are presented. It can be seen from the table that the lower the SCR (the weaker the system), the lower the power limit. Note that, in Table 4.9, a positive power direction is from VSC₁ to VSC₂.

The same tests regarding the dc cable length and the integral term of the DVC are performed in this section. As in section 4.7.2, the length of the cable is varied from 50 km to 150 km in steps of 5 km, the integral term k_{ie1} is changed from 0 to 12.31 pu in steps of 0.62 pu. In addition, the controller parameters are set according to case 2, and the SCR of the ac systems is 5. Similarly to Section 4.7.2, Figure 4.12(a) shows that the increase of the length turns the eigenvalues $\lambda_{1,2}$ better damped, although the system remains unstable for a length 150 km. Figure 4.12(b) shows that the variation of k_{ie1} does not impact $\lambda_{1,2}$ considerably. However, it has a negative effect on the eigenvalues related to the DVC. The eigenvalues related to the DVC move towards the unstable region, and actually becomes unstable. If $\lambda_{1,2}$ are the eigenvalues of interest, k_{ie1} can be considered zero, meaning that, as in Section 4.7.2, the DVC can be implemented as a proportional controller.

Table 4.8: Eigenvalues for different values of i_{f2}^{dref} and DVC parameters, non-infinite ac sources

| Set-points | Eigenvalues case 1 (pu) | Eigenvalues case 2 (pu) |
|----------------------|--------------------------------------|-------------------------------------|
| $i_{f2}^{dref} = +1$ | $\lambda_{1,2} = -0.73 \pm j6.90$ | $\lambda_{1,2} = -1.07 \pm j6.68$ |
| | $\lambda_3 = -4.58$ | $\lambda_3 = -5.35$ |
| | $\lambda_4 = -3.89$ | $\lambda_4 = -3.88$ |
| | $\lambda_5 = -0.45$ | $\lambda_5 = -0.80$ |
| | $\lambda_6 = -0.08$ | $\lambda_6 = -0.15$ |
| | $\lambda_7 = -4.04$ | $\lambda_7 = -4.04$ |
| | $\lambda_8 = -4.20$ | $\lambda_8 = -4.02$ |
| | $\lambda_{9,10} = -0.10 \pm j0.02$ | $\lambda_{9,10} = -0.10 \pm j0.01$ |
| | $\lambda_{11,12} = -0.10 \pm j0.02$ | $\lambda_{11,12} = -0.10 \pm j0.02$ |
| $i_{f2}^{dref} = 0$ | $\lambda_{1,2} = -0.38 \pm j7.13$ | $\lambda_{1,2} = -0.44 \pm j7.27$ |
| | $\lambda_3 = -3.28$ | $\lambda_{3,4} = -1.81 \pm j0.50$ |
| | $\lambda_4 = -0.55$ | $\lambda_5 = -4.04$ |
| | $\lambda_5 = -0.14$ | $\lambda_6 = -0.17$ |
| | $\lambda_6 = -4.04$ | $\lambda_7 = -4.04$ |
| | $\lambda_7 = -4.04$ | $\lambda_8 = -4.04$ |
| | $\lambda_8 = -4.04$ | $\lambda_9 = -0.12$ |
| | $\lambda_{9,10} = -0.08 \pm j0.01$ | $\lambda_{10} = -0.08$ |
| | $\lambda_{11,12} = -0.10$ | $\lambda_{11,12} = -0.10$ |
| $i_{f2}^{dref} = -1$ | $\lambda_{1,2} = 0.11 \pm j7.32$ | $\lambda_{1,2} = 0.69 \pm j7.51$ |
| | $\lambda_3 = -1.76$ | $\lambda_{3,4} = -0.83 \pm j1.56$ |
| | $\lambda_4 = -0.94$ | |
| | $\lambda_5 = -4.22$ | $\lambda_5 = -4.22$ |
| | $\lambda_6 = -0.08$ | $\lambda_6 = -0.15$ |
| | $\lambda_7 = -4.04$ | $\lambda_7 = -4.04$ |
| | $\lambda_8 = -3.88$ | $\lambda_8 = -3.88$ |
| | $\lambda_{9,10} = -0.09 \pm j0.03$ | $\lambda_{9,10} = -0.09 \pm j0.03$ |
| | $\lambda_{11,12} = -0.10 \pm j0.001$ | $\lambda_{11,12} = -0.1 \pm j0.001$ |

Table 4.9: Maximum power transfer for different SCRs and DVC set as case 1 and 2

| Cases | SCR = Inf. | SCR = 5 | SCR=3 |
|--------|------------|---------|-------|
| Case 1 | 1.51 | 0.81 | 0.64 |
| Case 2 | 0.81 | 0.45 | 0.36 |

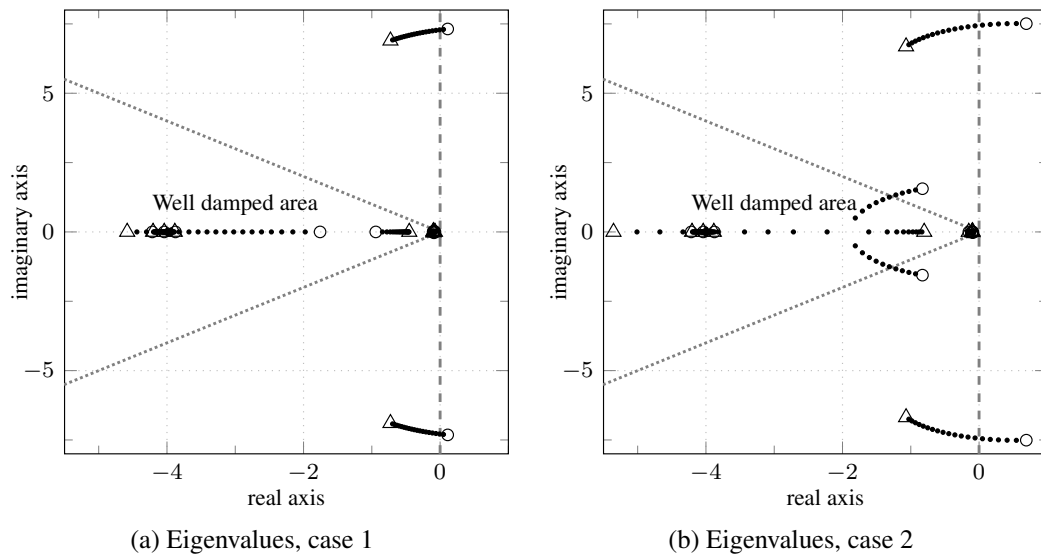


Figure 4.11: Eigenvalues of the system for i_{f2}^{dref} from +1 (Δ) to -1 (\circ), in steps of -0.1. The cable length is 50 km. The SCRs of the ac systems is 5.

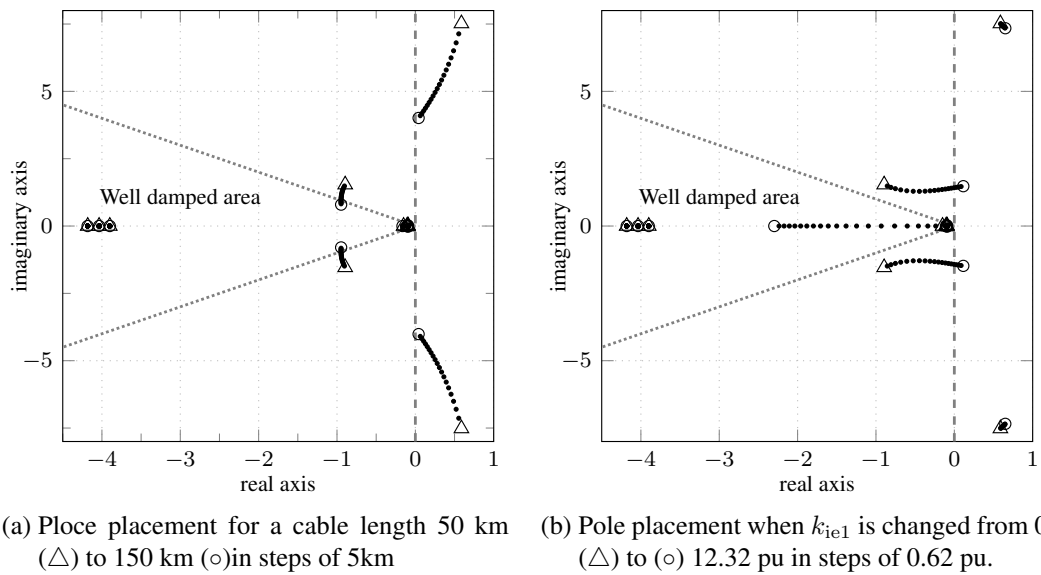


Figure 4.12: Eigenvalues of the system for $i_{f2}^{dref} = -1$, case 2 and SCR of 5.

4.7.4 VSCs connected to non-infinite ac sources with an shunt capacitor at the PCC

The results of the eigenvalue analysis for a system in which an ac capacitor is connected at the PCC is briefly presented in this section. The ac capacitor susceptance is 3 pu, the DVC parameters are set as defined in case 2, and the cable length is 50 km. Figure 4.13 shows the pole placement when i_{f2}^{dref} is changed from +1 to -1 for two different reactive power injections, $Q_{g1} = 0$ and $Q_{g1} = 0.3$. The poles related to the dc-side resonance, $\lambda_{1,2}$ remain inside the stable area for all power transfers, which is different from a similar case with no ac capacitor. New poles which are related with the ac-side resonance appear, and it is found that they move into the RHP as the converter consumes more reactive power. A close-up look of the ac-side resonance related poles is depicted in Figure 4.14, and it can be seen that the system is unstable when i_{f1}^{dref} is positive. In fact, the system is unstable as long as i_{f1}^{dref} is greater than -0.4 pu. This is opposite to the finding related to the dc-side instability, in which the instability occurred when i_{f1}^{dref} is lower than certain value, such as -0.45 pu for the case without capacitor. This is further studied using the frequency domain approach presented in Chapter 5.

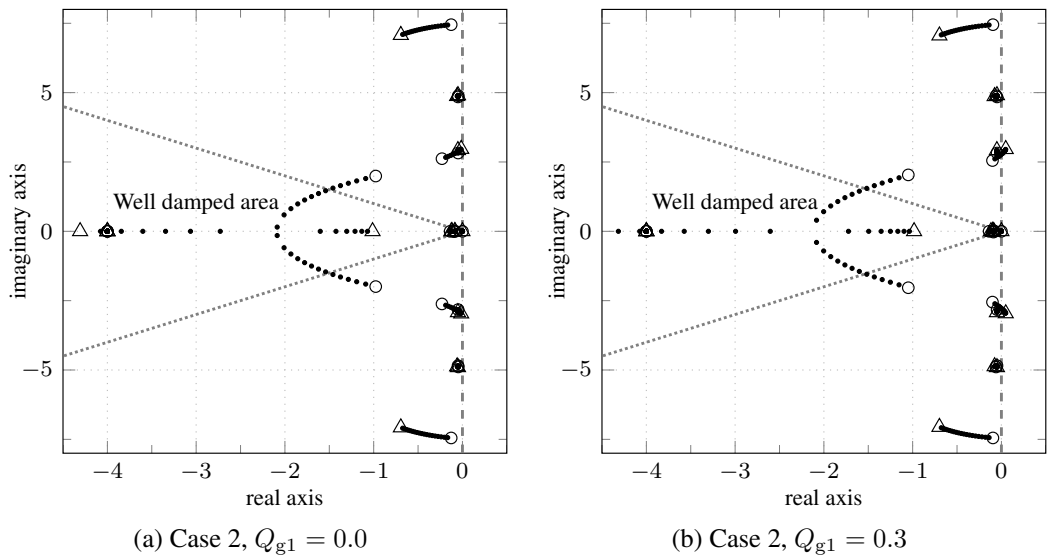


Figure 4.13: Eigenvalues of the system for i_{f2}^{dref} from +1 (\triangle) to -1 (\circ), in steps of -0.1 . The cable length is 50 km. The SCRs of the ac systems are 5.

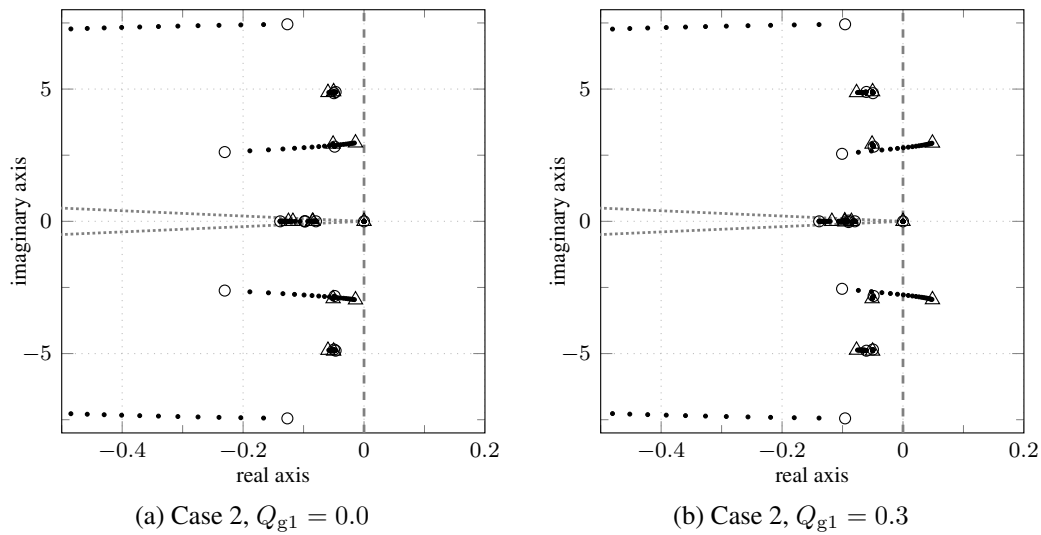


Figure 4.14: Eigenvalues of the system for i_{f2}^{dref} from +1 (Δ) to -1 (\circ), in steps of -0.1. The cable length is 50 km. The SCRs of the ac systems are 5.

4.8 Conclusions

In this chapter, the development of a state space model of a VSC-HVDC system has been presented. A modular approach has been adopted, which means that the system is divided into subsystems which are modelled individually. Afterwards, the subsystems are merged in order to form the system state space model of interest. The modelling approach is not restricted to a particular configuration, which means that more complex HVDC structures, such as MTDC systems can be modelled with the proposed modelling approach. For the sake of simplicity, the dynamic analysis in this chapter has been carried out for a two-terminal VSC-HVDC system.

The dynamic analysis of a two-terminal VSC-HVDC system has been performed through eigenvalue analysis. The analysis reveals that the unstable oscillations found in Section 3.3 through simulations are due to the fact that unstable eigenvalues appear when the gains of the DVC are high, and when the power transfer exceeds a certain value. Moreover, it has been indicated that the instability is related to the dc-side resonance phenomenon. Actually, it has been shown that, when removing the dc-side resonance by modelling the cable as a resistance, the eigenvalues are all located in the well damped area. The effects of the strength of the ac system to which the VSCs are connected have been also analyzed. It has been shown that the weaker the ac system, the more limited the power transmission from the stability point of view is. The effects of an ac capacitor connected at the PCC have also been investigated. It has been shown that the connection of an ac capacitor manage to damp the resonance phenomenon. However, in the studied conditions, the ac side resonances introduced by the LC circuit in the ac side introduce stability problems which are related to the amount of reactive power compensation.

Additional tests have been performed with the aim of studying the impact of other factors on the stability of the system. The increase of the dc cable length improves the dynamic performance of the system, since it makes the eigenvalues $\lambda_{1,2}$ to move towards the stable region as the length increases. The increase of the integral term of the DVC seems not to have any effect on $\lambda_{1,2}$, but its impact on the DVC related poles is considerable. The increase of the VCC bandwidth of the VSC which controls the power has shown not to have almost any effect on the poles of the system. Increasing the speed of the VCC bandwidth of the VSC which controls the direct-voltage has shown to improve the dynamic performance, confirming the rule that the DVC bandwidth should be at least ten times smaller than the VCC bandwidth.

Although eigenvalue analysis has been helpful in establishing the influence of different parameters on the dynamic performance of the system, it does not give a clear reason why the system turns unstable. For instance, it is not clear why the direction of the power matters on the stability of the system, or why the resonance of the dc grid becomes undamped when the proportional gain of the DVC increases. In order to gain a better understanding on the origin of the instability, a frequency domain approach is presented in Chapter 5. The frequency domain analysis provides other tools such as bode plots and the nyquist criteria, which are also of help on the investigation the nature of the unstable cases.

Chapter 5

Frequency domain analysis on HVDC systems

In Chapter 4, it has been found through eigenvalue analysis that, in some particular situations, a two-terminal VSC-HVDC system becomes unstable. The investigation indicates that the instability is related to the interaction between the dc side resonance phenomenon and the VSC which controls the direct-voltage. For a given system, this instability depends on the parameters of the DVC and the direction of the power transfer. However, the origin of the instability has not been clarified. In this chapter, some of the remaining questions from Chapter 4 are investigated through the frequency response of the different elements that compose the system. The system under analysis is divided into subsystems whose *passivity* properties are studied. The two-terminal VSC-HVDC system from Chapter 4 is still studied in this chapter. The dc-grid subsystem and the VSC subsystem are defined and their transfer functions are derived. The properties of the transfer functions are studied in order to find out the conditions that can lead to instability.

5.1 Stability analysis using a frequency domain approach

The stability of the SISO feedback system shown in Figure 5.1 can be evaluated through the frequency response of the transfer functions, $h_1(s)$ and $h_2(s)$. According to [56], a stable linear SISO system is passive if, and only if,

$$\operatorname{Re}[h(j\omega)] \geq 0, \forall \omega \geq 0 \quad (5.1)$$

where $h(s)$ is the closed-loop transfer function of the system shown in Figure 5.1 given by

$$h(s) = \frac{h_1(s)}{1 + h_1(s)h_2(s)}. \quad (5.2)$$

Moreover, the system is dissipative if,

$$\operatorname{Re}[h(j\omega)] > 0, \forall \omega \geq 0. \quad (5.3)$$

It is claimed also in [56] that $h(s)$ is dissipative if either $h_1(s)$ or $h_2(s)$ is dissipative, and the other is at least passive. However, the converse is not true. That is, if one of the subsystems is not passive (i.e. the real part of say $h_1(j\omega)$ is negative for some $\omega \geq 0$), then, $h(s)$ is not necessarily non passive, or unstable. In that case, the Nyquist criterion can be used to finally determine the conditions in which the system $h(s)$ is unstable, as will be shown in this chapter.

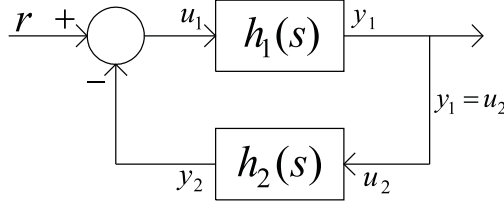


Figure 5.1: SISO feedback system

Here, the VSC-HVDC system is modelled by an equivalent SISO system similar to the one shown in Figure 5.1. Thus, the stability of the system can be studied by analyzing the passivity properties of the subsystems at different frequencies, particularly, for frequencies around the one of the dc side resonance phenomenon.

5.2 Preliminary considerations

In order to derive an equivalent SISO system for the two-terminal VSC-HVDC under examination, the following simplifications are made:

1. The integral gain of the DVC is set to zero since it has been shown that it has a negligible effect on the dc-side resonance-related eigenvalues.
2. The VSC which controls the active power, VSC₂, is modelled as a constant power device since it has been shown that the bandwidth of the current controller does not impact the location of the other eigenvalues.

The first simplification implies that the linearized DVC is modelled as

$$\Delta i_{f1}^{dref} = k_{pe1}(\Delta e_1^{ref} - \Delta e_1). \quad (5.4)$$

Moreover, the currents injected by VSC₁ and VSC₂ are

$$i_1 = \frac{P_1}{e_1}, \quad i_2 = \frac{P_2}{e_2} \quad (5.5)$$

where P_2 is constant since VSC₂ is modelled as a constant power device. That means that $P_2 = P_{20}$. Then, from (5.5), the linearized injected currents are

$$\Delta i_1 = -\frac{P_{10}}{e_{10}^2} \Delta e_1 + \frac{1}{e_{10}} \Delta P_1 \quad (5.6)$$

$$\Delta i_2 = -\frac{P_{20}}{e_{20}^2} \Delta e_2 \quad (5.7)$$

or, Δi_1 and Δi_2 can be represented as

$$\Delta i_1 = \frac{1}{R_{10}} \Delta e_1 + \Delta i_1^* \quad (5.8)$$

$$\Delta i_2 = \frac{1}{R_{20}} \Delta e_2 \quad (5.9)$$

where R_{10} and R_{20} are equivalent resistances, given by

$$R_{10} = -\frac{e_{10}^2}{P_{10}}, \quad R_{20} = -\frac{e_{20}^2}{P_{20}}, \quad (5.10)$$

with $\Delta i_1^* = \Delta P_1 / e_{10}$ ¹. Note that the resistances R_{10} and R_{20} can take negative values and that they have opposite signs. Furthermore, P_{10} , P_{20} , e_{10} and e_{20} are the initial operating powers and direct voltages that comes from the initial steady state of the system. Physically, (5.8) means that the current variation Δi_1 has two components, one component, which is *resistive* and proportional to the voltage variation Δe_1 , and another component, Δi_1^* , which comes from the converter dynamics. Similarly, (5.9) means that the current Δi_2 represents a resistive current which is proportional to the voltage Δe_2 . From (5.8) and (5.9), the two-terminal VSC-HVDC system can be modelled as illustrated in Figure 5.2. In the figure, the capacitors C_{eq1} and C_{eq2} are the parallel of the corresponding VSC capacitor and the dc cable equivalent capacitor.

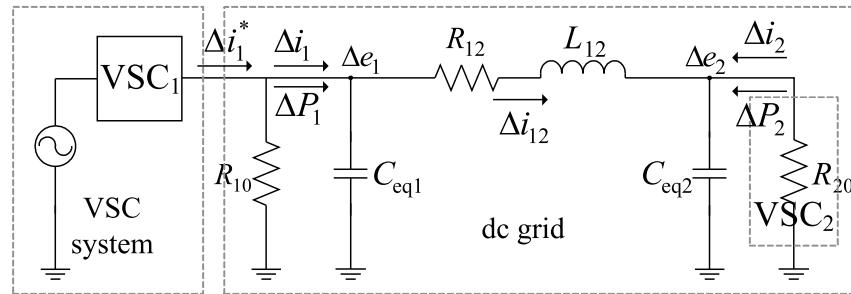


Figure 5.2: Linearized model of the VSC-HVDC system. C_{eq1} and C_{eq2} are the parallel equivalent of the converter capacitor and the dc cable capacitance

In Figure 5.2 two subsystems can be identified. The first subsystem is the dc grid (enclosed in the dashed box labeled as “dc grid” in the figure) whose input is the current Δi_1^* and output is voltage Δe_1 . The second subsystem is the VSC-system (enclosed in the dashed box labeled as “VSC system” in the figure) which is controlling the direct-voltage. In this case, the input is the voltage error $\Delta u_1 = \Delta e_1^{\text{ref}} - \Delta e_1$, which is used by the DVC to set the current reference, $\Delta i_{f1}^{\text{dref}}$, which, likewise, defines the current output Δi_1^* , injected to the dc grid. Therefore, the system shown in Figure 5.2 can be represented by the block diagram shown in Figure 5.3. In the figure, $F(s)$ is the VSC-system transfer function and $G(s)$ is the dc grid transfer function. A useful identity is

$$R_{12} = R_{10} + R_{20} \quad (5.11)$$

¹Some authors use the superscript * to denote a reference to a controller. However, in this thesis, references are indicated with the superscript ref. Then, Δi_1^* should not be confused with a current reference.

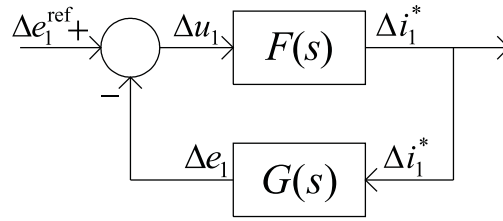


Figure 5.3: Block diagram of the simplified VSC-HVDC system

which can be shown with the help of the equivalent circuit of the dc side in steady state conditions, depicted in Figure 5.4. From the figure, the steady-state current i_{120} can be expressed as

$$i_{120} = \frac{e_{10}}{R_{10}} = -\frac{e_{20}}{R_{20}} = \frac{e_{10} - e_{20}}{R_{12}} \quad (5.12)$$

From (5.12), two relationships can be derived

$$e_{20} = -\frac{R_{20}}{R_{10}}e_{10} \quad (5.13)$$

$$\frac{e_{10}}{R_{10}} = \frac{e_{10} - e_{20}}{R_{12}} \quad (5.14)$$

Entering (5.13) into (5.14), (5.11) is obtained.

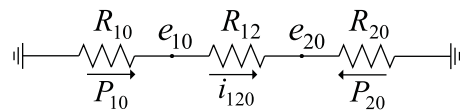


Figure 5.4: Representation of the dc side in steady state conditions.

5.3 The dc grid transfer function

The dc grid system, in this case, is the Π model of the cable along with the resistances R_{10} and R_{20} . The system is represented in the Laplace domain in Figure 5.5.

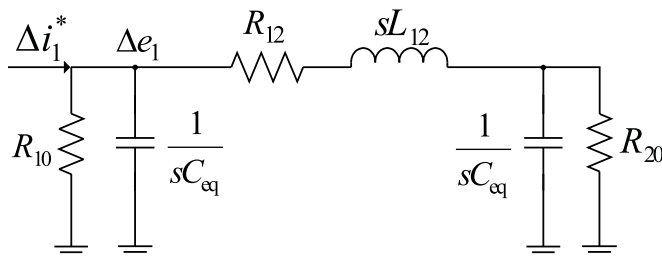


Figure 5.5: DC grid model

The capacitances C_{eq1} and C_{eq2} , shown in Figure 5.2, are considered equal to C_{eq} , since the VSC capacitors are equal for both VSCs in the studied case. In an electrical circuit, the

voltage Δe_1 is obtained as $Z_{dc}(s)\Delta i_1^*$, where $Z_{dc}(s)$ is the equivalent impedance. Then, the transfer function $G(s)$ is the impedance $Z_{dc}(s)$, as

$$\frac{\Delta e_1}{\Delta i_1^*} = Z_{dc}(s) = G(s) \quad (5.15)$$

The equivalent impedance $Z_{dc}(s)$ seen from the point where the current Δi_1^* is injected is

$$\frac{C_{eq}^{-1}(s^2 + (\omega_{r1} + \omega_{c2})s + \omega_{lc}^2 + \omega_{r1}\omega_{c2})}{s^3 + (\omega_{r1} + \omega_{c1} + \omega_{c2})s^2 + (2\omega_{lc}^2 + \omega_{c1}\omega_{c2} + \omega_{r1}(\omega_{c1} + \omega_{c2}))s + 2\omega_{lc}^2(\omega_{c1} + \omega_{c2})} \quad (5.16)$$

where

$$\omega_{c1} = \frac{1}{R_{10}C_{eq}}, \quad \omega_{c2} = \frac{1}{R_{20}C_{eq}}, \quad \omega_{lc}^2 = \frac{1}{L_{12}C_{eq}}, \quad \omega_{r1} = \frac{R_{12}}{L_{12}}. \quad (5.17)$$

The denominator of (5.16) is a third order polynomial whose roots are difficult to obtain analytically. A term “ δ ” can be added and subtracted from the denominator of (5.16) without modifying it. If

$$\delta = -\omega_{c1}\omega_{c2}(\omega_{c1} + \omega_{c2}), \quad (5.18)$$

then, it can be shown that (5.16) can be also expressed as

$$G(s) = \frac{C_{eq}^{-1}n(s)}{(s + \omega_{c1} + \omega_{c2})(d(s) + \omega_{c1}\omega_{c2}) + \delta} \quad (5.19)$$

where

$$n(s) = s^2 + (\omega_{r1} + \omega_{c2})s + \omega_{lc}^2 + \omega_{r1}\omega_{c2} \quad (5.20)$$

$$d(s) = s^2 + \omega_{r1}s + 2\omega_{lc}^2 \quad (5.21)$$

The roots can be found approximately by neglecting δ in the denominator of (5.19). In order to do that, it should be shown that

$$|2\omega_{lc}^2(\omega_{c1} + \omega_{c2})| \gg |\delta| \quad (5.22)$$

In order to determine in which conditions (5.22) is fulfilled, let us begin with some useful inequalities. First, the steady state initial powers are limited by the rated power of the VSCs. That is

$$|P_{10}| \leq 1, \quad |P_{20}| \leq 1 \quad (5.23)$$

assuming also, for the sake of simplicity, that the direct-voltages are approximated to 1 pu, then, the inverse of resistances R_{10} and R_{20} are limited by

$$0 \leq \frac{1}{|R_{10}|} \leq 1, \quad 0 \leq \frac{1}{|R_{20}|} \leq 1. \quad (5.24)$$

Moreover, considering that R_{10} and R_{20} are of opposite signs, the inverse of the product of the resistances are approximately

$$-1 \leq \frac{1}{R_{10}R_{20}} \leq 0. \quad (5.25)$$

Considering (5.11), δ , $\omega_{c1} + \omega_{c2}$ and $\omega_{c1}\omega_{c2}$ are

$$\delta = -\frac{R_{12}}{C_{\text{eq}}^3 R_{10}^2 R_{20}^2}, \quad \omega_{c1} + \omega_{c2} = \frac{R_{12}}{C_{\text{eq}} R_{10} R_{20}}, \quad \omega_{c1}\omega_{c2} = \frac{1}{C_{\text{eq}}^2 R_{10} R_{20}} \quad (5.26)$$

and, using (5.25), δ , $\omega_{c1} + \omega_{c2}$ and $\omega_{c1}\omega_{c2}$ are bounded as

$$-\frac{R_{12}}{C_{\text{eq}}^3} \leq \delta \leq 0, \quad -\frac{R_{12}}{C_{\text{eq}}} \leq \omega_{c1} + \omega_{c2} \leq 0, \quad -\frac{1}{C_{\text{eq}}^2} \leq \omega_{c1}\omega_{c2} \leq 0. \quad (5.27)$$

Equation (5.22) can be rewritten as

$$|2\omega_{\text{lc}}^2 R_{12} C_{\text{eq}}| |\omega_{c1}\omega_{c2}| \gg |\omega_{c1} + \omega_{c2}| |\omega_{c1}\omega_{c2}|. \quad (5.28)$$

If $|\omega_{c1}\omega_{c2}| \neq 0^1$, then, (5.28) is fulfilled if

$$|2\omega_{\text{lc}}^2 R_{12} C_{\text{eq}}| \gg |\omega_{c1} + \omega_{c2}|. \quad (5.29)$$

Using (5.27), (5.29) is fulfilled if

$$2\omega_{\text{lc}}^2 R_{12} C_{\text{eq}} \gg \frac{R_{12}}{C_{\text{eq}}} \quad (5.30)$$

where the absolute value symbol of the left side of (5.29) is removed in (5.30) since all the variables are positive. Considering the definition of ω_{lc}^2 made on (5.17), (5.30) is fulfilled if

$$\frac{L_{12}}{C_{\text{eq}}} \ll 2 \quad (5.31)$$

which means that, in order to neglect δ , (5.31) must be fulfilled. It should be kept in mind that C_{eq} is an equivalent capacitor conformed by the parallel of the converter capacitor and the cable capacitance. As a rule of thumb, we can say that (5.31) is fulfilled if

$$\frac{L_{12}}{C_{\text{eq}}} = z_0^2 \leq 0.02 \quad (5.32)$$

since it can be considered that $0.02 \ll 2$. From the values in Tables 4.2 and 4.1, for a 50 km cable, z_0^2 is equal to

$$z_0^2 = \frac{1.975 \cdot 10^{-4} \cdot 50}{3.142 + 0.0195 \cdot 50} = 0.0024$$

which means that δ can be neglected in (5.19). Then, the dc grid transfer function can be approximated by the following transfer function

$$G'(s) = \frac{C_{\text{eq}}^{-1} n(s)}{(s + \omega_{c1} + \omega_{c2})(d(s) + \omega_{c1}\omega_{c2})}. \quad (5.33)$$

Moreover, if (5.32) is fulfilled it means

$$2\omega_{\text{lc}}^2 \gg \omega_{c1}\omega_{c2}. \quad (5.34)$$

¹ $|\omega_{c1}\omega_{c2}|$ is zero when either P_{10} or P_{20} is zero. In that case, δ is zero as well, so the poles of 5.16 can be found analytically.

Then, the dc grid transfer function can be further approximated to

$$\tilde{G}(s) = \frac{C_{\text{eq}}^{-1}n(s)}{(s + \omega_{c1} + \omega_{c2})d(s)} \quad (5.35)$$

where the poles can be calculated as

$$\lambda_1 = -(\omega_{c1} + \omega_{c2}), \quad \lambda_{2,3} = -\frac{\omega_{r1}}{2} \pm \sqrt{2}\omega_{1c} \sqrt{\frac{\omega_{r1}^2}{8\omega_{1c}^2} - 1}. \quad (5.36)$$

Observe that the transfer function of the dc grid presents an unstable pole, λ_1 , for P_{10} and P_{20} different from zero. If either P_{10} or P_{20} are zero, then $p_1 = 0$. Therefore, when either P_{10} and P_{20} are different from zero, Bode diagrams cannot be used to study $\tilde{G}(s)$ since any sinusoidal input will make the output to grow unboundedly. However, this does not mean that the closed-loop of the overall system is unstable, since, as mentioned in [58], an unstable system can be stabilized with a feedback controller. Moreover, the value of the unstable eigenvalue indicates the value that the controller bandwidth must be in order to stabilize the system [58]. From (5.27), the upper bound of λ_1 is R_{12}/C_{eq} , which is small compared to $\lambda_{2,3}$. The small upper bound of λ_1 suggests that the term $\omega_{c1} + \omega_{c2}$ can be neglected if the controller gain is sufficiently high. This suggest that (5.35) can be further approximated to the marginally stable transfer function

$$\tilde{G}_0(s) = \frac{C_{\text{eq}}^{-1}n(s)}{s \times d(s)} \quad (5.37)$$

if the controller bandwidth is sufficiently high to stabilize the system. For example, Figure 5.6(a) shows the unstable system $G'(s)$ driven by a proportional controller with a gain k , and Figure 5.6(b) shows the approximated marginally stable system, $\tilde{G}_0(s)$, driven by the same controller. The eigenvalues of both feedback systems are calculated for k varied from

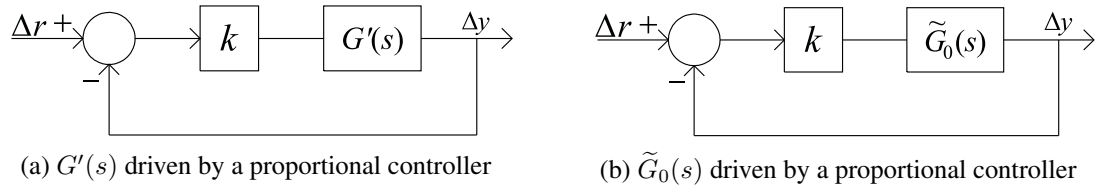


Figure 5.6: Feedback systems controlled by a proportional controller

0.01 to 100 and the error¹ between the eigenvalues of the two systems are shown in Figure 5.7. In both systems there are three eigenvalues, one real and two complex conjugated. In Figure 5.7(a), the errors of the real and the imaginary components of the complex eigenvalues are shown, while in Figure 5.7(b) the error of the real eigenvalue is shown. It can be seen in Figure 5.7(a) that, in the first case, the error is small for the range in which k is varied. Furthermore, Figure 5.7(b) shows for the real eigenvalue that the error is significantly high for small values of k . For instance, for k lower than 0.5, the error is above 2.6%. However, the error decreases quickly as k increases, falling below 1% when k is higher than 1.4. It should be mentioned that the x axes in Figure 5.7(a) and 5.7(b) are not the same for the sake of clarity.

¹There error is defined as $|\frac{\lambda_{G'} - \lambda_{\tilde{G}_0}}{\lambda_{G'}}|100\%$, where $\lambda_{G'}$ is a pole of G' and $\lambda_{\tilde{G}_0}$ is a pole of \tilde{G}_0 .

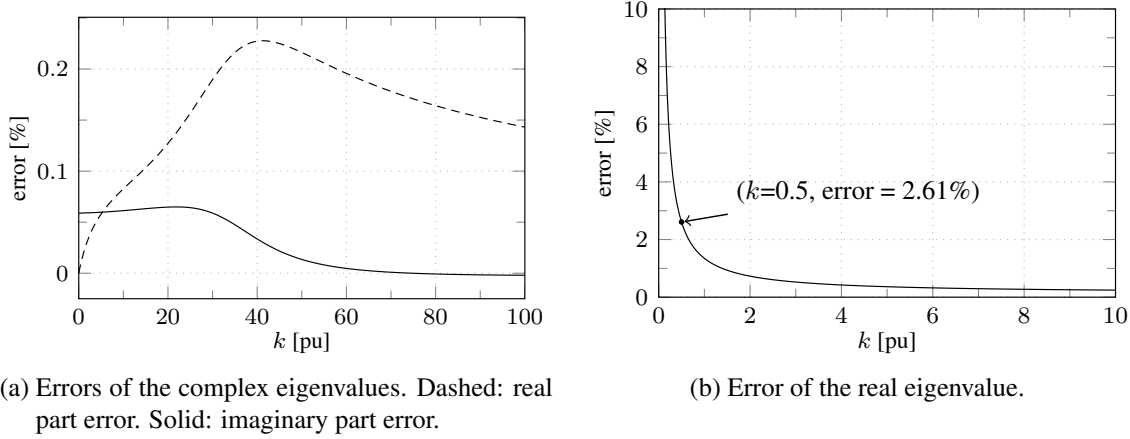


Figure 5.7: Comparison between the eigenvalues of the systems shown in Figure 5.6

Although not rigorous, the analysis above suggests that the dc grid transfer function can be approximated by the marginally stable system (5.37). The advantage of using the approximation (5.37) is that Bode plots can be used to study the frequency response of $\tilde{G}_0(s)$ and its implication on the stability of the system can be drawn.

5.4 The VSC-system transfer function

In this section, the VSC-system transfer function, named $F(s)$ in Figure 5.3, is derived. In this case, the input to the transfer function is the voltage error Δu_1 , and the output is Δi_1^* . We can recall from (5.8) that the current Δi_1^* is

$$\Delta i_1^* = \frac{\Delta P_1}{e_{10}} \quad (5.38)$$

Since the converter is assumed lossless, the active power at the ac side of VSC₁ is equal to the power at the dc-side. That is

$$P_1 = u_{c1}^d i_{f1}^d + u_{c1}^q i_{f1}^q \quad (5.39)$$

which in terms of small deviations, ΔP_1 is

$$\Delta P_1 = u_{c10}^d \Delta i_{f1}^d + u_{c10}^q \Delta i_{f1}^q + i_{f10}^d \Delta u_{c1}^d + i_{f10}^q \Delta u_{c1}^q. \quad (5.40)$$

Therefore, the current Δi_1^* , defined in (5.38), can be expressed as

$$\Delta i_1^* = \frac{1}{e_{10}} (u_{c10}^d \Delta i_{f1}^d + u_{c10}^q \Delta i_{f1}^q + i_{f10}^d \Delta u_{c1}^d + i_{f10}^q \Delta u_{c1}^q). \quad (5.41)$$

Considering the ac side of VSC₁ shown in Figure 4.6, the voltages u_{c1}^d and u_{c1}^q in the converter dq frame are expressed in the Laplace domain as

$$u_{c1}^d = u_{s1}^d - (R_{t1} + sL_{t1})i_{f1}^d + \omega_{g1}L_{t1}i_{f1}^q \quad (5.42a)$$

$$u_{c1}^q = u_{s1}^q - (R_{t1} + sL_{t1})i_{f1}^q - \omega_{g1}L_{t1}i_{f1}^d \quad (5.42b)$$

where $L_{t1} = L_{f1} + L_{s1}$ and $R_{t1} = R_{f1} + R_{s1}$. Furthermore, as explained in Section 4.4.1, u_{s1}^d and u_{s1}^q can be expressed as in (4.22). Then, (5.42) can be linearized and expressed in the converter dq -frame as

$$\Delta u_{c1}^d = u_{s10}^q \Delta \theta_{g1} - (R_{t1} + sL_{t1}) \Delta i_{f1}^d + \omega_{g1} L_{t1} \Delta i_{f1}^q + i_{f10}^q L_{t1} \Delta \omega_{g1} \quad (5.43a)$$

$$\Delta u_{c1}^q = -u_{s10}^d \Delta \theta_{g1} - (R_{t1} + sL_{t1}) \Delta i_{f1}^q - \omega_{g1} L_{t1} \Delta i_{f1}^d - i_{f10}^d L_{t1} \Delta \omega_{g1} \quad (5.43b)$$

and, in steady state u_{c10}^d and u_{c10}^q are

$$u_{c10}^d = u_{s10}^d - R_{t1} i_{f10}^d + \omega_{g10} L_{t1} i_{f10}^q \quad (5.44a)$$

$$u_{c10}^q = u_{s10}^q - R_{t1} i_{f10}^q - \omega_{g10} L_{t1} i_{f10}^d \quad (5.44b)$$

It should be highlighted that if VSC₁ is connected to an infinite ac source, L_{s1} and R_{s1} are zero and \underline{u}_s^{dq} is equal to \underline{u}_g^{dq} ; this voltage is constant, meaning that $\Delta \underline{u}_g^{dq}$ is zero. Continuing with (5.43), if (5.44) is put into (5.41), the following is the current injected to the dc-side by the VSC₁

$$\Delta i_1^* = -\frac{i_{f10}^d L_{t1}}{e_{10}} (s + z_1^d) \Delta i_{f1}^d - \frac{i_{f10}^q L_{t1}}{e_{10}} (s + z_1^q) \Delta i_{f1}^q + \frac{u_{s10}^q i_{f10}^d - u_{s10}^d i_{f10}^q}{e_{10}} \Delta \theta_g \quad (5.45)$$

where z_1^d and z_1^q are

$$z_1^d = 2 \frac{R_{t1}}{L_{t1}} - \frac{u_{s10}^d}{i_{f10}^d L_{t1}}, \quad z_1^q = 2 \frac{R_{t1}}{L_{t1}} - \frac{u_{s10}^q}{i_{f10}^q L_{t1}}. \quad (5.46)$$

Moreover, from (4.11a), the transfer function of current controller is

$$\Delta i_{f1}^d = \frac{\alpha_1}{s + \alpha_1} \Delta i_{f1}^{dref}, \quad \Delta i_{f1}^q = \frac{\alpha_1}{s + \alpha_1} \Delta i_{f1}^{qref}. \quad (5.47)$$

Entering (5.47) into (5.45) and assuming that i_{f1}^{qref} is constant ($\Delta i_{f1}^{qref} = 0$), then, (5.45) becomes

$$\Delta i_1^* = -\frac{\alpha_1 i_{f10}^d L_{t1}}{e_{10}} \left(\frac{s + z_1^d}{s + \alpha_1} \right) \Delta i_{f1}^{dref} + \frac{Q_{s10}}{e_{10}} \Delta \theta_{g1} \quad (5.48)$$

where Q_{s0} is $u_{s0}^q i_{f0}^d - u_{s0}^d i_{f0}^q$. As mentioned earlier, it is assumed that the DVC of VSC₁ is a proportional controller, then, the DVC is modelled as (5.4). Equation (5.4) can be entered into (5.48) and the following is obtained

$$\Delta i_1^* = F_c(s) \Delta u + \frac{Q_{s10}}{e_{10}} \Delta \theta_g \quad (5.49)$$

where:

$$F_c(s) = -\frac{\alpha_1 i_{f10}^d L_{t1} k_{pe1}}{e_{10}} \left(\frac{s + z_1^d}{s + \alpha_1} \right). \quad (5.50)$$

If the ac system is infinite, the angle variation $\Delta \theta_g$ is zero since \underline{u}_g is the voltage of an infinite ac source. Then, the VSC-system transfer function $F(s)$ for infinite ac sources is

$$F(s) = \frac{\Delta i_{dc1}^*}{\Delta u_1} = -\frac{\alpha_1 i_{f10}^d L_{f1} k_{pe1}}{e_{10}} \left(\frac{s + z_1^d}{s + \alpha_1} \right) \quad (5.51)$$

where

$$z_1^d = 2 \frac{R_{f1}}{L_{f1}} - \frac{u_{g10}^d}{i_{f10}^d L_{f1}}. \quad (5.52)$$

Continuing with (5.49), $\Delta\theta_{g1}$ has to be expressed in terms of Δi_{f1}^d and Δi_{f1}^q in order to derive a transfer function similar to (5.51). The angle θ_{g1} and the frequency ω_{g1} are estimated by the PLL block, and it is defined by (4.27). In the Laplace domain, (4.27) is expressed as

$$\Delta\theta_{g1} = \frac{k_{pll}s + k_{ill}}{s^2} \Delta u_{g1}^q = F_{pll}(s) \Delta u_{g1}^q. \quad (5.53)$$

Considering the voltage drop over the ac source impedance and that $\Delta\omega_{g1} = s\theta_{g1}$, then, Δu_{g1}^q can be expressed as

$$\Delta u_{g1}^q = -(u_{s10}^d + s i_{f10}^d L_{s1}) \Delta\theta_{g1} - (R_{s1} + s L_{s1}) \Delta i_{f1}^q - \omega_{g10} L_{s1} \Delta i_{f1}^d. \quad (5.54)$$

Combining (5.53) and (5.54), the following is expression for the angle $\Delta\theta_{g1}$ is obtained

$$\Delta\theta_{g1} = -\frac{(R_{s1} + s L_{s1}) F_{pll}(s)}{1 + (u_{s10}^d + s i_{f10}^d L_{s1}) F_{pll}(s)} \Delta i_{f1}^q - \frac{\omega_{g10} L_{s1} F_{pll}(s)}{1 + (u_{s10}^d + s i_{f10}^d L_{s1}) F_{pll}(s)} \Delta i_{f1}^d. \quad (5.55)$$

Considering (5.47), and that Δi_f^{qref} is zero, (5.55) becomes

$$\Delta\theta_{g1} = \frac{e_{10}}{Q_{s10}} F_{\theta}(s) \Delta u_1. \quad (5.56)$$

where

$$F_{\theta}(s) = -\frac{\omega_{g10} Q_{s10} L_{s1} k_{pe1} F_{pll}(s)}{e_{10} (1 + (u_{s10}^d + s i_{f10}^d L_{s1}) F_{pll}(s)) (s + \alpha_1)}. \quad (5.57)$$

Finally, using (5.56) into (5.49), the transfer function $F(s)$ for the non-infinite ac source case is

$$F(s) = F_c(s) + F_{\theta}(s). \quad (5.58)$$

In a more general case, the VSC-system transfer can be found using (4.48). Then, the state space model of VSC₁, where the input is Δu_1 and the output is Δi_1^* , can be written as

$$\frac{d\Delta \mathbf{x}_{s1}^e}{dt} = \mathbf{A}_{s1}^e \Delta \mathbf{x}_{s1}^e - \mathbf{B}_{se1}^e \Delta u_1 \quad (5.59)$$

$$\Delta i_1^* = \mathbf{C}_{s1}^e \Delta \mathbf{x}_{s1}^e + \mathbf{D}_{sr1}^e \mathbf{q} \Delta u_1 \quad (5.60)$$

where \mathbf{q} is $[1 \ 0]^T$. The VSC-system transfer function is then

$$F(s) = \frac{\Delta i_1^*}{\Delta u_1} = [-\mathbf{C}_{s1}^e (s\mathbf{I} - \mathbf{A}_{s1}^e)^{-1} \mathbf{B}_{se1}^e + \mathbf{D}_{sr1}^e \mathbf{q}] \quad (5.61)$$

Note that (5.59) represents either a VSC connected to infinite or non-infinite sources, or a VSC system in which an ac capacitor is connected at the PCC. Finally, the system shown in Figure 5.3 can be represented by the SISO feedback system shown in Figure 5.8, where $F(s)$ is the VSC-system transfer function given by either (5.51), (5.58) or (5.61), and \tilde{G}_0 is the approximated dc grid transfer function given by (5.37).

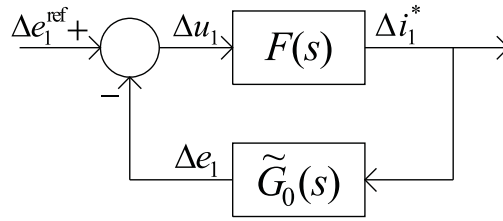


Figure 5.8: System block diagram with the approximated dc grid transfer function.

5.5 Stability investigation using a frequency domain approach

In this section the stability of the two-terminal VSC-HVDC system is studied considering the passivity properties of F and \tilde{G}_0 , and the Nyquist criterion. The Bode diagrams of both, F and \tilde{G}_0 , are used to study their passivity properties at different frequencies.

5.5.1 Analysis of the dc-grid subsystem

Figure 5.9 shows the frequency response of \tilde{G}_0 for two power transfers: -1 and $+1$ ¹. Observe that the numerator of \tilde{G}_0 , given by (5.20), depends on the initial operating point. Along with both plots, the frequency response of the transfer function of the dc cable, G_0 is also plotted. The transfer function G_0^2 is obtained when the resistances R_{10} and R_{20} are not considered as part of the model dc grid model, and it is

$$G_0(s) = \frac{C_{\text{eq}}^{-1}(s^2 + \omega_{r1}s + \omega_{lc}^2)}{s(s^2 + \omega_{r1}s + 2\omega_{lc}^2)} \quad (5.62)$$

which is independent from the operating point. Moreover, the data used for \tilde{G}_0 and G_0 are as indicated in Tables 4.1 and 4.2 for a cable length of 50 km. It can be seen from Figure 5.9 that \tilde{G}_0 and G_0 are passive systems since they are marginally stable and their phase angle is always between -90° and 90° . Moreover, it can be seen that the three cases match closely to the dc cable transfer function, G_0 , which suggests that the frequency response of the actual impedance seen from the point where VSC₁ is connected could be utilized for the analysis instead of \tilde{G}_0 . The fact that the dc grid transfer function is passive implies that VSC-system transfer function is non-passive in the unstable cases. This is analyzed next.

5.5.2 Analysis of the VSC subsystem - The infinite ac source case

Let us begin the analysis with the case when VSC₁ is connected to an infinite ac source. In this case, the VSC-system transfer function is defined by (5.51). It can be seen from (5.51)

¹In this case, a positive power transfer means that the power flow direction is from VSC₁ to VSC₂

²Actually, G_0 coincides with (5.19) when $P_{20} = 0$.

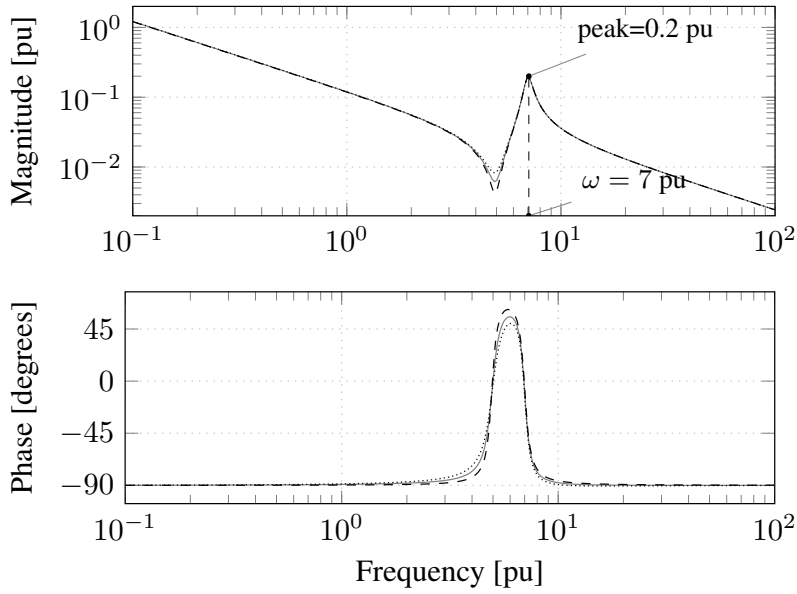


Figure 5.9: Frequency response of: Solid gray: $G_0(s)$. Solid black: $\tilde{G}_0(s)$ for a power flow of -1 . Dotted $\tilde{G}_0(s)$ for a power flow of $+1$

that F is a stable system that has one pole, $-\alpha_1$, and one zero, $-z_1^d$. Moreover, (5.52) shows that z_1^d depends on the operating point. If the resistance R_{f1} is neglected, $-z_1^d$ is

$$-z_1^d = \frac{u_{g10}^d}{i_{f10}^d L_{f1}}. \quad (5.63)$$

It can be seen that the zero is located in the left-half plane (LHP) of the s-plane when the i_{f10}^d is negative (VSC₁ absorbs power from the dc system), and the zero is located in the RHP when i_{f10}^d is positive (VSC₁ injects power to the dc grid). In [56], it is mentioned that the necessary conditions for the system to be *strictly positive real* (or in other words, dissipative) are that the system must be strictly stable and the system must be strictly minimum-phase. From (5.52), F is minimum phase as long as VSC₁ absorbs power from the dc side, meaning that, for this power direction, the necessary conditions for F to be passivity are fulfilled when VSC₁ absorbs power from the dc grid. However, when the direction is opposite, F is non-minimum phase. This means that F is non-passive for any positive power transfer. Moreover, as mentioned in [58], RHP zeros impose a limitation on the bandwidth that the closed-loop system can achieve, meaning that high controller gains can lead the system to instability. This explains why for the same positive power direction, the system with higher DVC gains (case 2 in Table 4.3) results unstable.

Figure 5.10(a) shows the frequency response of F for negative power transfers. It can be seen that the phase angle of F is between -20° and 0° for power transfers of -1 , -0.8 and -0.5 , meaning that the system is passive (even dissipative). On the other hand, Figure 5.10(b) shows the frequency response of F for three positive power transfers, $+1$, $+0.8$ and $+0.5$. It can be seen that, in this case, the phase angle is around zero for low frequencies, and it decreases towards -180° as the frequency increases, which means that F is non-passive for high frequencies and positive power transfers. Besides, it can be seen that the magnitude of F increases as the absolute value of the power transfer increases.

5.5. Stability investigation using a frequency domain approach

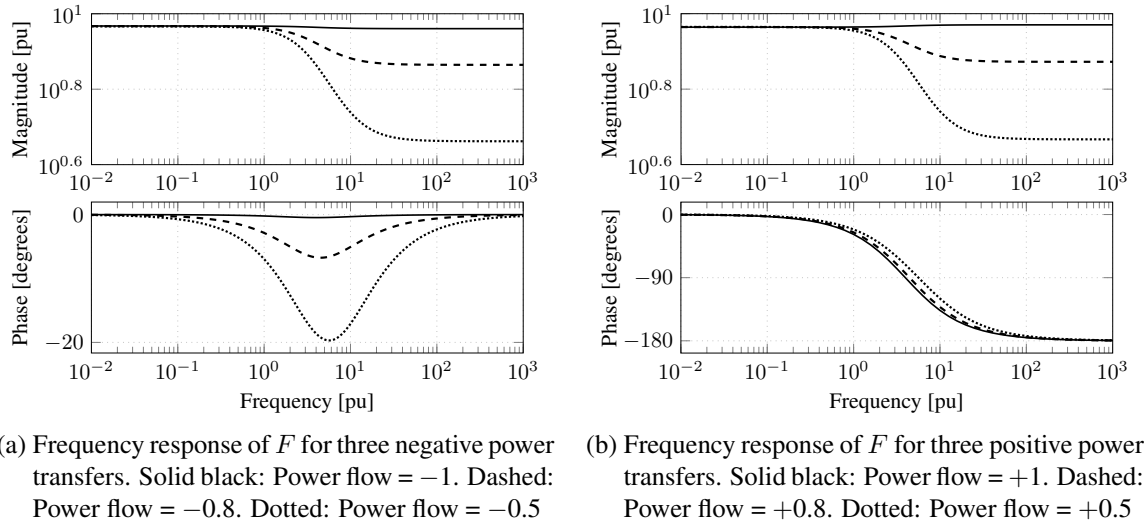


Figure 5.10: Frequency response of F for different power transfer (Positive means from VSC₁ to VSC₂)

5.5.3 The VSC admittance and the dc grid impedance

Similarly to [40], the VSC-HVDC system can be seen as an interconnection of the VSC *admittance* and the dc grid *impedance*. The VSC admittance for some frequency ω is defined by

$$F(j\omega) = F_x(\omega) + jF_y(\omega) \quad (5.64)$$

where F_x is the VSC conductance and F_y is the VSC susceptance. The VSC conductance dissipates energy when it is positive, and accumulates energy when it is negative. In addition, the dc grid impedance for some frequency ω is defined by

$$\tilde{G}_0(j\omega) = \tilde{G}_{0x}(\omega) + j\tilde{G}_{0y}(\omega) \quad (5.65)$$

where $\tilde{G}_{0x}(\omega)$ is the dc grid resistance and \tilde{G}_{0y} is the dc grid reactance. The dc grid impedance has a peak at the resonance frequency, and its resistance is positive for all frequencies. Then, the resonance phenomenon originated in the dc grid is dissipated by the VSC-system if the VSC conductance is positive. However, the resonance phenomena may be amplified if the VSC conductance is negative. To determine whether the system is stable or not, the Nyquist stability criterion can be used. According to the Nyquist criterion, if the open loop system, $F(s)\tilde{G}_0(s)$ is stable, then, the closed loop system is stable if the mapping of $F(s)\tilde{G}_0(s)$ along the Nyquist path does not encircle the point $-1 + j0$ in the clock-wise direction. That is

$$F_x(\omega_{180^\circ})\tilde{G}_{x0}(\omega_{180^\circ}) - F_y(\omega_{180^\circ})\tilde{G}_{y0}(\omega_{180^\circ}) > -1 \quad (5.66)$$

where ω_{180° is the frequency at which the phase of $F(j\omega)\tilde{G}_0(j\omega)$ is 180° or, in other words, it is the frequency at which $F(j\omega)\tilde{G}_0(j\omega)$ intersects the real axis of the complex plane. In this particular case, it has been shown that, at low frequencies, F is conductive and positive, while \tilde{G}_0 is capacitive, meaning that the real part of $F(j\omega)\tilde{G}_0(j\omega)$ is very small at

low frequencies. At high frequencies, F is conductive but negative, while \tilde{G}_0 is capacitive and very small. This means that the real part of $F(j\omega)\tilde{G}_0(j\omega)$ is much smaller. At the resonance frequency it can be assumed that \tilde{G}_0 is purely resistive (meaning that \tilde{G}_{y0} is zero), then, the condition (5.66) turns approximately into

$$F_x(\omega_{\text{dcre}})\tilde{G}_{x0}(\omega_{\text{dcre}}) > -1 \quad (5.67)$$

where ω_{dcre} is the dc-side resonance frequency. This means that the Nyquist criterion is not fulfilled if the VSC conductance is negative and high at ω_{dcre} . For example, in Figure 5.11, the real and imaginary parts of \tilde{G}_0 and F are plotted. The figure shows that, for negative power transfers, the resonance peak finds a positive VSC conductance, meaning that the resonance is dissipated and (5.67) is fulfilled. On the other hand, Figure 5.12 shows the real and imaginary parts of \tilde{G}_0 and F when the power transfer is positive. It can be seen that the resonance peak coincides with negative VSC conductances, which increases as the power transfer increases. The more negative the VSC conductance is, the higher the risk for the system to turn unstable. This explains why, for the investigated system and for the given set of controller parameters, the system is more prone to instability when the transmitted power transfer increases (from VSC₁ to VSC₂).

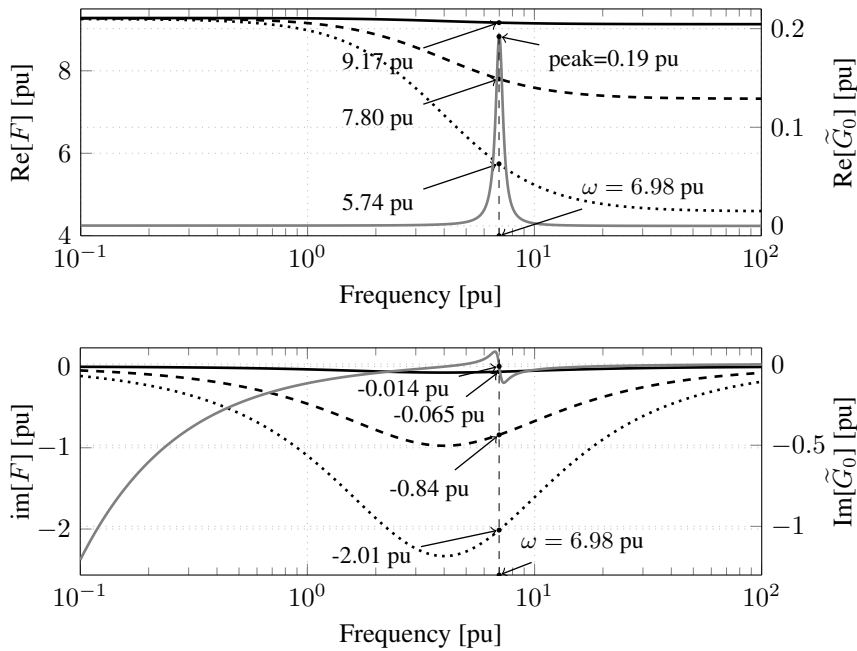


Figure 5.11: Real (up) and imaginary (down) parts of F and \tilde{G}_0 for negative power transfers. Solid gray: \tilde{G}_0 . Solid black: F for -1 . Dashed: F for -0.8 . Dotted: F for -0.5

The effects of the dc cable length on the stability of the system can be studied with the help of Figure 5.13. The figure shows the real part of F together with \tilde{G}_0 plotted for three cable lengths, 50 km, 100 km, and 150 km. It can be seen that, as the dc cable length increases, the resonance peak and the resonance frequency decrease. At the decreasing resonance frequency of the dc cable, the VSC conductances becomes less negative, thus reducing the risk of instability. Observe that, the VSC conductance is positive at the cable resonance frequency.

5.5. Stability investigation using a frequency domain approach

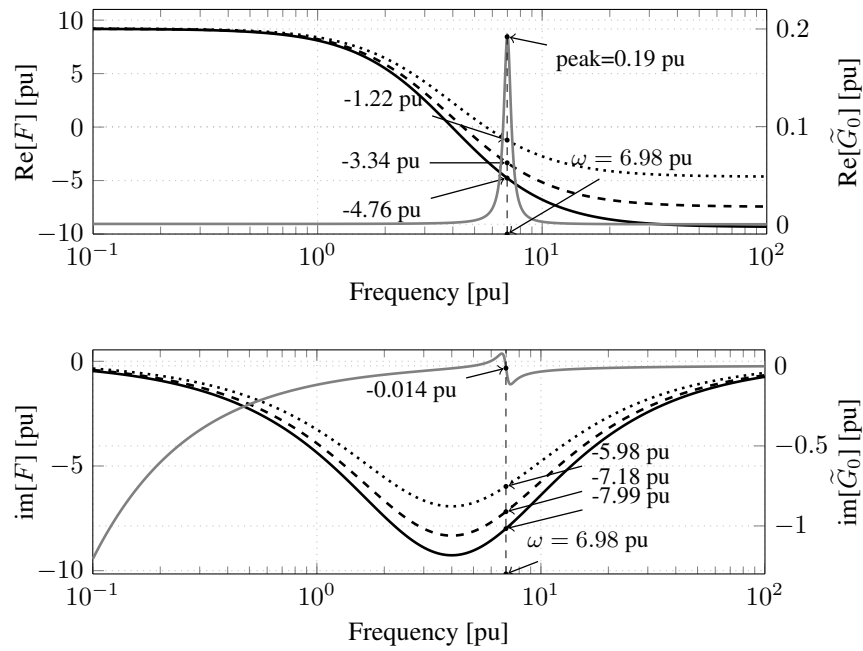


Figure 5.12: Real (up) and imaginary (down) parts of F and \tilde{G}_0 for positive power transfers. Solid Gray: \tilde{G}_0 . Solid: F for +1. Dashed: F for +0.8. Dotted: F for +0.5

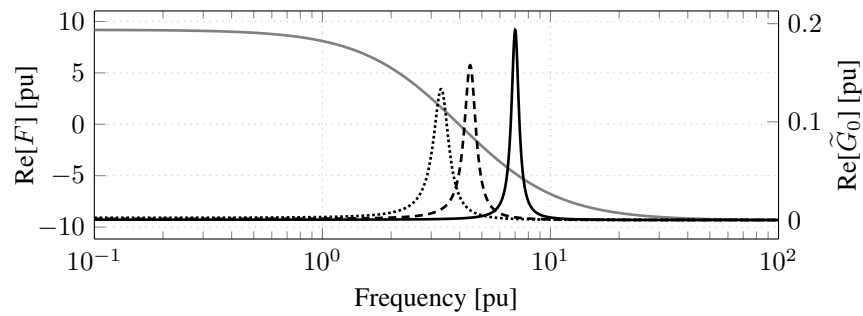


Figure 5.13: Gray: $\text{Re}[F]$ for +1. Solid: $\text{Re}[\tilde{G}_0]$ for 50 km. Dashed: $\text{Re}[\tilde{G}_0]$ for 100 km. Dotted: $\text{Re}[\tilde{G}_0]$ for 150 km

The effects of the DVC parameters on the VSC conductance are shown in Figure 5.14. The parameters shown in Table 4.3 are used to plot the VSC conductance, but considering k_{ie1} as zero. It can be seen that for case 2 the VSC conductance is more negative than case 1¹ at the resonance frequency, which indicates that the risk that instability takes place is higher in case 2 compared to case 1. The impact of the proportional gain k_{pe} on the VSC conductance can also be inferred from (5.51) since it shows explicitly that the magnitude of F depends on k_{pe1} . The higher k_{pe1} , the more negative the VSC conductance, making the system prone to instability. This explains why the power transfer limit is lower with high DVC gains compared with low DVC gains, as shown in Table 4.9.

Finally, a direct relationship between the controller parameters, the dc side characteristics, and the operating point can be obtained by assuming that the dc side resonance occurs at

¹Remember that case 1 corresponds to the case in which the DVC gains are high, while case 2 corresponds to the case in which the DVC gains are low.

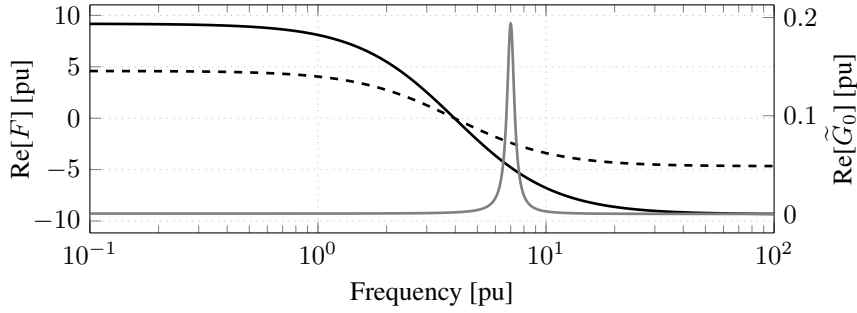


Figure 5.14: Real part of F and \tilde{G}_0 for a power transfer equal to +1 pu and different cases. Gray: $\text{Re}[\tilde{G}_0]$. Solid: $\text{Re}[F]$ for case 2. Dashed: $\text{Re}[F]$ for case 1.

a high frequency. This can be assumed since it can be seen that the VSC conductance decreases to a minimum value which remains almost constant as the frequency increases. From (5.58), at high frequencies, the VSC conductance is approximately

$$F_x = -\frac{\alpha_1 i_{f10}^d L_{t1} k_{pe1}}{e_{10}} \quad (5.68)$$

and, assuming that the resonance frequency of the dc cable corresponds to the resonance frequency of a lossless dc cable, i.e.

$$\omega_{res} = \frac{\sqrt{2}}{\sqrt{L_{12} C_{eq}}} \quad (5.69)$$

the peak of the dc grid resistance can be found approximately replacing (5.69) into (5.62). That gives

$$\tilde{G}_{0x} = \frac{L_{12}}{2R_{12}C_{eq}}. \quad (5.70)$$

Using (5.67), and considering that $P_1 = u_{g10}^d i_{f10}^d$, it can be found that the power transfer limit is given by

$$P_{1lim} < \frac{2C_{eq}e_{10}u_{g10}^d R_{12}}{\alpha_1 L_{t1} k_{pe1} L_{12}} \quad (5.71)$$

which is a conservative value, since instability can take place at a VSC conductance higher than the minimum one. Equation (5.71) shows that the (positive) power transfer is reduced if either the system is the ac system is weak, the bandwidth of the controllers are high, the cable resistance is small, etc.

5.5.4 Analysis of the VSC subsystem - The non-infinite ac grid case

In Section 4.7.3, eigenvalue analysis has been used to study the stability of VSC-HVDC systems when connected to non-infinite ac grids. From this study, it has been found that the power transfer is further limited when the SCR of the ac grids decreases. Since the dc grid impedance is unchanged (there is no change in the topology), then, the reason for the instability has to do with the VSC conductance. This can be shown by studying the

frequency response of F , this time given by (5.58). Figure 5.15, show the real parts of F and \tilde{G}_0 . F is plotted for SCRs equal to 3, 5 and infinity. It can be seen that the VSC conductance becomes more negative when SCR decreases, i.e. when the system is weaker. The effect of k_{pe} is similar to infinite ac source case as shown by (5.58), meaning that, if k_{pe} is set according to case 2, the VSC conductance is more negative at the dc side resonance frequency compared with case 1.

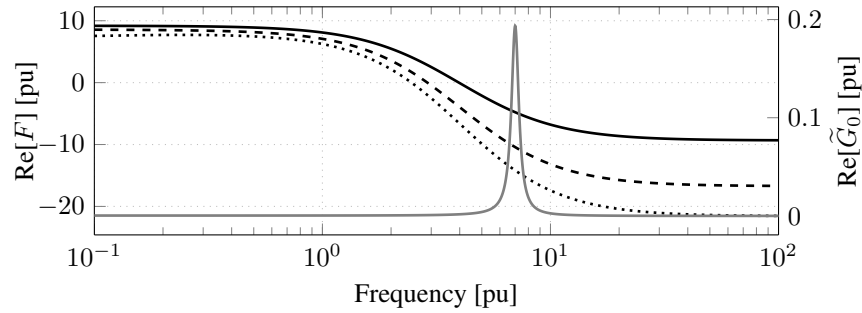


Figure 5.15: Frequency response of F for a power transfer equal to +1 pu, DVC set as case 2, and three different SCRs. Solid: SCR infinite. Dashed: SCR = 5. Dotted: SCR = 3.

5.5.5 Analysis of the VSC subsystem - Capacitor connected at the PCC

In Section 4.7.4 the effects of a capacitor connected at the PCC has been studied with eigenvalue analysis. It has been shown in Section 4.7.4 that the dc-side-resonance-related eigenvalues ($\lambda_{1,2}$) are better damped when the capacitor is connected at the PCC. However, instability has been identified in the system, and it is related to the resonance of the ac side LCL circuit. This is further investigated using the approach developed in this section. In Figures 5.16 and 5.17 the VSC conductance and susceptance are plotted for power transfers of +1 and -1, respectively, and with the DVC parameters as defined for case 2. The VSC conductance and susceptance when there is no ac capacitor is also plotted for the sake of comparison. It can be seen that, when an ac capacitor is connected to the PCC, the VSC subsystem is non passive for some frequencies in both power directions. This is different from the case with no ac capacitor in which the VSC subsystem is passive for negative power transfers and non passive for positive power transfers. Nevertheless, the passivity of the VSC subsystem can be checked at each particular resonance frequency. Concerning the dc side resonance phenomenon, for the case when the power transfer is +1, the VSC conductance is more positive as compared with the case with no ac capacitor meaning that the resonance is better damped. When the power transfer is in the opposite direction, i.e. -1 the VSC conductance is still negative but it is higher, compared to the case when there is no ac capacitor.

From the figures, it can be seen that the VSC conductance presents fairly high resonance peaks. However, at those frequencies, the dc grid resistance is very small, since the dc grid impedance is capacitive. If at the ac-side resonance frequencies the dc grid resistance and the VSC conductance are neglected, the stability of the system can be approximately

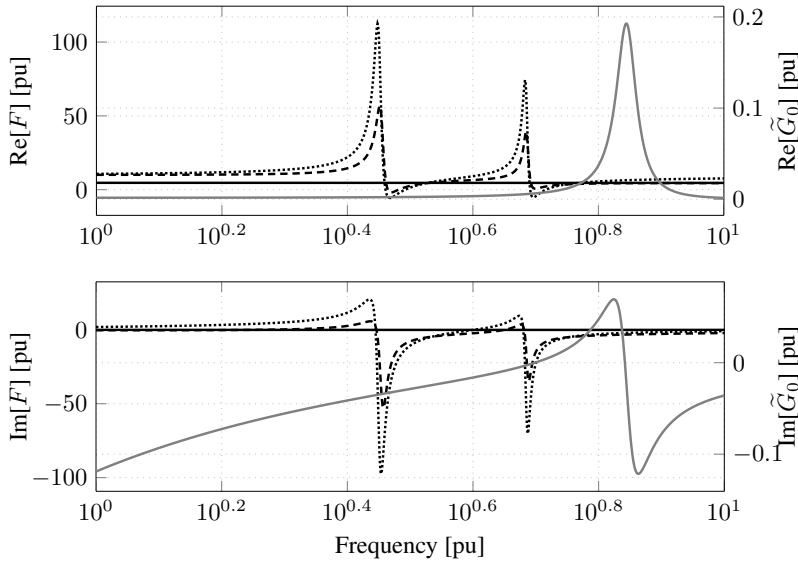


Figure 5.16: Unstable case. Frequency response of \tilde{G}_0 and F with DVC paramters set as case 2 and SCR as 5: Solid gray: $G_0(s)$. Solid black: F for a power transfer of +1 and no ac capacitor, . Dashed: F for a power transfer of +0.5 and ac capacitor. Dotted: F for a power transfer of +1 and ac capacitor

assessed by claiming that the system is stable if

$$F_y(\omega_{acres})\tilde{G}_{0y}(\omega_{acres}) < 1 \quad (5.72)$$

where ω_{acres} is the ac-side resonance frequency under examination. From Figure 5.16, the VSC susceptance peak at the resonance frequency 2.8 pu is around -100 pu and the corresponding dc grid reactance is around -0.034 pu, which makes $F_y G_y$ equal to 3.4 pu, meaning that (5.72) is not fulfilled. At the second resonance frequency, 4.8 pu, the VSC susceptance peak is around -70 pu, while the magnitude of \tilde{G}_0 is around -0.004 pu which means that (5.72) is fulfilled. On the other hand, from Figure 5.17, the VSC susceptance peak is around 80 pu and the dc grid reactance is around -0.032 pu for a resonance frequency of 2.95 pu, which fulfills (5.72) since $F_y G_y$ is negative. The same is true for the second resonance frequency, since the VSC conductance resonance peak is positive, and the dc grid reactance is negative.

Although the VSC admittance and the dc grid impedance has been analyzed considering their definition in this thesis, it is recommendable that the analysis is performed as carried out in [44]. In that way, the ac side resonance is captured without the influence of the VSC system, and then VSC admittance seen as shown in Figure 5.18 can give better information on whether or not the resonance is amplified or damped.

5.5. Stability investigation using a frequency domain approach

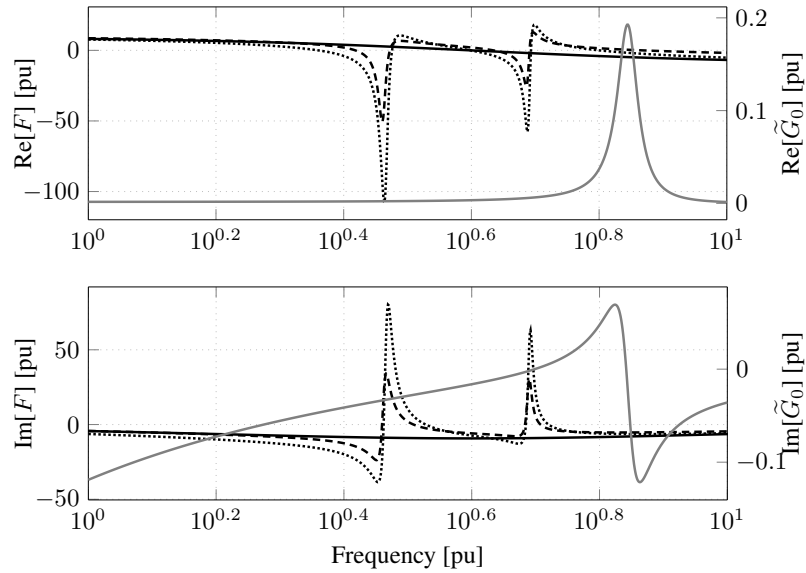


Figure 5.17: Sstable case. Frequency response of \tilde{G}_0 and F with DVC paramters set as case 2 and SCR of 5: Solid gray: $G_0(s)$. Solid black: F for a power transfer of -1 and no ac capacitor, . Dashed: F for a power transfer of -0.5 and ac capacitor. Dotted: F for a power transfer of -1 and ac capacitor

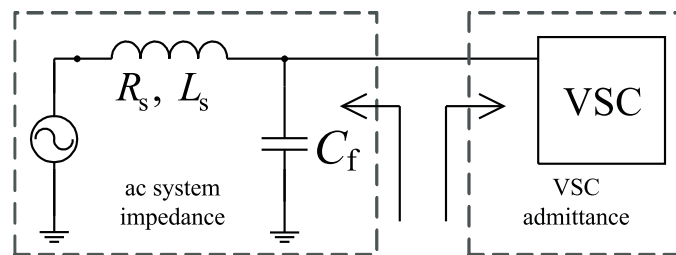


Figure 5.18: AC system impedance and VSC admittance to analyse the ac side resonance

5.6 Conclusions

In this chapter, the dc-side dynamics of the two-terminal VSC-HVDC system has been studied using a frequency domain approach. The VSC-HVDC system has been modelled as a SISO feedback system, in which two subsystems have been defined: the VSC and their dc grid subsystems. The corresponding transfer functions have been derived and the passivity properties have been studied. It has been shown that the dc grid subsystem is an unstable system which can be approximated to a marginally stable system, \tilde{G}_0 . \tilde{G}_0 has been found to be a passive subsystem, meaning that it is not the source of the instability. However, the dc grid subsystem presents a resonance which can interact with the VSC subsystem. The VSC subsystem has been found passive when the VSC, which controls the direct-voltage, absorbs power from the dc grid. This means that, when the VSC absorbs power from the dc side, the system is stable even for high DVC gains. The VSC subsystem is non passive when the VSC injects current into the dc grid which means that there is a risk that the resonance phenomenon developed in the dc side becomes amplified due to the non passive behaviour of the VSC subsystem.

The VSC admittance has been defined also in this chapter, and it is shown that in the unstable cases, the VSC-subsystem presents a “negative conductance” characteristic at the frequencies of interest. When the dc-side resonance encounters a negative VSC conductance, the resonance can be amplified depending on the size of the negative VSC conductance. It has been shown that the following influence the magnitude of the negative VSC conductance:

1. The amount of active power injected by the VSC into the dc grid. The more power is injected into the dc grid, the more negative the VSC conductance.
2. The DVC proportional gain. The higher the DVC proportional gain, the more negative the VSC conductance.
3. The SCR of the ac system to which the VSC it is connected. The weaker the system, the more negative the VSC conductance.

The analysis has been performed for a particular control system. However, the procedure is not restricted to the control system assumed in this chapter. If the interaction between the VSC which controls the direct voltage and the dc grid dynamics is to be investigated, the next procedure can be followed:

1. Identify the resonance frequency and the resonance peak of the dc-side. Commercial tools which calculates the harmonic impedance of electrical networks can be used for this purpose.
2. Determine if the converter conductance is negative at the resonance frequency. Determine also if the Nyquist stability criterion is fulfilled.
3. If the system is unstable, investigate if the magnitude of the converter admittance can be decreased by modifying the controller structure.

Chapter 6

Simulations in a multi-terminal configuration

In this chapter, simulations are performed in order to further investigate the dc network dynamics in VSC-MTDC configurations. A four-terminal HVDC system is modelled in PSCADTM, and its performance when using two control strategies, the voltage-margin and the voltage-droop control, is tested. Some events, such as converter disconnections and operating point changes, are tested for both control strategies and different controller parameters. The effect of other control loops, not studied analytically in this thesis, are investigated in this section as well through simulations.

6.1 System description

The system under analysis is a radial four-terminal VSC-HVDC system, as depicted in Figure 6.1. The cables are modelled as Π sections and their lengths are as shown in the figure. The equivalent cable inductance, capacitance, and resistance per kilometer are as indicated in Table 3.2. The VSCs are two-level converters and they have their ratings as

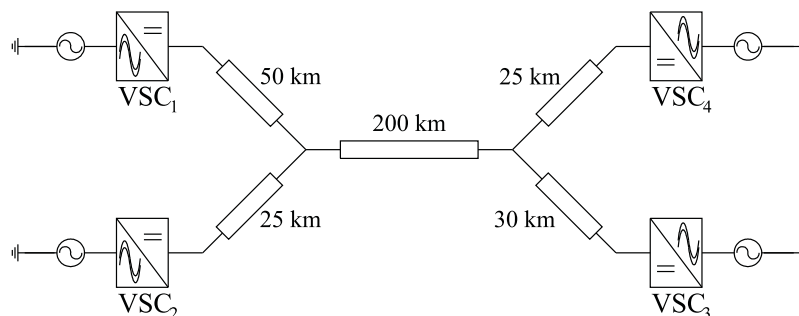


Figure 6.1: System under analysis

indicated in Table 3.1 and Table 4.1, i.e. 600 MVA power rating, 300 kV rated line-to-line voltage in the ac side, and ± 300 kV rated pole-to-pole voltage in the dc side. In

this example, VSC₁ and VSC₂ are set to control the direct-voltage, following a strategy defined in the next sections, and VSC₃ and VSC₄ are set to control the power. Table 6.1 summarizes the controller parameters considered in the simulations. The controllers of VSC₁ and VSC₂ are selected two times faster than VSC₃ and VSC₄ in order to provide a fast voltage regulation in the dc side of the system. In VSC₁ and VSC₂, the recommendation that the DVC should be ten times slower than the VCC is adopted [44,45].

Table 6.1: Controller parameters in per unit

| Parameter | VSC ₁ | VSC ₂ | VSC ₃ | VSC ₄ |
|--|------------------|------------------|------------------|------------------|
| VCC bandwidth (α) | 8.0 | 8.0 | 4.0 | 4.0 |
| DVC nat. res. frequency (ω_n) | 0.8 | 0.8 | – | – |
| DVC damping factor (ξ) | 1.0 | 1.0 | – | – |
| VCC proportional gain (k_p) | 2.0 | 2.0 | 1.0 | 1.0 |
| VCC integral gain (k_i) | 0.02 | 0.02 | 0.01 | 0.01 |
| DVC proportional gain (k_{pe}) | 3.078 | 3.078 | – | – |
| DVC integral gain (k_{ie}) | 1.231 | 1.231 | – | – |

Furthermore, a current limiter is added in order to limit the output of the DVC, as illustrated in Figure 6.2. The limits are set ± 1.3 pu. In some cases, the current limiters are deactivated in order to investigate the effect on the system dynamics.

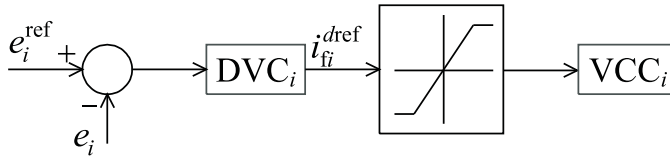


Figure 6.2: Implementation of a current limiter

6.2 Simulated case

The following sequence of events is simulated in the four-terminal VSC-HVDC system:

t=0.0 s: Initially VSC₁ and VSC₂ are controlling the direct-voltage following a certain control strategy. VSC₃ consumes 300 MW and VSC₄'s power is zero.

t=0.5 s: VSC₄ begins increasing its power consumption at a rate of 150 MW/s.

t=1.0 s: VSC₁ is disconnected.

In all cases, the voltage at the VSC₂ dc-side node and the power injected/absorbed by VSC₂ are plotted. The depicted powers are filtered through a low pass filter with a bandwidth of 2000 rad/s in order to remove the high harmonic content present in the power waveforms. However, the direct-voltages are shown unfiltered.

6.3 Voltage-margin control strategy

VSC₁ and VSC₂ are set according to the voltage-margin control discussed in Section 2.5. As illustrated in Figure 6.3, in normal conditions, VSC₁ is in charge of regulating the voltage of the dc network and VSC₂ acts as power regulating converter, supplying 300 MW to the dc network. If VSC₁ is disconnected, the excess of power consumption¹ makes the voltage to decrease, meaning that VSC₂ starts regulating the power when the voltage reaches 0.95 pu. In that case, VSC₂ will carry out the task of regulating the voltage in the dc network.

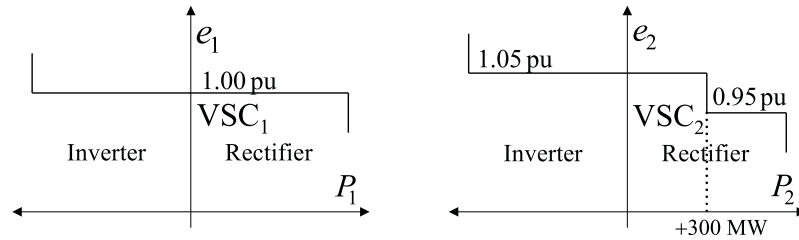


Figure 6.3: Voltage-margin control strategy for VSC₁ (left) and VSC₂ (right).

Through eigenvalue analysis, it can be shown that, when VSC₁ is out of service, the maximum power that VSC₂ can supply to the dc network is 0.8 pu for the given configuration and set of parameters. Figure 6.4 shows the results of the sequence of events stated in

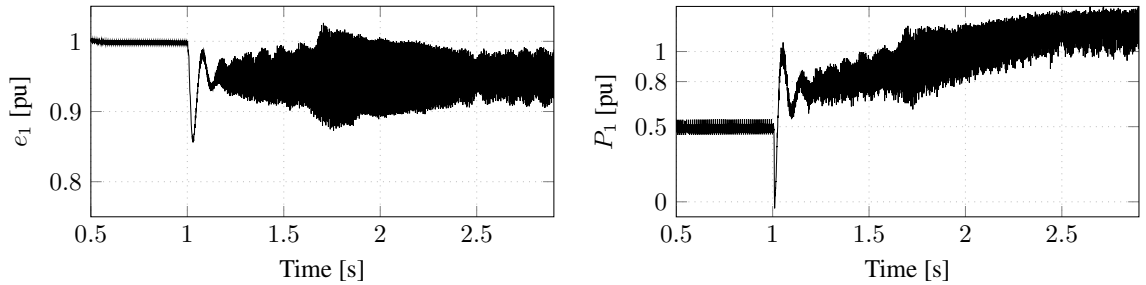


Figure 6.4: Simulated sequence of events. Voltage-margin control. DVC with $\omega_n = 0.8$ and $\xi = 1$. Left: VSC₁ voltage, e_1 . Right: VSC₁ power, P_1 .

Section 6.2. It can be seen that, when the VSC₁ is disconnected, the voltage decreases and oscillates at a frequency of around 11 Hz. This oscillation cannot be explained with the analysis performed in this thesis since it is triggered by a large disturbance, while this thesis deals with the small signal dynamics of the system. VSC₂ takes over the control of the direct voltage and it can be seen that oscillations of 512 Hz appear (see Figure 6.5). It should be noted that the power at which VSC₂ turns unstable is around 0.8 pu, which confirms the limit calculated through eigenvalue analysis. In order to confirm that the oscillations

¹As mentioned in Section 2.5.2, the term “consumption” means that the power flows from the dc network to the ac side of the VSCs. Likewise, the term “supply” means that power flows from the ac side into the dc network.

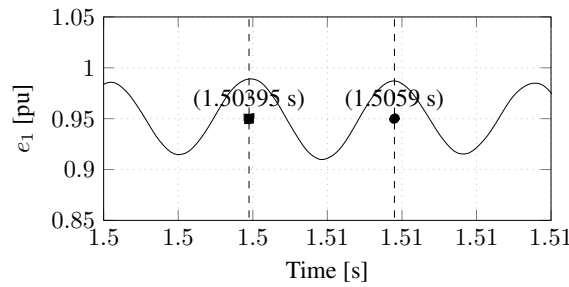


Figure 6.5: Zoom of the voltage e_1 from Figure 6.4 at 1.5s. The period is 1.95ms, then, the frequency is 512 Hz.

are related to the resonance phenomenon which occurs in the dc cable, the impedance frequency scan at the node where VSC₂ is connected is shown in Figure 6.6. The figure shows three resonance peaks occurring at 98 Hz, 284 Hz, and 519 Hz. As studied in Chapter 5, the conductance of VSC₂ becomes negative as the frequency increases. Then, it can be

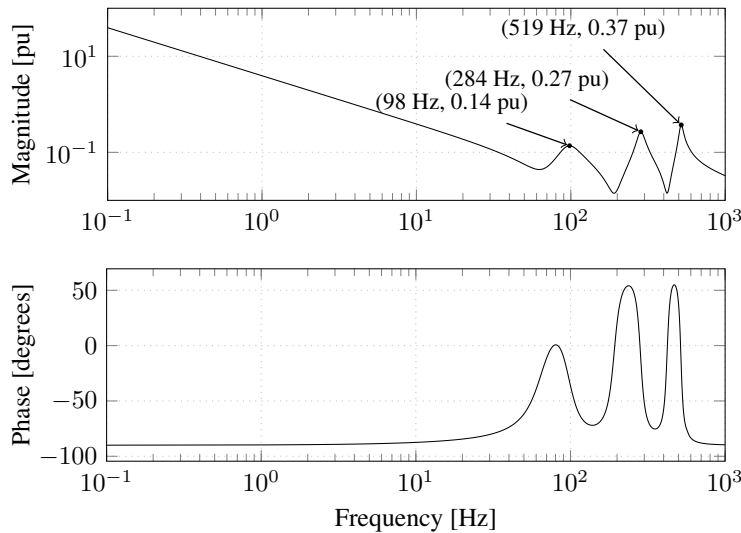


Figure 6.6: Frequency response of the dc grid

inferred that the VSC₂ conductances at 98 Hz and 284 Hz are either positive or not sufficiently negative as to turn the system unstable while at 519 Hz, the VSC₂ conductance is negative and sufficiently low.

Interestingly, Figure 6.7 shows that, when i_{f2}^{qref} is set to 0.2 pu (which means that the VSC injects around 0.2 pu reactive power to the ac system), the dc-side resonance related oscillations appear later. Similarly to Figure 6.4, low frequency oscillations appear at around $t = 2.5s$, which coincides with the development of instability related to the dc side resonance. In order to further investigate whether these low frequency oscillations are related to the saturation characteristic of the current limiters, the same case is run without limiting i_{f2}^{dref} .

The results are shown in Figure 6.8 and it can be seen that the same oscillations appear but the amplitude has increased. Then, it could be that the oscillations are related to the saturation of the voltage generated by the VSC. The VSC cannot deliver a peak-to-peak

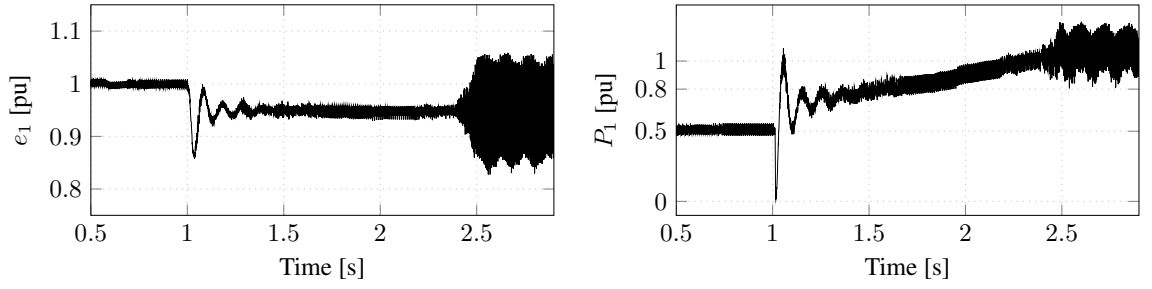


Figure 6.7: Simulated sequence of events. Voltage-margin control. DVC with $\omega_n = 0.8$ and $\xi = 1$. $i_{f2}^{qref} = 0.2$. Left: VSC₁ voltage, e_1 . Right: VSC₁ power, P_1 .

voltage higher than the voltage of its dc-side capacitor¹. Furthermore, Figure 6.9 shows a detailed picture of the direct-voltage at $t = 2.6$ s, and it can be seen that there is again a 512 Hz frequency resonance, which is around the frequency at which the greatest peak appears in the dc grid frequency scan (See Figure 6.6). In order to confirm if the power limit has

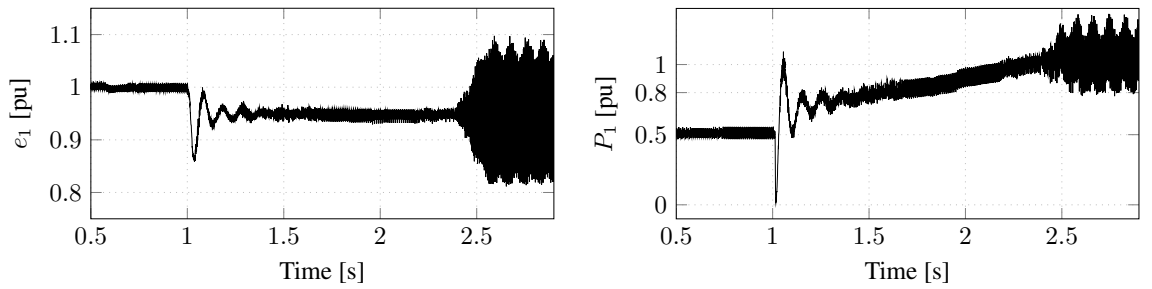


Figure 6.8: Simulated sequence of events. Voltage-margin control. DVC with $\omega_n = 0.8$ and $\xi = 1$. $i_{f2}^{qref} = 0.2$. No current limiter. Left: VSC₁ voltage, e_1 . Right: VSC₁ power, P_1 .

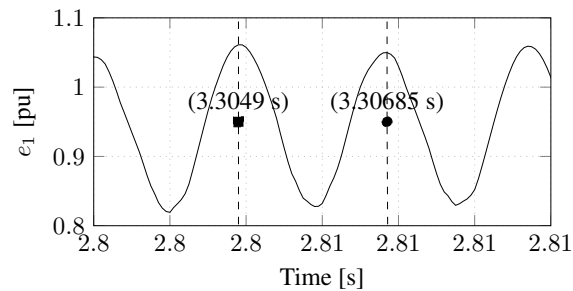


Figure 6.9: Zoom of the voltage e_1 from Figure 6.8 at 2.8s. The period is 1.95ms, then, the frequency is 512 Hz.

increased with the injection of reactive power, the case is run again, but with power the consumption of VSC₄ ramped up to 0.4 pu (240 MW). The results are shown in Figure 6.10, and it can be seen that no oscillations appear even after the VSC₄ has reach 0.4 pu.

From the analysis carried out in Chapter 5, one way to avoid the instability related to the dc side resonance is to decrease the magnitude of the VSC₂ admittance. It has been shown

¹In this case, the PWM is not optimized using zero-sequence voltage injection.

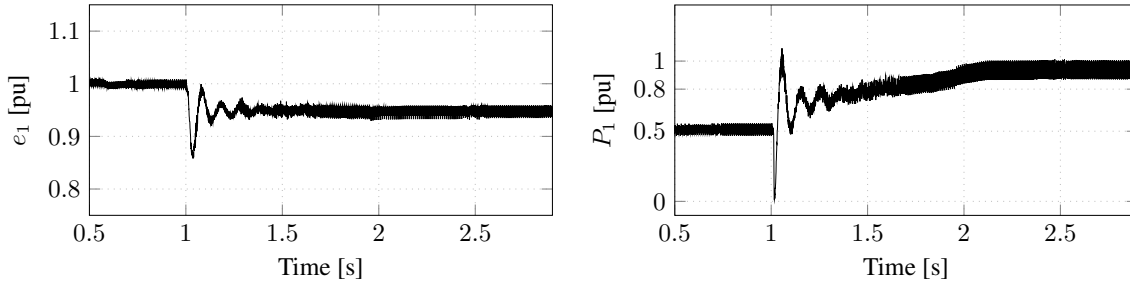


Figure 6.10: Simulated sequence of events. Voltage-margin control. DVC with $\omega_n = 0.8$ and $\xi = 1$. i_{f2}^{qref} . VSC₄ power consumption is ramped up until 0.4 pu. Left: VSC₁ voltage, e_1 . Right: VSC₁ power, P_1 .

also that the magnitude of the VSC₂ admittance is related to the bandwidth of the DVC. Therefore, the magnitude of the VSC₂ admittance can be decreased by reducing the speed of the DVC. The controller parameters of VSC₂, corresponding to a DVC bandwidth of 0.4 pu, are set according to Table 6.2. The same sequence of events defined in Section 6.2 is run (without reactive power injection) and the results are plotted in Figure 6.11. It can be seen that the instability shown in Figure 6.4 does not appear in this case, even with an active power transfer of 1 pu.

Table 6.2: Controller parameters of VSC₂

| | α | ω_n | ξ | k_p | k_i | k_{pe} | k_{ie} |
|--------|----------|------------|-------|-------|-------|----------|----------|
| Values | 4.0 | 0.4 | 1.0 | 1.0 | 0.01 | 1.54 | 0.31 |

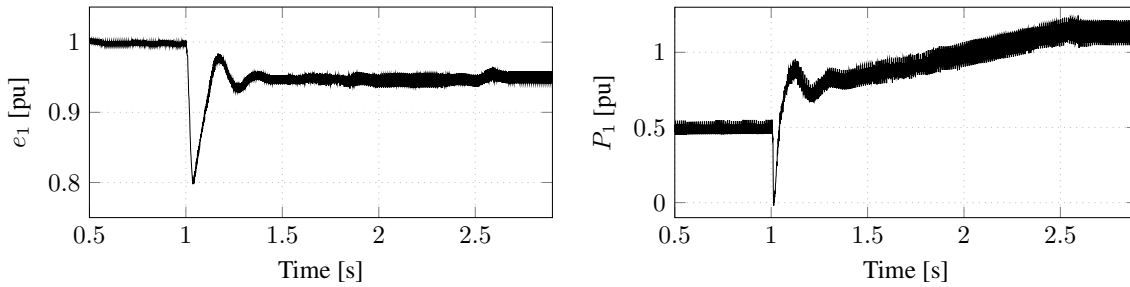


Figure 6.11: Simulated sequence of events. Voltage-margin control. DVC with $\omega_n = 0.4$ and $\xi = 1$. Left: VSC₁ voltage, e_1 . Right: VSC₁ power, P_1 .

6.4 Voltage-droop control strategy

For this set of simulations, VSC₁ and VSC₂ are set according to the voltage-droop control strategy discussed in Section 2.5. The droop setting for the i -th VSC is implemented as indicated in Figure 6.12, where k_{dri} is the slope of the droop setting and e_i^{nl} is the no-load voltage reference. The values of $k_{dr1,2}$ are selected as 0.1 pu for both VSCs, meaning

that the converter will increase its power output by 1 pu, if a voltage droop of 10 % the rated voltage occurs. The no-load voltages, e_1^{nl} and e_2^{nl} , are selected as 1.0 pu and 1.05 pu, respectively. For the sake of simplicity, the reference current i_{fi}^{dref} is used instead of the power, since it is proportional to active power of the VSC. With the parameters and the configuration selected, initially, VSC₁ will be supplying 300 MW, VSC₂ and VSC₄ will be operating with zero power, and VSC₃ will be consuming 300 MW.

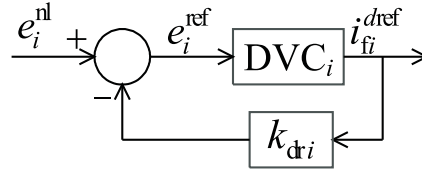


Figure 6.12: Direct-voltage droop control block diagram implemented in this section.

The parameters of the DVC and VCC of VSC₁ and VSC₂ are set as indicated in Table 6.1. The sequence of events stated in Section 6.2 is also run in this case, and the results are shown in Figure 6.13. The first difference that can be observed is that the sudden disconnection of VSC₁ does not produce the high fluctuation in the voltage, as in the voltage margin control. Another difference is that the instability occurs at a higher power compared to the case shown in Figure 6.4, where, almost immediately after VSC₂ is disconnected, the instability related to the dc-side resonance occurs. In this case, the instability occurs when the power at VSC₁ is around 0.9 pu. The increase of the stability limit can be explained

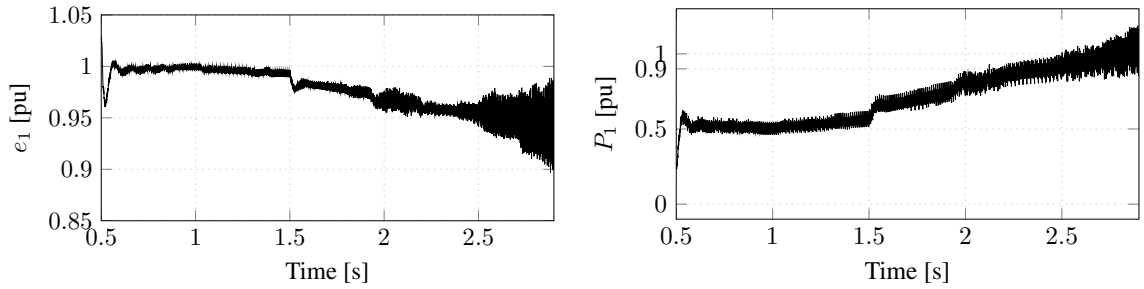


Figure 6.13: Simulated sequence of events. Voltage-droop control. DVC with $\omega_n = 0.8$ and $\xi = 1$. Left: VSC₁ voltage, e_1 . Right: VSC₁ power, P_1 .

by deriving the transfer function of the DVC including the voltage droop characteristic. In terms of small signals, the voltage droop characteristic can be expressed as

$$\Delta e_2^{ref} = \Delta e_2^{nl} - k_{dr2} \Delta i_{f2}^{dref} \quad (6.1)$$

which, combined with the DVC described by (4.15), gives

$$\frac{d\Delta n_2}{dt} = -\frac{k_{ie2}k_{dr2}}{k_{pe2}k_{dr2} + 1} \Delta n_2 + \frac{k_{ie2}}{k_{pe2}k_{dr2} + 1} (\Delta e_2^{nl} - \Delta e_2) \quad (6.2)$$

$$\Delta i_{f2}^{dref} = \frac{1}{k_{pe2}k_{dr2} + 1} \Delta n_2 + \frac{k_{pe2}}{k_{pe2}k_{dr2} + 1} (\Delta e_2^{nl} - \Delta e_2) \quad (6.3)$$

which subsequently gives the transfer function

$$\Delta i_{f2}^{dref} = \beta k_{pe2} \left(\frac{s + (k_{ie2} k_{dr2} \beta + \frac{1}{k_{pe2}})}{s + k_{ie2} k_{dr2} \beta} \right) (\Delta e_2^{nl} - \Delta e_2) \quad (6.4)$$

with $\beta = \frac{1}{k_{pe2} k_{dr2} + 1}$. Equation (6.4) shows that the DVC acts as a phase-lag compensator (since $\frac{1}{k_{pe2}} > 0$). Using the numerical values from Table 6.1, the zero and the pole of (6.4) are

$$z_1 = -0.42 \text{ pu}, \quad \lambda_1 = -0.094 \text{ pu} \quad (6.5)$$

which means that (6.4) adds a negative phase to the VSC admittance at low frequencies. At frequencies higher than 0.42 pu, the gain of the DVC transfer function is approximately βk_{pe} , which explicitly is

$$\beta k_{pe2} = \frac{k_{pe} \frac{1}{k_{dr2}}}{k_{pe2} + \frac{1}{k_{dr2}}} \quad (6.6)$$

which is less than k_{pe2} since k_{dr2} is usually less than 1. From (6.6), it can be interpreted that the effect of the droop characteristic on the VSC admittance is actually to decrease the magnitude of the VSC admittance. In this way, at the dc side resonance frequencies, the VSC conductance is smaller when the droop characteristic is introduced compared to the case without it. That explains why the stability limit has increased when using the voltage-droop control.

6.5 Impact of other control loops

In this section, the impact of other control loops on the dynamic performance of the system is investigated through simulations. One of the first assumptions made on the modelling of VSC is that the active power has been controlled directly by the current reference i_{fi}^{dref} instead of an outer loop power controller. The power controllers for VSC₃ and VSC₄ are implemented as suggested in Section 2.4.4 with $k_{pP} = 0$ and $k_{iP} = 31.42 \text{ pu}$, which gives a rise time of 220 ms. The parameters of the VCC and the DVC of all VSCs are set as indicated in Table 6.1 and the sequence of events stated in Section 6.2 is simulated. Figure 6.14 shows the voltage and the power of VSC₂ and it can be seen that the instability related to the dc-side resonance still occurs in a similar way as shown in Figure 6.4, where no outer loop power controller had been implemented. However, the low frequency oscillations which appear in Figure 6.4 from $t = 2.5\text{s}$, are not present when the power controller is implemented as can be seen in Figure 6.14. The comparison indicates that the power controller does not have a major impact on the dynamics related to the dc-side resonance, so the current reference i_{f2}^{dref} can be used directly to control the active power supply/consumption of the converter. Observe that the difference between Figures 6.4 and 6.14 are mainly dictated by the slight different in transmitted power when the power controllers are activated.

The alternating-voltage controller can be implemented at VSC₁ and VSC₂ in order to improve the voltage profile, since the voltage at the PCC decreases as the power supply increases. Since, in the studied sequence of events VSC₂ ends up to be the only converter that controls the direct-voltage of the system, the alternating-voltage controller described

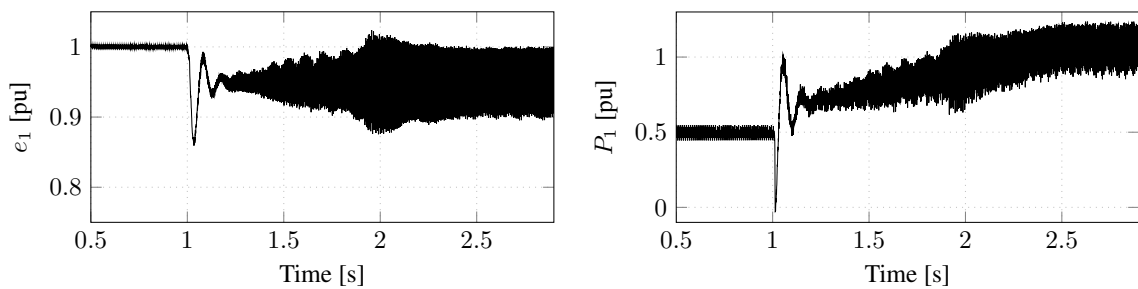


Figure 6.14: Simulated sequence of events. Voltage-margin control with act. power controller. DVC with $\omega_n = 0.8$ and $\xi = 1$. Left: VSC₁ voltage, e_1 . Right: VSC₁ power, P_1 .

in Section 2.4.5 is implemented in this converter with $k_{pU} = 1$ pu and $k_{iU} = 0.32$ pu. The results of the simulation are shown in Figure 6.15; it can be seen that the instability takes place at a higher power transfer, compared to Figure 6.4. The results presented in Figure 6.15 are very similar to ones shown in Figures 6.7 and 6.8 where reactive power is injected to the ac side of VSC₂. This indicates that a small variation in the VSC₂ admittance (due to the reactive power injection) together with a better voltage profile at the PCC leads to an increase of the amount of active power that the VSC₂ can inject into the dc grid without losing stability.

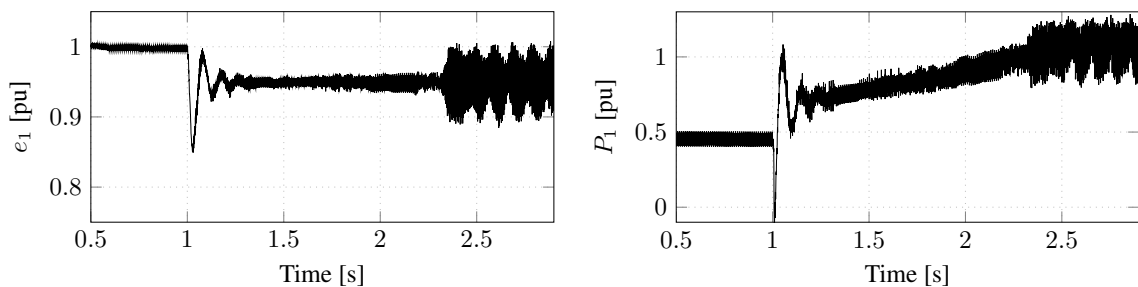


Figure 6.15: Simulated sequence of events. Voltage-margin control with alternating-voltage controller. DVC with $\omega_n = 0.8$ and $\xi = 1$. Left: VSC₁ voltage, e_1 . Right: VSC₁ power, P_1 .

6.6 Conclusions

In this chapter, simulations have been performed in order to extend the analysis developed in the previous chapters. A four-terminal VSC-HVDC system has been modelled in PSCAD, and its dynamic performance has been tested for different parameters, control strategies, and operating points. Simulation results confirm the results obtained through the analysis carried out in the previous chapters. It has been shown that the dc-side resonance are not amplified when decreasing the bandwidth of the DVC. Through simulations, it has been shown that the voltage-droop control strategy has a better dynamic performance, since it has the effect of decreasing the magnitude of the VSC admittance. Additional tests

were carried out, in which the impact of other loops on dc-side resonance related stability is studied. The tests have shown that the injection of reactive power, or the control of the alternating-voltage at the PCC, increase the stability limit since it improves the voltage profile at the PCC and changes the VSC admittance. The active power controller does not seem to have any significant effect on the dc side dynamics. This is due to the fact that the active power controller will only respond to disturbances in the ac side. It is of importance to stress that the analysis carried out in Chapters 4 and 5 considers that the VSCs are linear amplifiers that are capable of delivering any kind of power level. However, in the implemented PSCAD model, actual switching converters have been considered. This leads to small mismatches between the theoretical and the simulated models.

Chapter 7

Conclusions and future work

7.1 Conclusions

In this thesis, the dc network dynamics of VSC-HVDC systems has been thoroughly investigated. Small signal analysis has been used, initially, to determine the main factor that impact the stability of the VSC-HVDC system. A modelling procedure to obtain the state space model of the system has been developed in such a way that individual subsystems are modelled, and, after that, they are merged into the system of interest.

From eigenvalue analysis in a two-terminal HVDC system, it has been found that the main factors that impact the dc-side stability of the system are the following:

1. The dc-side resonance phenomenon, which takes place due to the RLC characteristics of the cables which conform the dc network.
2. The direction of the power transfer, since it has been shown that the more power the VSC which controls the direct voltage injects to the dc side, the more the poles related to resonance phenomenon moves to the left side of the s-plane. On the other hand, the more power the VSC which controls the direct voltage absorbs from the dc side, the more the poles move to the right side of the s plane.
3. The size of the gains of the direct-voltage controller. It has been shown that high gains turns the system more prone to instability than low gains.
4. The strength of the ac system to which the VSC which controls the direct voltage is connected. The weaker the system, the more the poles related to the dc side resonance move to the left side of the s-plane.
5. The ac side grid configuration. The case when a capacitor is connected at the PCC has been studied and it was found that ac side resonances can also turn the system unstable.

Although eigenvalue analysis is a powerful tool to study the stability of the system, it does not give a clear insight on the source of the instability found in the analysis. A frequency

domain approach is proposed in this thesis to explain the conditions in which the system turns unstable. A two-terminal VSC-HVDC system is modelled as a SISO feedback system, where the VSC-system transfer function and the dc grid transfer function are defined. The VSC-system transfer function can be interpreted as an admittance, called the VSC admittance in this thesis, and the dc grid transfer function as an impedance. The dc grid impedance has its real part positive for all frequencies since its electrical circuit is composed by passive elements. The main characteristic of the dc grid impedance are the resonance peaks that appear as a result of the RLC resonances. On the other hand, the real part of the VSC admittance is negative or positive depending on the direction of the active power and the frequency. In the unstable cases, the dc grid resonance peak coincides with a negative VSC conductance, meaning that, instead of being damped, the resonance is amplified, if the conductance is sufficiently high. The impact of different factors on the VSC admittance is studied as well. The frequency domain approach proposed in this thesis can provide design criteria for the VSC control system. For example, in order to avoid instability related to dc-side resonances, the control system can be designed such that the magnitude of the VSC admittance is below a certain value at frequencies around the dc-side resonance frequency.

Finally, a four-terminal HVDC system has been modelled and some events has been tested for two control strategies, the voltage-margin control, and the voltage-droop control. The results confirms the findings from previous chapters, and the knowledge acquired from the analysis performed in the previous chapters is utilized to explain the instability which occurred in the simulated cases. Particularly, it has been shown that the voltage-droop control strategy has a better performance than the voltage-margin control strategy, from the dynamic point of view. It has been found that the application of the voltage-droop controller decreases the magnitude of the VSC admittance, reducing then the risk of dc side instabilities. Other control loops has been studied, and it has been shown that the injection of reactive power, or the voltage control at the PCC increases the power limit from the stability point of view. Moreover, the impact of the active power controller has been studied and it has been found that it does not have a significant impact on the system dynamics.

7.2 Future work

The main philosophy adopted in this thesis has been the simplification of the studied model as much as possible. This facilitates the analysis since, obviously, the study of simple systems are easier than the study of complex systems that accounts for all the possible control loops into the model. Simplifications adopted in this thesis are, for example, waiving the active and reactive power control loops, the alternating-voltage control loop, assuming the measurement devices ideal, etc. A next step on this work is then to study the stability of an increasingly complex HVDC system, not only considering the complexity of the VSC control structure, but also the complexity of the dc network (composed by different types of cables and overhead transmission lines).

Moreover, this works has been devoted to the explanation of the instability found in the dc

network. However, the design of the control system such that the instability is avoided has not been investigated in this thesis. The approach proposed in this thesis can be used to provide criteria for the design of the control system.

Experimental verification of the theoretical derivations and the simulation results is needed in order to give strength to the findings pointed out in this thesis.

In addition, in this thesis, small signal analysis is performed, meaning that the results are only valid for very slow changes of the operating conditions. Large disturbance phenomena such as the low frequency oscillations identified in Section 6.5 and Section 6.3 can also occur and their investigation are of interest, especially in complex infrastructures such as MTDC systems. For these investigations, the ideal converter models used for the theoretical analysis in this thesis, can be further improved by implementing average converter models.

Further analysis can be carried with the aim of providing design and operation practices. For example, the VSC capacitor can be designed considering the benefits that the selected capacitor can bring to the HVDC system dynamic performance. Requirements on maximum power ramp up/down time or rise times considering a given controller speed can also be determined.

The performance of the HVDC control system during and after a fault, either in the ac side or dc side, is also an important topic to investigate, especially in meshed HVDC grids. Issues such as fault detection methods, protection schemes, calculation of electrical quantities in fault conditions, etc, are some of the topics to investigate in the future.

Chapter 7. Conclusions and future work

References

- [1] 50 HERTZ, Energinet.dk, Svenska Kraftnät, “Kriegers Flak Combined Grid Solution Feasibility Study,” Joint Report, 24, February, 2010. Available from http://www.50hertz.com/en/file/2010-02-24_Final_Feasibility_Study_Public.pdf
- [2] E. Koldby, M. Hyttinen, “Challenges on the Road to an Offshore HVDC Grid,” *5th Nordic Wind Power Conference*, 10-11, September 2009
- [3] G. Asplund, B. Jacobson, B. Berggren, K. Lindén, “Continental Overlay HVDC-Grid,” *Cigré Session*, Paris, France, 22-27, August, 2010.
- [4] A. L’Abbate, G. Migliavacca, U. Häger, C. Rehtanz, S. Rüberg, H. Ferreira, G. Fulli, A. Purvins, “The role of facts and HVDC in the future paneuropean transmission system development,” *9th IET International Conference on AC and DC Power Transmission*, London, UK, 19-21 Oct. 2010
- [5] U. Axelsson, A. Holm, C. Liljegren, K. Eriksson, L. Weimers, “Gotland HVDC Light Transmission - World’s First Commercial Small Scale dc Transmission,” *CIREN, 15th International Conference and Exhibition on Electricity Distribution*, Nice, France, 1-4, June, 1999.
- [6] D. Van Hertem, M. Ghandhari, M. Delimar, “Technical Limitations towards a Super-Grid - A European Prospective,” *IEEE International Energy Conference and Exhibition (EnergyCon)*, Manama, Baharain, 18-22, December, 2010.
- [7] N. Ahmed, A. Haider, D. Van Hertem, L. Zhang, HP. Nee, “Prospects and Challenges of Future HVDC SuperGrids with Modular Multilevel Converters,” *14th European Conference on Power Electronics and Applications*, Birmingham, UK, 30 August - 1 September, 2011.
- [8] J. Arrillaga, Y.H. Liu, N.R. Watson, *Flexible Power Transmission: the HVDC Options*, pp. 98, John Wiley and Sons Ltd, 2007.
- [9] N. Mohan, T.M. Undeland, *Power Electronics: Converter, Applications, and Design*, pp. 220, John Wiley and Sons Inc., 2007.
- [10] B. Jacobson, P. Karlsson, G. Asplund, L. Harnefors, T. Jonsson, “VSC-HVDC Transmission with Cascaded Two-Level Converters,” *Cigré Session*, Paris, France, 22-27 August 2010.

References

- [11] B. Gemmell, J. Dorn, D. Retzmann, D. Soerangr, "Prospects of Multilevel VSC Technologies for Power Transmission," *Transmission and Distribution Conference and Exposition*, Milpitas, CA, 21-24 April, 2008.
- [12] Alstom, "Think Grid-Sharing Alstom Grid Innovation and Practices," Technical Magazine, no. 8, Spring/Summer 2011.
- [13] J. Glasdam, J. Hjerrild, L.H. Kocewiak, C.L. Bak, "Review on Multi-Level Voltage Source Converter Based HVDC Technologies for Grid Connection of Large Offshore Wind Farms," *International Conference on Power System Technology POWERCON*, Auckland, New Zealand, October 30-November 2, 2012.
- [14] S. P. Teeuwesen, "Modeling the Trans-Bay Cable Project as Voltage-Sourced Converter with Modular Multilevel Converter Design," *IEEE PES General Meeting*, San Diego, CA, 24-29 July 2011.
- [15] ABB, "It is time to connect-Technical description of HVDC Light Technology," Technical Brochure, Issued in March 2008.
- [16] ABB, "It is time to connect-Technical description of HVDC Light Technology," Technical Brochure, Issued in December 2012.
- [17] F. Wang, L. Bertling, T. Ahn Le, A. Mannikoff, A. Bergman, "An Overview Introduction of VSC-HVDC: State-of-the-art and Potential Applications in Electric Power System," *Cigré International Symposium: The Electric Power System of the Future, Integrating supergrids and microgrids*, Bologna, Italy, 13-15, September, 2011.
- [18] L. Harnefors, H-P. Nee, "Model-Based Current Control of AC Machines Using the Internal Model Control Method," *IEEE Trans. on Industry Applications*, vol. 34, no. 1, pp. 133-141, January/February, 1998.
- [19] M. Bongiorno, "On Control of Grid Connected Voltage Source Converters - Mitigation of Voltage Dips and Subsynchronous Resonances," PhD Dissertation, Chalmers University of Technology, Gothenburg, Sweden, August 2007.
- [20] M. Bongiorno, "An Advanced Cascade Controller for Series-Connected VSC for Voltage Dip Mitigation," *IEEE Trans. on Industry Applications*, vol.33, no. 1, pp.187-195, January-February, 2008.
- [21] C. Du, "VSC-HVDC for Industrial Power Systems," PhD Dissertation, Chalmers University of Technology, Gothenburg, April 2007.
- [22] L. Harnefors, H-P. Nee, "A General Algorithm for Speed and Position Estimation of AC Motors," *IEEE Trans. on Industrial Electronics*, vol. 47, no. 1, pp. 77-83, February, 2000.
- [23] L. Ängquist, M. Bongiorno, "Auto-normalizing Phase-Locked Loop for Grid-connected Converters," *Energy Conversion Congress and Exposition*, San Jose, CA, 20-24 September 2009.
- [24] M. Beza, "Control of Energy Storage Equipped Shunt-Connected Converter for Elec-

- tric Power System Stability Enhancement,” Licentiate Thesis, Chalmers University of Technology, Gothenburg, Sweden, May, 2012.
- [25] M. Bongiorno, J. Svensson, A. Sannino, “Effect of Sampling Frequency and Harmonics on Delay-Based Phase-Sequence Estimation Method,” *IEEE Trans. on Power Delivery*, vol. 23, no. 3, pp. 1664-1671, July, 2008.
- [26] S. Cole, “Steady-State and Dynamic Modelling of VSC-HVDC Systems for Power System Simulation,” PhD Dissertation, University of Leuven, Leuven, Belgium, September, 2010.
- [27] W.F. Long, J. Reeve, J.R. McNichol, M.S Holland, J.P. Taisne, J. LeMay, D.J. Lorden, “Application Aspects of Multiterminal DC Power Transmission,” *IEEE Trans. on Power Delivery*, vol. 5, no. 4, pp. 2084-2098, November, 1990.
- [28] ABB, “Québec - New England: The first large scale multiterminal HVDC transmission in the world.” available from <http://new.abb.com/systems/hvdc/references/quebec-new-england>.
- [29] J. Reeve, “Multiterminal HVDC Power Systems,” *IEEE Trans. On Power Apparatus and Systems*, vol. PAS-99, no. 2, pp 729-737, March/April, 1980.
- [30] G. Pinares, M. Bollen, “Understanding the Operation of HVDC Grids,” *Cigré International Symposium: The Electric Power System of the Future, Integrating supergrids and microgrids*, Bologna, Italy, 13-15, September, 2011.
- [31] T.M. Hailesalassie, M. Molinas, T. Undeland, “Multi-terminal VSC-HVDC System for Integration of Offshore Wind Farms and Green Electrification of Platforms in the North Sea,” *NORPIE*, Espoo, Finland, 9 - 11, June, 2008.
- [32] T. Nakajima, S. Irokawa, “A control System for HVDC Transmission by Voltage Sourced Converters,” *IEEE Power Engineering Society Summer Meeting*, Edmonton, Alta, 18-22, July, 1999.
- [33] T.M. Hailesalassie, K. Uhlen, T. Undeland, “Control of Multiterminal HVDC Transmission for Offshore Wind Energy,” *Nordic Wind Power Conference*, Bornholm, Denmark, 10-11, September, 2009.
- [34] J. Liang, O. Gomis-Bellmunt, J. Ekanayake, N. Jenkins, “Control of multi-terminal VSC-HVDC transmission for offshore wind power,” *13th European Conference on Power Electronics and Applications*, 8-10, September, 2009.
- [35] A. Emadi, M. Ehsani, and J. M. Miller, *Vehicular electric power systems: land, sea, air, and space vehicles*, New York: Marcel Dekker, December 2003.
- [36] A. Emadi, M. Ehsani, “Multi-Converter Power Electronic Systems: Definition and Applications,” *Power Electronic Specialist Conference*, Vancouver, BC, 17-21 June 2001.
- [37] A. Emadi, M. Ehsani, “Dynamics and Control of Multi-Converter DC Power Electronic Systems,” *Power Electronic Specialist Conference*, Vancouver, BC, 17-21 June

References

2001.

- [38] A. Emadi, A. Khaligh C.H. Rivettam, G. A. Williamson, "Constant Power Loads and Negative Impedance Instability in Automotive Systems: Definition, Modelling, Stability, and Control of Power Electronic Converters and Motor Drives," *IEEE Trans. On Vehicular Technology*, vol. 55, no. 4, pp. 1112-1125, July 2006.
- [39] A. Kwasinski, C. N. Onwuchekwa, "Dynamic Behavior and Stabilization of DC Microgrids With Instantaneous Constant-Power Loads," *IEEE Trans. On Power Electronics*, vol. 26, no. 3, pp. 822-834, March 2011.
- [40] S.D. Sudhoff, S.F. Glover, P.T. Lamm, D.H. Schmucker, D.E. Delisle, "Admittance Space Stability Analysis of Power Electronic Systems," *IEEE Trans. on Aerospace and Electronic System*, vol. 36, no. 3, part 1, pp.965-973, July 2000.
- [41] S.D. Sudhoff, S.F. Glover. "Stability Analysis Methodologies for DC Power Distribution Systems," in *Proceedings of the 13th international Ship Control System Symposium*, April 2003.
- [42] J. R. LeSage, R. G. Longoria, W. Shutt, "Power System Stability Analysis of Synthesized Complex Impedance Loads on an Electric Ship," *IEEE Electric Ship Symposium*, Alexandria, VA, 10-13 April 2011.
- [43] H. Latorre, "Modeling and Control of VSC-HVDC Transmissions," PhD Dissertation, Royal Institute of Technology, Stockholm, Sweden, April 2011.
- [44] L. Harnefors, M. Bongiorno, S. Lundberg, "Input Admittance Calculation and Shaping for Controlled Voltage-Source Converters," *IEEE Trans. on Industrial Electronics*, vol. 54, no. 6, December 2007.
- [45] L. Harnefors, M. Bongiorno, S. Lundberg, "Stability Analysis of Converter-Grid Interaction using the Converter Input Admittance," *European Conference on Power Electronics and Applications*, Aalborg, Denmark, 2-5 September 2007.
- [46] L. Zhang, "Modeling and Control of VSC-HVDC Links Connected to Weak AC Systems," PhD Dissertation, Royal Institute of Technology, Stockholm, Sweden, April 2010.
- [47] F. Mura, C. Meyer, R. W. De Doncker, "Stability Analysis of High-Power DC Grids," *IEEE Trans. On Industry Applications*, vol. 46, no. 2, March 2010.
- [48] B. Yin, R. Oruganti, S. K. Panda, A. K. S. Bhat, "A Single-Input-Single-Output (SISO) Model for a Three-Phase PWM Rectifier," *IEEE Trans. on Power Electronics*, vol. 24, no. 3, March 2009.
- [49] L. Tang, "Control and Protection of Multi-terminal DC Transmission Systems Based on Voltage-Source Converters", PhD Dissertation, McGill University, Montreal, Québec, Canada, January 2003.
- [50] P. Rault, F. Colas, X. Guillaud, S. Nguéfeu, "Method for Small Signal Stability Analysis of VSC-MTDC grids," *IEEE PES General Meeting*, San Diego, CA, 22-26 July

- 2012.
- [51] G.O. Kalcon, G. P. Adam, O. Anaya-Lara, S. Lo, K. Uhlen, "Small-Signal Stability Analysis of Multi-terminal VSC-Based DC Transmission Systems," *IEEE Trans. On Power Systems*, vol. 27, no. 4, pp. 1818-1830, November 2012.
 - [52] A. M. Alsseid, D. Jovcic, A. Starkey, "Small Signal Modelling and Stability Analysis of Multiterminal VSC-HVDC," *European Conference on Power Electronics and Applications*, Birmingham, UK, 30 August - 1 September, 2011.
 - [53] S. Rodrigues, "Dynamic Modelling and Control of VSC-based Multi-terminal DC Networks," MSc Thesis, Universidade Técnica de Lisboa, Lisboa, Portugal, December, 2011.
 - [54] G. Pinares, "Operation of HVDC grids in parallel with AC grids," Master of Science Thesis, Chalmers University of Technology, Gothenburg, Sweden, June, 2010.
 - [55] P. Kundur, *Power System Stability and Control*, Tata McGraw-Hill Education, 1994.
 - [56] J.J.E. Slotine, W. Li, *Applied Nonlinear Control*, Vol. 199, No. 1, New Jersey: Prentice Hall, 1991.
 - [57] C.D. Barker, R. Whitehouse, "Autonomous Converter Control in a Multi-terminal HVDC System," *9th IET International Conference on AC and DC Power Transmission*, London, UK, 19-21, October, 2010.
 - [58] S. Skogestad and I. Postlethwaite, *Multivariable Feedback Control: Analysis and Design*, 2nd Edition. West Sussex, England: John Wiley and Sons Ltd., 2005.

References

Appendix A

Three-phase transformations

In this appendix, the necessary transformations from three-phase quantities to vectors in stationary $\alpha\beta$ and rotating dq frames, and vice versa, are described.

A.1 Transformation of three phase quantities to vectors

A three-phase system composed by three quantities $u_a(t)$, $u_b(t)$ and $u_c(t)$ can be transformed into a two-component vector, $\underline{u}^{\alpha\beta}(t)$, in a stationary complex reference frame, usually called $\alpha\beta$ -frame, by applying the transformation defined by

$$\underline{u}^{\alpha\beta}(t) = u^\alpha(t) + ju^\beta(t) = K_{\text{tr}}(u_a(t) + u_b(t)e^{j\frac{2}{3}\pi} + u_c(t)e^{j\frac{4}{3}\pi}). \quad (\text{A.1})$$

The transformation constant K_{tr} can be chosen between $\sqrt{2/3}$ or $2/3$ to ensure power invariant or amplitude invariant transformation, respectively. It should be highlighted that amplitude invariant transformation is used in this thesis. Equation (A.1) can be expressed in matrix form as

$$\begin{bmatrix} u^\alpha(t) \\ u^\beta(t) \end{bmatrix} = \mathbf{T}_{32} \begin{bmatrix} u_a(t) \\ u_b(t) \\ u_c(t) \end{bmatrix} \quad (\text{A.2})$$

where the matrix \mathbf{T}_{32} is given by

$$\mathbf{T}_{32} = K_{\text{tr}} \begin{bmatrix} 1 & -\frac{1}{2} & -\frac{1}{2} \\ 0 & \frac{\sqrt{3}}{2} & -\frac{\sqrt{3}}{2} \end{bmatrix}.$$

The inverse transformation, assuming no zero-sequence, i.e. $u_a + u_b + u_c = 0$, is given by

$$\begin{bmatrix} u_a(t) \\ u_b(t) \\ u_c(t) \end{bmatrix} = \mathbf{T}_{23} \begin{bmatrix} u^\alpha(t) \\ u^\beta(t) \end{bmatrix} \quad (\text{A.3})$$

with the matrix \mathbf{T}_{23} given by

$$\mathbf{T}_{23} = \frac{1}{K_{\text{tr}}} \begin{bmatrix} \frac{2}{3} & 0 \\ -\frac{1}{3} & \frac{1}{\sqrt{3}} \\ \frac{1}{3} & -\frac{1}{\sqrt{3}} \end{bmatrix}.$$

A.2 Transformation between stationary and rotating coordinate systems

For the vector $\underline{u}^{\alpha\beta}(t)$ rotating in the $\alpha\beta$ -frame with the angular frequency $\omega(t)$ in the positive (counter-clockwise) direction, a dq -frame that rotates in the same direction with the same angular frequency $\omega(t)$ can be defined. In this reference frame, the vector $\underline{u}^{\alpha\beta}(t)$ appears as a stationary vector. A projection of the vector in the d -axis and q -axis of the dq -frame gives the components of the vector in the dq -frame as illustrated in Figure A.1.

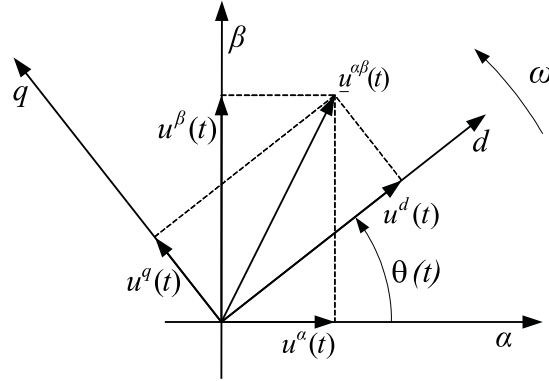


Figure A.1: Relation between $\alpha\beta$ -frame and dq -frame.

The transformation can be written in vector form as

$$\underline{u}^{dq}(t) = u^d(t) + ju^q(t) = \underline{u}^{\alpha\beta}(t)e^{-j\theta(t)} \quad (\text{A.4})$$

with the angle $\theta(t)$ in Fig.A.1 given by

$$\theta(t) = \theta_0 + \int_0^t \omega(\tau)d\tau.$$

The inverse transformation, from the rotating dq -frame to the fixed $\alpha\beta$ -frame is defined by

$$\underline{u}^{\alpha\beta}(t) = \underline{u}^{dq}(t)e^{j\theta(t)}. \quad (\text{A.5})$$

In matrix form, the transformation between the fixed $\alpha\beta$ -frame and rotating dq -frame can be written as

$$\begin{bmatrix} u^d(t) \\ u^q(t) \end{bmatrix} = \mathbf{R}(-\theta(t)) \begin{bmatrix} u^\alpha(t) \\ u^\beta(t) \end{bmatrix} \quad (\text{A.6})$$

A.2. Transformation between stationary and rotating coordinate systems

$$\begin{bmatrix} u^\alpha(t) \\ u^\beta(t) \end{bmatrix} = \mathbf{R}(\theta(t)) \begin{bmatrix} u^d(t) \\ u^q(t) \end{bmatrix} \quad (\text{A.7})$$

where the projection matrix $\mathbf{R}(\theta(t))$ is

$$\mathbf{R}(\theta(t)) = \begin{bmatrix} \cos(\theta(t)) & -\sin(\theta(t)) \\ \sin(\theta(t)) & \cos(\theta(t)) \end{bmatrix}.$$

Appendix A. Three-phase transformations

Appendix B

Symbols and Per-unit Convention

The adopted symbolic representation of the variables in different coordinate systems are explained in this appendix. In addition, since per-unit values are used extensively in this thesis, their definition are also presented.

B.1 Coordinate systems

From the ac side perspective, three types of electrical variables are used throughout this thesis. The three-phase ac voltages and currents, the $\alpha\beta$ quantities, and the dq quantities (where the transformation methods are presented in Appendix A). Three-phase variables are represented as non-underlined variables with a subscript which highlights certain characteristics of the variable. The subscripts a , b and c are added when the individual phase of the variable is handled. For example, from Figure 2.9:

- i_f : is the three-phase current that flows through the filter.
- i_{fa} : is the current that flows through the phase a of the filter.
- i_{fb} : is the current that flows through the phase b of the filter.
- i_{fc} : is the current that flows through the phase c of the filter.

In the $\alpha\beta$ -frame (or coordinate system), the three-phase quantities are transformed into two-component rotating vectors. Vectors in this thesis are represented as underlined variables and the complex number notation is often used to represent the vector. For example, the three-phase current i_f in the $\alpha\beta$ -frame is represented as

$$\underline{i}_f^{\alpha\beta} = i_f^\alpha + j i_f^\beta.$$

where $\underline{i}_f^{\alpha\beta}$ is a current vector in the stationary $\alpha\beta$ -frame, and i_f^α and i_f^β are the current components in the α and β axis, respectively. In the same fashion, the current i_f can be expressed in the dq -frame as

$$\underline{i}_f^{dq} = i_f^d + j i_f^q$$

where \underline{i}_f^{dq} is the current vector in the rotating dq -frame, and i_f^d and i_f^q are the current components in the d and q axes, respectively. In addition, other rotating reference frames, such as

Appendix B. Symbols and Per-unit Convention

the *ideally aligned dq*-frame, are referred to in the thesis. In that case, a superscript is added to denote that rotating frame corresponds a particular coordinate system. For example, in the ideally aligned *dq*-frame, the the current i_f is expressed as

$$\underline{i}_f^{idq} = i_f^{id} + j i_f^{iq}$$

where \underline{i}_f^{idq} is the current vector in the rotating ideal *dq* frame, and i_f^{id} and i_f^{iq} are the current components in the ideal *d* and *q* axes, respectively. The filter reactor current in the grid *dq* frame, defined in Section 4.4.1, is represented as \underline{i}_f^{sdq} . However, variables in the converter *dq* frame, defined in Section 4.4.1, are represented without any special superscript, e.g. i_f^{dq} . In some cases, the matrix notation is used instead of the complex number notation, especially in the Laplace domain. For instance, the current \underline{i}_f^{dq} in matrix notation is

$$\mathbf{i}_f^{dq} = \begin{bmatrix} i_f^d \\ i_f^q \end{bmatrix}.$$

Matrices, in general, are represented as bold symbols and do not represent necessarily electrical variables. Thus, their elements are always specified in order to avoid confusion.

Variables in the dc side are represented similar to three-phase variables, i.e. not underlined and with a subscript which describes a characteristic of the variable. Whether the variable represents an ac or dc quantity is stated in the thesis.

B.2 Per unit values

In this thesis, the electrical variables (currents and voltages), as well as variables which denote electrical properties (impedances, inductances, capacitances, frequencies) are treated in per unit. The bases are defined as defined in Table B.1.

It should be highlighted that the base voltage and current in the ac side are the peak of the line-to-neutral voltage and the peak of the line current, respectively. Moreover, in the dc side, only one of the poles are studied since only symmetrical cases are assumed. Thus, the dc-side base power is half of the ac-side base power. As an example, Table B.2 shows numerically the base values selected for the system shown in Figure 3.12 and whose ratings are as indicated in Table 3.1.

Table B.1: Base values

| Base value | Definition |
|---|---|
| Base time (t_{base}) | $(2\pi f_{\text{nominal}})^{-1}$ |
| Base frequency (ω_{base}) | $2\pi f_{\text{nominal}}$ |
| Base Power (S_{acbase}) | $S_{\text{VSC-rated}}$ |
| ac side - Base voltage (U_{acbase}) | $\sqrt{2/3}U_{\text{LL-rated}}$ |
| ac side - Base current (I_{acbase}) | $\frac{2}{3} \frac{S_{\text{base}}}{U_{\text{acbase}}}$ |
| ac side - Base impedance (Z_{acbase}) | $\frac{U_{\text{acbase}}}{I_{\text{acbase}}}$ |
| ac side - Base inductance (L_{acbase}) | $\frac{Z_{\text{acbase}}}{\omega_{\text{base}}}$ |
| ac side - Base capacitor (C_{acbase}) | $(Z_{\text{acbase}}\omega_{\text{base}})^{-1}$ |
| dc side - Base power (S_{dcbase}) | $\frac{S_{\text{VSC-rated}}}{2}$ |
| dc side - Base voltage (U_{dcbase}) | E_{rated} |
| dc side - Base current (I_{dcbase}) | $\frac{S_{\text{dcbase}}}{E_{\text{dcbase}}}$ |
| dc side - Base impedance (Z_{dcbase}) | $\frac{U_{\text{dcbase}}}{I_{\text{dcbase}}}$ |
| dc side - Base inductance (L_{dcbase}) | $\frac{Z_{\text{dcbase}}}{\omega_{\text{base}}}$ |
| dc side - Base capacitor (C_{dcbase}) | $(Z_{\text{dcbase}}\omega_{\text{base}})^{-1}$ |

Table B.2: Example of base values for the rated values from Table 3.1

| Base value | Numerical value |
|------------------------|---------------------|
| ω_{base} | 314.16 rad/s |
| S_{acbase} | 600 MVA |
| U_{acbase} | 244.95 kV |
| I_{acbase} | 1.63 kA |
| Z_{acbase} | 150 Ω |
| L_{acbase} | 477 mH |
| C_{acbase} | 21.22 μF |
| S_{dcbase} | 300 MW |
| U_{dcbase} | 300 kV |
| I_{dcbase} | 1 kA |
| Z_{dcbase} | 300 Ω |
| L_{dcbase} | 955 mH |
| C_{dcbase} | 10.6 μF |